U.PORTO
FEUP FACULDADE DE ENGENHARIA
UNIVERSIDADE DO PORTO

Development of a Patient-Specific device to guide and assist the knee arthroscopy

by
Nuno Filipe Vieira Gonçalves

Thesis submitted to
Faculdade de Engenharia da Universidade do Porto
as a requirement to obtain the MSc Degree in Mechanical Engineering

under the supervision of
Professor Jorge Américo Oliveira Pinto Belinha
and
Professor Renato Natal Jorge

Porto, July 2019

"Não há derrotas quando é firme o passo,
ninguém fala em perder, ninguém recua
e a mocidade invicta em cada abraço,
a si mais nos estreita: a pátria é sua!"

Pedro Homem de Melo,
Aleluia! Daqui houve nome Portugal

Acknowledgements / Agradecimentos

Em primeiro lugar e porque nada disto seria possível sem que tivesse acreditado em mim e neste projeto, agradecer ao Professor Jorge Belinha por toda a disponibilidade e tempo despendido ao longo do último semestre. Por, com toda a humildade, sempre me ter esclarecido todas as dúvidas que eventualmente surgiam.

À minha Mãe e ao meu Pai, Manuela e Fernando, por sempre terem estado a meu lado para me ajudar e levar pelo rumo certo, mostrando-me diariamente que nada se consegue sem esforço e superação, mantendo sempre ao meu redor um clima de amor e união, que foram essenciais para o meu desenvolvimento enquanto pessoa e engenheiro. É um grande orgulho ser vosso filho.

À minha avó Cândida e ao avô Miguel, por me terem aturado e formado ao longo da minha infância. Particularmente à D. Cândida, agradecer os almoços, lanches e jantares e os panados que me fazem recordar de onde vim.

Ao meu irmão Luís, por me mostrar que não há apenas uma forma de viver a vida e por, desde sempre, ser um exemplo para mim, quebrando sempre as barreiras que se vão pondo no caminho, mantendo-se sempre fiel a si próprio.

À Carolina, que desde muito cedo me tem acompanhado ao longo da caminhada com um sorriso nos lábios, sempre contagiante, mesmo em alturas de maior adversidade. Por ser a toda a hora um exemplo de superação para mim e por contribuir, todos os dias, para o meu sucesso académico e pessoal.

Aos meus parceiros da Faculdade, os que estiveram sempre em todas as aventuras e peripécias, alegrias e tristezas, na Biblioteca, no Departamento, ou onde for. Bolly; Paupério; Pena; Random; Reis; Ricky; Semeão; Sousa e Zé, sem vocês não seria possível... obrigado Clitos.

À restante família que não pude nomear: avós; tios; primos, por me fazerem sentir orgulhoso de partilhar com vocês a minha vida.

Aos amigos de sempre: Cuca; Joel; Leandro; Samuel e Roleta com quem vivi momentos únicos, de gargalhadas e parvoíces, que ajudaram à minha formação enquanto pessoa.

Sem todos os citados e, certamente, outros que não tive oportunidade de mencionar, nada disto seria possível. Não é só meu... também é muito vosso.

Por último, à FEUP... foi um orgulho imenso fazer parte desta casa e ter sido aluno de docentes de valor reconhecido internacionalmente. Foram certamente os melhores anos da minha vida e por isso vai deixar tantas saudades.

Institutional Acknowledgements

The author truly acknowledges the work conditions provided by the Applied Mechanics Division (SMAp) of the department of mechanical engineering (DEMec) of Faculty of Engineering of the University of Porto (FEUP), and by the MIT-Portugal project "MIT-EXPL/ISF/0084/2017", funded by Massachusetts Institute of Technology (USA) and "Ministério da Ciência, Tecnologia e Ensino Superior - Fundação para a Ciência e a Tecnologia" (Portugal).

Additionally, the authors gratefully acknowledge the funding of Project NORTE-01-0145-FEDER-000022 - SciTech - Science and Technology for Competitive and Sustainable Industries, cofinanced by Programa Operacional Regional do Norte (NORTE2020), through Fundo Europeu de Desenvolvimento Regional (FEDER).

Finally, the author acknowledges the synergetic collaboration with the collaborators of "Computational Mechanics Research Laboratory CMech-Lab" (ISEP/FEUP/INEGI), and its director, Prof.Dr. Jorge Belinha, and its senior advisors, Prof.Dr. Renato Natal Jorge and Prof.Dr. Lúcia Dinis.

Abstract

The Anterior Cruciate Ligament (ACL) total tear is one of the most frequent injuries happening in multidirectional sporting activities, such as Football and Basketball. The incidence of this kind of injuries is quite high and, ideally in all cases, it is necessary the ligament reconstruction with the aid of an orthopaedic surgery. One of the surgical techniques, the arthroscopic ACL reconstruction, enabled the ligament repair with a less invasive method.

The knee arthroscopic ACL reconstruction lacks optimization, since the femoral tunnel where the ligament is inserted is often mispositioned. For this reason, the physical and mechanical properties of the neo-ligament slowly decay, increasing the relapse risk. This originated the need of an instrument that would allow the orthopaedist to know, for each patient, the exact location to perform the graft incision.

To maintain the less-invasive condition of the arthroscopic ACL repair, incrementing the precision of the femoral tunnel incision, an instrument was developed in such manner that it would fit (folded) into the surgical devices with a cylindrical shape and, when in contact with the body-temperature, it would expand and adapt to the femoral geometry. Its function is to guarantee the exact positioning of the femoral tunnel in a customized way.

The instrument in development along the framework of this research project falls within the category of the Patient-Specific Instruments, a field with rising popularity in the international medicine. This customization ensures an individualized and more accurate treatment. These devices will be produced using Additive Manufacturing, because its flexibility to produce customized products and the need to adapt a device to a personalized bone.

The results were quite encouraging, once it was possible to obtain a geometry, a thermic gradient and the quantification of the material properties that allow the usage of the developed instrument.

Resumo

A rotura total do Ligamento Cruzado Anterior (LCA) do joelho é uma das lesões mais frequentes em desportos multidirecionais, como o Futebol e o Basquetebol, por exemplo. A incidência deste tipo de lesão é bastante elevada e, idealmente na totalidade dos casos, é necessária a reconstrução do mesmo recorrendo a uma intervenção cirúrgica ortopédica. Uma das técnicas, a cirurgia de artroscopia do joelho, permite a reconstrução do LCA de uma forma pouco invasiva.

A cirurgia artroscópica do joelho carece de otimização, uma vez que o posicionamento do túnel onde é reconstruído o ligamento nem sempre é o mais preciso. Este fator leva a que as propriedades físicas e mecânicas do LCA se vão degradando, aumentando o risco de uma recidiva. Isto originou a necessidade de um instrumento que permita ao cirurgião saber, para cada paciente, o local preciso para a incisão do enxerto.

Para que a cirurgia artroscópica se mantenha como pouco-invasiva, aumentando a precisão na incisão do túnel femoral, desenvolveu-se um instrumento que, inserido nos dispositivos cirúrgicos com uma forma cilíndrica, uma vez em contacto com a temperatura corporal, se expanda e adapte à geometria do fémur. A sua função é, de uma forma personalizada, garantir o local exato de execução do túnel em questão.

O instrumento em desenvolvimento ao longo deste trabalho insere-se na categoria dos *Patient-Specific Instruments*, um ramo de investigação em forte expansão na medicina internacional. Esta personalização garante um tratamento individualizado e, dessa forma, mais preciso. A produção em massa destes instrumentos será garantida através de Fabrico Aditivo devido à sua flexibilidade na produção de dispositivos customizados, os quais poderão ser função da geometria femoral do doente.

Os resultados foram bastante encorajadores, uma vez que se conseguiu obter uma geometria, um gradiente térmico e a quantificação das propriedades dos materiais necessários para a produção do dispositivo desenvolvido.

Table of Contents

1. Introduction 1

1.1 Objectives 2

1.2 Document Structure 2

2. Arthroscopic ACL repair 5

2.1 ACL injuries epidemiology 5

2.2 Knee anatomical structures 7

2.2.1 Knee anatomy 7

2.2.2 Anterior cruciate ligament anatomy 8

2.3 ACL arthroscopic surgery procedure 10

2.3.1 Existent techniques 11

2.3.2 Different graft types 12

2.4 Tunnel placement in ACL reconstruction 14

3. Thermomechanical shape-memory polymers 17

3.1 Shape-memory polymers 17

3.2 Programming cycle 18

3.3 Quantification of the shape-memory effect 19

3.4 Activating the shape-memory effect 20

3.5 Poly(lactic) acid 21

3.5.1 PLA's physical; mechanical and thermal properties 22

3.5.2 PLA's biocompatibility 25

3.5.3 PLA-based shape-memory materials for biomedical applications 26

4. Additive Manufacturing 29

4.1 General considerations on 3D Printing 29

4.1.1 Polymers for 3D printing 31

4.2 Fused Deposition Modelling description 32

4.2.1 FDM parameters 33

4.2.2 FDM processed parts' defects 34

4.3 Biomanufacturing 36

4.4 Patient-Specific Instrumentation 39

5. Finite Element Method 41

5.1 Solid mechanics fundamentals 41

5.1.1 Stress and Strain 41

5.1.2 Constitutive equations 44

5.1.3 Static equilibrium equations 44

5.2 FEM fundamentals 45
5.2.1 Strong and weak forms 45
5.2.2 FEM procedure 46
5.3 FEM for heat transfer problems 47
5.3.1 Field problems 47
5.3.2 Weight residual approach for FEM 47
5.3.3 Three-dimensional heat transfer problem 48
6. Software validation 53
6.1 Finite Element Method Analysis Software 53
6.2 Cook's Membrane - Convergence example 54
6.2.1 Meshing 56
6.2.2 Results and discussion 58
7. PSI development 67
7.1 PSI requirements 67
7.2 Small-scale 2D testing 69
7.2.1 Patch's shape selection 71
7.2.2 Patch's geometry and sizing alteration 79
7.3 Real-scale 2D testing 83
7.3.1 Temperature gradient alteration 85
7.4 3D geometry validation 87
7.5 Tunnel drilling hole 89
7.5.1 Temperature gradient alteration 91
7.5.2 Thermal expansion coefficient alteration 92
7.6 Unfolding process 95
7.6.1 Thermal expansion coefficient alteration 96
7.6.2 Ellipse shaped tunnel drilling hole 98
7.7 Drill guiding tabs 102
7.8 Position fixation tabs 104
7.9 Final device's 3D printing 109
8. Conclusions 113
8.1 Final Remarks 113
8.2 Future works 114
9. Bibliography 115
Appendix i
A. Incremental Procedure MATLAB© routine code i
B. Materials' Attribution MATLAB© routine code iii
C. Folded Geometry MATLAB© routine code v

D. Additional Material's Attribution routine vii

List of figures

Figure 1 - Left knee seen from behind [3]. 8
Figure 2 - Schematic drawing of ACL bundles insertion in lateral femoral condyle and in tibial plateau [5]. 9
Figure 3 - ACL arthroscopic repair [7]. 10
Figure 4 - Single-bundle (l.h.s) and double-bundle (r.h.s) ACL reconstruction [9]. 12
Figure 5 - Several types of ACL possible autografts [10]. 13
Figure 6 - Illustration of the anatomical structures of the ACL femoral landmark [12]. 15
Figure 7 - Molecular mechanism of the thermally induced shape-memory effect [13]. 18
Figure 8 - Typical stress-strain-temperature diagram, for a thermoplastic SMP with a thermally induced shape-memory effect [13]. 19
Figure 9 - Synthesis methods for PLA [15]. 22
Figure 10 - Generic curves showing the sequence of polymer-molecular weight; strength; and mass-reduction over time [15]. 23
Figure 11 - Schematic representation of acute and chronic phases of FBR [16]. 26
Figure 12 - Conceptual schematic of material feeding in commercial FDM [19]. 32
Figure 13 - Illustration of the difference between two distinct layer heights. [20] 33
Figure 14 - FDM process parameters [19]. 34
Figure 15 - Schematic showing the formation of the staircase effect on the build direction surface in SFF processed parts (right) when the CAD surface is planar (left) [19]. 35
Figure 16 - Schematic showing the formation of the chordal effect on xOy plane in SFF processed parts (right) as a result of linear approximation of the actual curved surfaces (left). 35
Figure 17 - Overview of biomanufacturing [21]. 37
Figure 18 - Cost-effectiveness chart for healthcare innovations [21]. 38
Figure 19 - Solid subjected to forces applied within the solid (body force) and on the solid's surface (surface force) [24]. 42
Figure 20 - Six independent stress components at a point in a solid viewed on the surfaces of an infinitely small cubic block [24]. 42
Figure 21 - Graphic user interface of FEMAS [25]. 54
Figure 22 – Two (left) and three-dimensional (right) geometry (in mm) of the Cook's membrane. 55
Figure 23 – Thickness (T) calculation with nodal distance t. 56

Figure 24 - Different meshes comparison between ANSYS (with a blue background) and FEMAS (with a white background). 58
Figure 25 - Horizontal (above) and vertical (below) displacements results for 2D simulations. 59
Figure 26 - Horizontal (above) and vertical (below) displacements results for 3D simulations. 60
Figure 27 - Effective-stress (Von Mises) (above) and Normal-stress along *Ox* (below) for two-dimensional simulations. 62
Figure 28 - Effective-stress (Von Mises) (above) and Normal-stress along Ox (below) for three-dimensional simulations. 63
Figure 29 – Triangular 2x2 FEMAS (a) and ANSYS© (c); 128x128 FEMAS (b) and ANSYS© (d) σef values; 2x2 FEMAS (e) and ANSYS© (g); 128x128 FEMAS (f) and ANSYS© (h) σxx values 64
Figure 30 - Quadrangular 2x2 FEMAS (a) and ANSYS© (c); 128x128 FEMAS (b) and ANSYS© (d) σef values; 2x2 FEMAS (e) and ANSYS© (g); 128x128 FEMAS (f) and ANSYS© (h) σxx values. 65
Figure 31 – Tetrahedral (3D) 2x2 FEMAS (a) and ANSYS© (c); 32x32 FEMAS (b) and ANSYS© (d) σef values; 2x2 FEMAS (e) and ANSYS© (g); 32x32 FEMAS (f) and ANSYS© (h) σxx values 66
Figure 32 - Hexahedral (3D) 2x2 FEMAS (a) and ANSYS© (c); 32x32 FEMAS (b) and ANSYS© (d) σef values; 2x2 FEMAS (e) and ANSYS© (g); 32x32 FEMAS (f) and ANSYS© (h) σxx values 66
Figure 33 - Intercondylar notch proximal (35.17mm) and distal (44.50mm) portions length of a Femur model from CMECH-Lab database. 69
Figure 34 - Illustration of the length variation in both patches' shapes (rectangular l.h.s and splined r.h.s). 72
Figure 35 - Total displacement (above) and Effective-Stress (Von Mises) (below) evolution curves with patch's length increment. 72
Figure 36 - Illustration of the width variation in both patch shapes (rectangular l.h.s and splined r.h.s). 73
Figure 37 - Total displacement (above) and Effective-Stress (Von Mises) (below) evolution curves with patch's width increment. 74
Figure 38 - Effective-Stress (Von Mises) obtained with a 0.9mm length patch, with a width of 0.1mm. (Min = 6.572 MPa; Max = 35.238 MPa) 75
Figure 39 - Illustration of several patches (l.h.s) and different widths in one single patch (r.h.s). 75
Figure 40 - Total displacement (above) and Effective-Stress (Von Mises) (below) evolution curves with several patches' configuration. 76
Figure 41 - Total displacement (above) and Effective-Stress (Von Mises) (below) evolution curves with one single patch with width variations..... 77

Figure 42 - Effective-Stress (Von Mises) obtained with width variation between 0.125/0.1mm and patch's length of 0.1mm. (Min = 7.538 MPa; Max = 33.784 MPa) 77
Figure 43 - Effective-Stress (Von Mises) obtained with a 0.9mm length patch, with a width of 0.1mm using the Incremental Procedure. (Min = 8.496 MPa; Max = 41.046 MPa) 78
Figure 44 - Effective-Stress (Von Mises) obtained with a 0.9mm length patch, with a width of 0.1mm using the Incremental Procedure, with a temperature gradient of 250ºC. (Min = 52.617 MPa; Max = 243.431 MPa) 79
Figure 45 - New sample's configuration with a void between materials 1 and 2, used as model to the first calculations. 80
Figure 46 - Illustration of the deformation along the length of both materials, resultant from the heat-transfer process. 81
Figure 47 - Illustration of the real deformation happening during the heat-transfer process. 82
Figure 48 - Samples' geometry used in first 2D real-scale tests. 83
Figure 49 - Effective-Stress (Von Mises) for the 17mm model (l.h.s) with the Incremental Procedure, under a temperature gradient of 37ºC and a Zoom-In the final patch (r.h.s). (Min = 7.186 MPa; Max = 30.089 MPa) 84
Figure 50 - Samples' geometry used in carved 2D real-scale tests. 84
Figure 51 - Effective-Stress (Von Mises) for the 17mm carved model (l.h.s) with the Incremental Procedure, under a temperature gradient of 37ºC and a Zoom-In the final patch (r.h.s). (Min = 6.283 MPa; Max = 30.194 MPa) 85
Figure 52 - Effective-Stress (Von Mises) for the 17mm carved model (l.h.s) with the Incremental Procedure, under a temperature gradient of 80ºC and a Zoom-In the final patch (r.h.s). (Min = 16.860 MPa; Max = 65.612 MPa) 86
Figure 53 - Geometry's side dimensions to perform the first 3D tests. 87
Figure 54 - 3D device modelled in SOLIDWORKS© with its dimensions. .. 88
Figure 55 - Final geometry's materials after a FEM simulation with the Incremental Procedure with Materials' Attribution. 88
Figure 56 - 3D Effective-Stresses (Von-Mises) colormaps generated with FEMAS, in a 3D view (l.h.s) and a top view (r.h.s). 89
Figure 57 - 2D illustration of boundary conditions imposed to the structure to be modelled in SOLIDWORKS© and analysed in FEMAS. 90
Figure 58 - 3D half device modelled in SOLIDWORKS© with is dimensions and the tunnel drilling hole. 90
Figure 59 - tunnel drilling hole dimensions and positioning in the SOLIDWORKS© model. 91
Figure 60 - Effective-Stresses (Von-Mises) colormaps generated with FEMAS, in a 3D view of the entire component with the tunnel positioning hole (l.h.s) and a top view (r.h.s), under 80ºC of temperature gradient. 91

Figure 61 - Effective-Stresses (Von-Mises) colormaps generated with FEMAS, in a 3D view of the entire component with the tunnel positioning hole (l.h.s) and a top view (r.h.s), under 127ºC of temperature gradient. 92
Figure 62 - Effective-Stresses (Von-Mises) colormaps generated with FEMAS, in a 3D view of the entire component with the tunnel positioning hole (l.h.s) and a top view (r.h.s), under 127ºC of temperature gradient and with material 2's TEC of 170e-6 strain/ºC. 93
Figure 63 - Effective-Stresses (Von-Mises) colormaps generated with FEMAS, in a 3D view of the entire component with the tunnel positioning hole (l.h.s) and a top view (r.h.s), under 127ºC of temperature gradient and with material 2's TEC of 250e-6 strain/ºC. 94
Figure 64 – Linear (l.h.s), before, and cylindrical geometry, from a 3D perspective (centre) and a top view (r.h.s), after the Folded Geometry routine that folded the device previously to the simulation. 95
Figure 65 - Effective-Stresses (Von-Mises) colormaps generated with FEMAS, in a 3D view of the entire component with the tunnel positioning hole (l.h.s) and a top view (r.h.s), starting from a cylindrical shape, under 127ºC of temperature gradient and with material 2's TEC of 250e-6 strain/ºC. 96
Figure 66 - Effective-Stresses (Von-Mises) colormaps generated with FEMAS, in a 3D view of the entire component with the tunnel positioning hole (l.h.s) and a top view (r.h.s), starting from a cylindrical shape, under 127ºC of temperature gradient and with material 2's TEC of 320e-6 strain/ºC. 97
Figure 67 - Effective-Stresses (Von-Mises) colormaps generated with FEMAS, in a 3D view of the entire component with the tunnel positioning hole (l.h.s) and a top view (r.h.s), starting from a cylindrical shape, under 127ºC of temperature gradient and with material 2's TEC of 420e-6 strain/ºC. 98
Figure 68 - Graphical illustration of the determination of ellipse diameter (Df) using the expansion of the tunnel drilling hole. 99
Figure 69 - 3D device modelled in SOLIDWORKS© with ellipse shaped hole positioning (above) and Df diameter dimension (below). 100
Figure 70 - Effective-Stresses (Von-Mises) colormaps generated with FEMAS, in a 3D view of the entire component with the ellipse tunnel positioning hole (l.h.s) and a top view (r.h.s), starting from a cylindrical shape, under 127ºC of temperature gradient and with material 2's TEC of 420e-6 strain/ºC. 101
Figure 71 - Effective-Stresses (Von-Mises) colormaps of the ellipse tunnel positioning hole, shown in the l.h.s of Figure 70, with the highlighting of the distorted elements..... 101
Figure 72 - 3D device modelled in SOLIDWORKS© with the ellipse shaped hole and the guiding tabs positioning (above) and their dimensions (below). 102
Figure 73 - Drill placement in between both guiding tabs. 103

Figure 74 - Effective-Stresses (Von-Mises) colormaps generated with FEMAS, in a 3D view of the entire component with guiding tabs (l.h.s) and a top view (r.h.s), starting from a cylindrical shape, under 127ºC of temperature gradient and with material 2's TEC of 420e-6 strain/ºC. 103
Figure 75 – Illustration of the drill axis orientation. 104
Figure 76 - 3D device modelled in SOLIDWORKS© with the ellipse shaped hole, the drill guiding tabs and the fixation tabs positioning (l.h.s) and their dimensions (r.h.s). 105
Figure 77 - Linear geometry with the fixation tabs with elements of both materials in FEMAS. 106
Figure 78 - Effective-Stresses (Von-Mises) colormaps generated with FEMAS, in a 3D view of the entire component with guiding and fixation tabs (l.h.s) and a top view (r.h.s), starting from a cylindrical shape, under 127ºC of temperature gradient and with material 2's TEC of 420e-6 strain/ºC. 106
Figure 79 - Material distribution illustration with the three different materials used in the device, in the linear configuration. 107
Figure 80 – Geometry generated with FEMAS, in a 3D view of the entire component with guiding and fixation tabs (l.h.s) and a top view (r.h.s), starting from a cylindrical shape, under 127ºC of temperature gradient and with material 3's TEC of 50e-3 strain/ºC. 108
Figure 81 – Geometry generated with FEMAS, in a 3D view of the entire component with guiding and fixation tabs (l.h.s) and a top view (r.h.s), starting from a cylindrical shape, under 127ºC of temperature gradient and with material 3's TEC of 100e-3 strain/ºC. 109
Figure 82 - SOLIWORKS© final model previous to the 3D printing. 110
Figure 83 - Slic3r software interface with the final model before printing. 110
Figure 84 - Slic3r detailed legend of the model's different entities 111
Figure 85 - Printed part on 3D printer immediately after the processing (l.h.s) and detailed image (r.h.s). 112

List of tables

Table 1 - Properties of Polylactide obtained in CES 2018 Edupack©. (* marked values are estimates). 24
Table 2 - Material properties used o tests. 55
Table 3 - Meshing parameters for two-dimensional simulations. 57
Table 4 - Meshing parameters for three-dimensional simulations..... 57
Table 5 – Materials' mechanical and thermal properties used in small-scale tests [27]. 70
Table 6 – Materials' mechanical and thermal properties used in the tunnel drilling hole tests, first alteration of material 2's TEC. 93
Table 7 – Materials' mechanical and thermal properties used in the tunnel drilling hole tests, second alteration of material 2's TEC. 94
Table 8 – Materials' mechanical and thermal properties for the unfolding test, first alteration of material 2's TEC. 97
Table 9 – Materials' mechanical and thermal properties for the unfolding test, second alteration of material 2's TEC. 97
Table 10 – Hole's shape changing calculation values..... 99
Table 11 - Materials' mechanical and thermal properties for the fixation tabs test, first satisfactory alteration of material 3's TEC. 107
Table 12 - Materials' mechanical and thermal properties for the fixation tabs test, final value of material 3's TEC. 108
Table 13 - 3D printing parameters for the printing of the final model. 111

Chapter 1

1. Introduction

Medicine worldwide is currently going through an innovation process where the customization of the instruments used in several medical applications is growing rapidly. The medical areas where these devices are used go from orthopaedics to neurosurgery, passing by the angiology and oncology.

It is expected an increment in the global market volume for medical equipment given the fact that a higher investment in the development of new techniques and products will make it possible to improve life-quality in the world population.

This work presents the theoretical approach for the development of a patient-specific (customized) instrument produced by Additive Manufacturing (AM) to be used in an orthopaedical knee surgery of arthroscopic reconstruction of the Anterior Cruciate Ligament (ACL).

The patient-specific instrumentation (PSI) is a new trend in the medical market and it is seen as a cheaper alternative to robotic technologies and a more accurate technique when compared to traditional instrumentation because it allows the healthcare provider to accomplish a given function in a personalized way. A drawback regarding PSI is the direct cost in the acquirement and production of the materials and devices. Nevertheless, it is expected, as it will be stated bellow, to increment the efficiency in the operating room time. This fact makes it economically viable to invest in patient-specific instrumentation.

Usually, after obtaining the medical images by magnetic resonance imaging (MRI) or computed tomography (CT), a device is designed according to the geometry of the body structures of the patient and produced with 3D (three-dimensional) printing and AM technologies. The materials of the products should be, in general, biodegradable, biocompatible and its behaviour under corrosion environment should be well-known. Generally, the polymers are the most used group of materials because they fulfil these specific requirements. One of the most commonly used polymers for biomedical applications is the poly(lactic) acid (PLA) because of its biocompatibility and processability, as well as its shape-memory effect, that is easily programmed in this kind of material. This work will explore PLA's characteristics later on.

The ACL is the most important ligament of the knee joint when it comes to stability. It restricts horizontal translation and relative rotation between femur and tibia. The incidence of ACL injuries in professional athletes can reach the 3.67% (B. Moses et al.) and it affects more the female gender comparatively with males when exposed to the same activity. To regain all the stability and functional activity of the knee after an ACL total rupture it is required a surgery procedure. This procedure is performed in a large spectrum of different techniques and one of the worldwide most popular one is the arthroscopic ACL repair. The purpose of this thesis is to develop a device that can provide a 100% accurate tunnel placement for the new ACL graft provided this is one of the most relevant causes of the decreasing of ligament mechanical properties during time after surgery.

1.1 Objectives

The main objective of this thesis is to design and study a Patient-Specific Instrument that allows orthopaedic surgeons to position the femoral tunnel drill in an exact spot and with a specific angle in order to increase their precision in Arthroscopic ACL reconstructions.

The detailed objectives are:

- PLA based instrument development, with two materials with different Thermal Expansion Coefficients;
- to explore PLA's specifications in medical applications;
- to use different computational tools to perform structural tests and analysis;
- design of the device's structural topology to enhance its performance;
- thorough study of the different possibilities to be considered to accomplish the requirements that are imposed to the Arthroscopic knee surgery.

Once accomplished the original objectives some constructive solutions were tested in order to fix the PSI in a given position inside the knee joint and a 3D printing of the completed model was performed as a proof of concept.

1.2 Document Structure

The thesis is divided in eight main chapters: Introduction; Arthroscopic ACL repair; Thermomechanical shape-memory polymers; Additive Manufacturing; Finite Element Method; Software validation; PSI development and Conclusions.

The first chapter allows the **Introduction** and the presentation of the purpose of this work with a brief state-of-the-art presentation regarding the ACL arthroscopic reconstruction and Patient-Specific Instrumentation.

In the chapter that regards the **Arthroscopic ACL repair**, the concepts and the current technologies and techniques concerning this medical application are detailed in order to provide the reader with concepts related to healthcare and medicine.

Thereafter, the basic notions regarding **Thermomechanical shape-memory polymers** are detailed in the third chapter, as well as a comprehensive demonstration of PLA's properties, biocompatibility and its usage in biomedical applications.

Some concepts pertaining to **Additive Manufacturing** were as well exposed in the fourth chapter of this thesis. This chapter is important because the reader can understand why this technology is key nowadays for products' customization.

The fifth chapter details the **Finite Element Method** fundamentals and provides a description about the mathematical formulations that are behind the software used in the thesis, as well as an exhaustive review of the concepts regarding Finite Element Method for Heat Transfer Problems.

Regarding the **Software Validation** chapter, it provides an introduction and an explanation about the academic software that was used to perform the FEM analysis throughout this work. Afterwards, a mechanical benchmark example was studied comparing the academic and a commercial software to assess the results generated, followed by a comparison between both.

Once presented all the preliminary chapters, that are supposed to be a complement to sustain the device's development, the seventh, and most important chapter is an extending review of the **PSI development** process, from the small-scale two-dimensional tests to the real-scale 3D tests that were performed with all the calibrated parameters (geometric, material and numerical parameters) obtained in the previous steps of this work.

Lastly, the final chapter is where all the main **Conclusions** and future works are presented and suggested.

Chapter 2

2. Arthroscopic ACL repair

One of the various techniques to repair ACL injuries is using an arthroscope, making this procedure minimally invasive to diagnose. Also, it allows to treat some of the conditions affecting the several human body joints. The surgery of these ligaments is especially difficult given the placement of the natural ligament in the human knee. ACL repair can be made using different types of grafts, and the range of techniques existent to perform it is vast. Along this chapter, it will be detailed the knee and ACL anatomy, as well as the different kind of knee arthroscopy and ACL grafts types used nowadays.

2.1 ACL injuries epidemiology

A ligament is a band of tough, flexible fibrous tissue that connects two different hard-tissues (bones) one to another within a body keeping the structures stable. Particularly, the Anterior Cruciate Ligament (ACL) is an important knee structure and connects the femur to the tibia on the knee joint. The ACL is a very important stabilizer of the femur on tibia and serves to prevent the tibia from rotating and sliding forward during jumping, running and other quick or sudden physical movements and it is the most frequently injured ligament [1].

Anterior Cruciate Ligament injuries of the knee are amongst the most common major injuries in sport. They are of particular concern in multidirectional sports, such as basketball, soccer, American football, Australian football and rugby [2].

In what concerns the numbers of the incidence of ACL injuries in the Portuguese population no studies were found during the research and, for this reason, the approach scrutinized was the analysis of a paper that compares

the annual incidence of ACL injuries and surgeries in various populations worldwide.

Orchard et al. compared 112 studies that reported incidence data regarding the ACL injuries and surgeries on populations from 16 different countries related to 51 specific populations (18 general/national/mixed and 33 from specific sports). These studies were only scrutinized if they reported the annual incidence rate in terms of the percentage of individuals who suffer an ACL injury (or surgery) per year; an incidence rate on a unit similar to injuries (or surgeries) per 100,000 years (to be directly converted to an annual percentage) or presented per athlete exposure or 1,000 player hours to be converted into an annual incidence. Because it was easier to convert the units where the incidence was presented in the studies the common comparison unit chosen by the authors was the population annual incidence [2].

Regarding the Population Studies at the National Level, the authors of this paper found that the annual national population incidence for surgery or injury range from 0.01 to 0.05% and the median annual incidence was 0.03% for the different countries studied. Although these rates appear low, it should be noticed for further interpretation, that the values include persons of all ages (e.g. babies and elderly people) and people who do not engage in sporting activities. Once these sub-rates are assessed for highly active groups (e.g. males aged 15-40) the rates are substantially higher. The obvious explanation for different national population figures relates to variations in sports exposure, because there are countries that have high annual rates of participation in the various forms of football, snow sports, and court sports and will tend to have higher rates of ACL injury. Another important aspect is the climate, which may play a role in these number in terms of exposure (countries with temperate weather will perhaps have longer playing seasons leading to a higher number of exposure hours). It is established that females have a higher rate of ACL injuries than males when exposed to the same sport. However, at a population level, males generally have a higher annual ACL injury incidence than females, which is almost certainly due to an exposure bias in which males are more likely to play higher risk sports, especially the various forms of football. An important conclusion is that, where reported national population annual ACL incidence for young males were higher than the comparative rates for young females [2].

In relation to particular sporting/activity groups, people that belong to the military forces have annual incidence figures calculated in a range from 0.30% to 2.14%. As it is easy to notice, these values are substantially higher than the general population ratios and are broadly comparable to the figures for professional/elite sports. The incidence of ACL injuries/surgeries for professional sporting individuals (particularly for multidirectional team sports such as football or basketball) - ranging from 0.15% to 3.67% - are

substantially higher than national population levels, as for military populations, whereas for amateur athletes the range of annual incidence goes from 0.03% to 1.62% which is quite lower than the professional sport incidence rates but higher than the national population. At first sight it would be intuitive to think that the poor movement coordination and physical preparation could be a risk factor for ACL injury, but these factors do not appear to outweigh the greater intensity and exposure of high-level play. In addition, professional athletes are more likely to have an ACL injury diagnosed, as well as there is a greater likelihood of a reconstructive surgery being required in high-level athletes. Finally, it is likely that professional and elite athletes (who play more games annually and train for longer periods of time than amateur) increase their exposure to injury [2].

The reconstruction of the ACL, particularly the arthroscopic procedure, is a very frequent non-invasive surgery performed all over the globe to help people restoring the full functionality of the injured knee and make them able to perform every kind of activity with the less amount of discomfort and pain as possible. Given these figures it is possible to conclude that everything that can make this procedure even less invasive, more precise and effective, will be a good income for orthopaedic surgeons, who expect that these innovations will decrease the postoperative morbidity and a quicker patients' rehab. As it was stated above, the customization of instruments in the orthopaedic procedures is a tendency in the medical world and in knee arthroscopy for ACL reconstruction a PSI would come out as an important step forward to increase the effectiveness of the clinical process.

2.2 Knee anatomical structures

2.2.1 Knee anatomy

As previously mentioned, the human knee is stabilized with four different ligaments, as it is shown in the figure below: the anterior and posterior cruciate ligament (PCL), the medial collateral ligament (MCL) and the lateral collateral ligament (LCL). The first two are placed in the "centre" of the knee and the collateral ligaments are located in the inner knee and in the outer knee, respectively (see Figure 1).

The PCL controls the backward movement of the tibia (the shin bone), while the medial and lateral collateral ligaments give stability to the inner and outer knee. The ACL functions will be detailed subsequently.

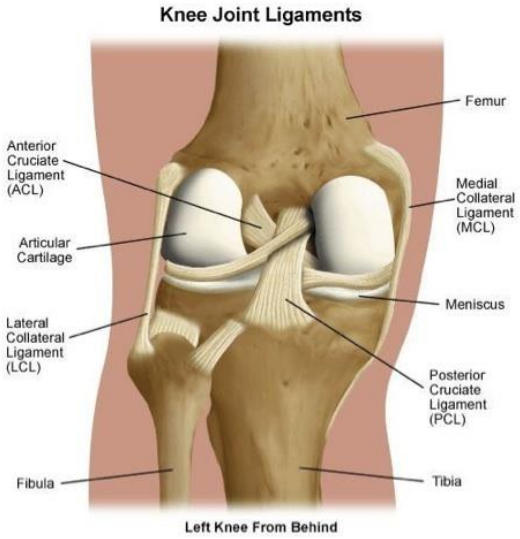


Figure 1 - Left knee seen from behind [3].

Apart from the 4 major ligaments, there are other entities such as bones and cartilage. The femur (thigh bone), tibia (shin bone) and patella (knee cap) make up the bones of knee joint. The patella is a triangle shaped bone and it is located in the most anterior part of the knee, within the quadriceps muscle. Its function is to withdraw a great deal of the loads and this is why it is covered with the thickest layer of cartilage present in the human body.

There are two types of cartilage in the knee, the meniscus and the articular cartilage. The meniscus consists in crescent-shaped discs that act as cushion in the absorption of shock to let the bones of the knee move across all their range of motion (ROM) without rubbing directly against each other. The menisci (medial meniscus – on the inner side; lateral meniscus – on the outer side) also help in the body balance because of the containing nerves as well as giving stability and ensure the correct weight distribution between femur and tibia. The articular cartilage, which is placed on the femur, on top of the tibia and in the back of the patella, is a thin layer of cartilage and its function is to absorb shock and to help the smooth movement of bones between each another.

2.2.2 Anterior cruciate ligament anatomy

The ACL is responsible for providing stability of the knee joint by controlling excessive knee motion. This ligament is important in knee stability because it restricts both horizontal translation (anterior-posterior and medial-lateral) as well as the restriction of relative rotation (varus-valgus and internal-external) of the knee entities (femur and tibia). The anterior cruciate ligament is often subjected to overloading during heavy physical activities

and sports, resulting in a sprain or tear of the ligament. The tear happens during a rapid change in direction when moving, slowing down when running, landing after a jump, or receiving an abrupt force of the knee [4]. The healing ability of this ligament is quite poor, since it is enveloped by synovial fluid and lacks significant vascularization.

The mechanical properties of the natural ACL reported in the literature consulted to the production of this work are of 1730N of tensile strength; strain between 20 to 25% and the stiffness between 129 and 182 N/m [1].

The native insertion of the AC ligament is on the posteromedial portion of the lateral femoral condyle in the intercondylar notch and inserts on the anterior aspect of the tibial plateau, being the femoral footprint 3.5 times larger than the midsubstance that has a cross-sectional area of 35mm^2 and an average length of 12mm, being the ACL average length from 31 to 38mm. The centre of the ACL lies about 9mm posterior to the intermeniscal ligament and 7-8mm from the PCL, nearly 6mm anterior to a projected line from the apex of the medial tibial eminence. The tibial insertion is 120% larger in area comparing to the femoral insertion.

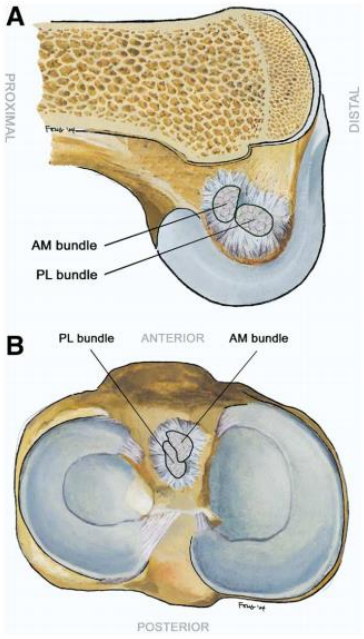


Figure 2 - Schematic drawing of ACL bundles insertion in lateral femoral condyle and in tibial plateau [5].

The ACL is composed by two bundles (see Figure 2) named Anteromedial (AM) and Posterolateral (PL). During flexion on 90º the insertion points are horizontal to each other whereas in extension they are oriented vertically. The first one has a length of 33mm and comprises 49% of the femoral footprint. It is tightened in flexion and slack in extension, being

the opposite true for the PL bundle. For this reason, the AM is more important in flexion. Its function is to stabilize anteroposterior tibial motion. The PL bundle has greater effect during extension and has a length of 18mm. It also allows to control tibial rotation. Both of the bundles are oriented orthogonally during extension and in flexion they are crossed [6].

2.3 ACL arthroscopic surgery procedure

The first knee arthroscopy was performed in the 1980s and it is a minimally invasive procedure used to diagnose and repair conditions affecting the human knee. It is handled with the aid of a small tube-shaped instrument that assists the healthcare provider visualizing with detail internal structures of the joint. This instrument is called arthroscope. The arthroscopy consists in a system of lenses, a small video camera and a light for viewing, apart from the other instruments needed to perform the medical procedure.

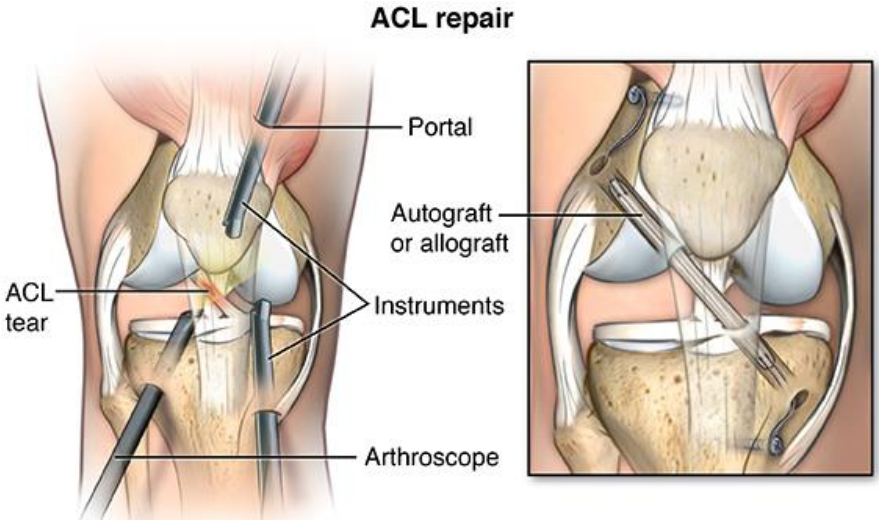


Figure 3 - ACL arthroscopic repair [7].

During a knee ligament repair the healthcare provider will perform a few small incisions in the knee surroundings, and the surgery using an arthroscope will be performed under general anaesthesia or under spinal anaesthesia. Selecting a given type of graft (which will be discussed subsequently in this work) the orthopaedic surgeon may reattach the torn ligament, or reconstruct it depending on the degree of the injury.

The repairing or reconstruction of the ligament is performed after the drilling of small holes close to the tibia and femur natural insertion sites and the graft will be threaded through the holes and attached with surgical shapes, screws, or other means. The human body will, later on, naturally grow

bone tissue around the graft helping on the cicatrisation process and providing the fixation devices with more stability.

2.3.1 Existent techniques

During the early 1980s, the ACL reconstruction was performed without the use of the arthroscope. However, this device, developed in the 1970s for interventions regarding the meniscus repair, started to play a role in ACL surgery during this decade. This kind of surgery allows a faster rehabilitation, decreases the postoperative morbidity, and provides a better ROM immediately after the surgery. Furthermore, on the esthetical point of view, the patient would have barely noticeable scars, instead of a full knee length sized. The disadvantages of this technique is related with the lack of visualization range inside the joint.

Primarily the arthroscopic ACL repairing were performed with a two incisions technique, where the tibial tunnel and the graft harvesting were made in the first one, whereas the second incision was responsible for the drilling of the femoral tunnel with an "outside-in" technique. This previous procedure was smoothly replaced by a one incision technique called "all-inside" or trans-tibial (TT), where the tibial tunnel was drilled through a single incision and the femoral tunnel was subsequently drilled via tibial tunnel. This technique is limited given the fact that the drilling of the second tunnel is dependent on the position of the tibial tunnel, which promotes a location of the future graft insertion site different from the natural one, where the femoral tunnel is usually placed too high and deep into the intercondylar ridge, that is a structure located just anteriorly to the femoral insertion site of the AC ligament.

There are two different types of ACL reconstruction, both based on the length of the ligament during the range of motion of the joint. The isometry concept states that the ligaments in the body are taut and maintain their length during all the ROM. This "concept of isometry" is important in ACL, as full ROM can be achieved without causing long term deformation. Isometry does not exist regarding the ACL because there is not a single femoral point that maintains the distance to another given point in the tibial plateau during all the flexion-extension movement. The AM bundle is tightened during flexion and slack in extension and its fibres have relatively vertical attachment on the femur and are more isometric. While the initial literature proposed ACL reconstruction with graft isometry, the recent papers prove that graft isometry is not the most crucial factor. Instead, the anatomical attachment of the ACL allows it to mimic better its biomechanical properties with the restoration of the native tensile properties, and the popularity of isometric placement rapidly decreased. However the results of studies made

for the correct placement of the insertion sites with the anatomical or isometric technique showed that the focus of the research should be on the contribution of respective insertion sites in transmitting load from the ACL substance to bone and to determine how fibre length changes during knee ROM [8].

There is also the possibility to mimic the native ACL anatomy with a single or a double-bundle technique. The anatomical double-bundle reconstruction has as result a closer anatomy of the reconstructed ligament to the natural one but is a much more challenging and time-consuming procedure for the surgeon when compared with single-bundle reconstruction, where four bone tunnels should be drilled at native footprints and the grafts are harvested and prepared afterwards into two separate bundles. The AM and PL bundles are tensioned and inserted separately. It should be noticed that a two-bundle reconstruction is not necessarily an anatomical reconstruction, but the definition of anatomical is much broader in meaning. The advantage of the double-bundle technique is that the rotational stability is increased significantly when compared to a single bundle, however the possible difference in clinical outcome of both techniques is questionable. Another positive point of two separately tensioned bundles are also suggested to distribute the graft load in a more natural manner during knee range of motion compared to simply one bundle and thereby preventing excessive stretching and elongating of the grafts [8].

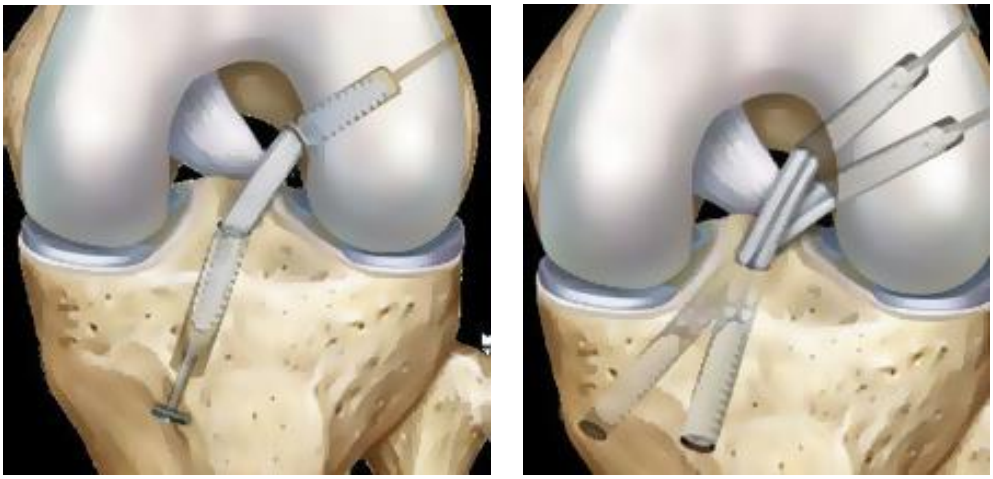


Figure 4 - Single-bundle (l.h.s) and double-bundle (r.h.s) ACL reconstruction [9].

2.3.2 Different graft types

The ideal graft selection for the replacement of the ACL should reproduce the complex anatomy of the natural ligament with the same biomechanical properties. Accelerated rehab should be a priority, while a rapid biologic

incorporation of the graft occurs due to a right selection of the material. The donor site morbidity should be minimal.

The graft type for a neo-ACL can be divided in three different groups: autografts; allografts and artificial grafts.

The autografts are from patient's own tissues (usually the middle-third of the patella tendon, the hamstring tendons or quadriceps tendon, see Figure 5) and should provide good results, however, they do not eliminate some risks regarding morbidity; secondary knee pain; patellar tendonitis and fracture or hamstring tendon weakness. When choosing between patellar or hamstring tendon it should be noticed that this last has more graft strength, stiffness and cross-sectional area, less morbidity and preservation of extensor mechanism, while opting for the patellar tendon could prevent the hamstring weakness and result in a decreased tendon-tunnel healing time [5].

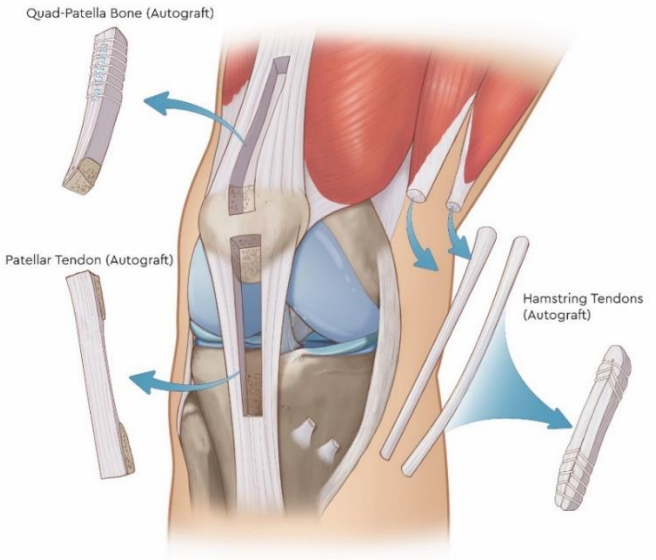


Figure 5 - Several types of ACL possible autografts [10].

Regarding allografts they usually come from cadaveric tissue from a tissue bank and have several drawbacks such as the limited donor tissue sources, the transmission of diseases, tissue rejection but, in general, it results in less time in operating room.

Artificial grafts should mimic the nature ACL properties and are made from synthetic fibres. They were widely clinically adopted in 1980s and 1990s acting as an alternative to allografts and autografts because of the donor site morbidity and disease transmission. This type of ligaments can be split in four different groups: permanent type, scaffold type, ligament augmentation device (LAD) type and permanent scaffold type and are usually made of carbon fibre, polyethylene glycol terephthalate (PET) and poly-tetrafluoroethylene. Besides the aforementioned products, a novel type of

artificial ligaments, called tissue-engineered ligaments, still remains in the developmental stage [11]

The graft tensioning should provide initial stability and strength of fixation and not strength in the graft itself. It was found that a reconstructed ACL should withstand 454N of tensile strength for daily living. The femoral sided is different from the tibial sided fixation because the femoral side is denser, and this affects the biomechanical properties of screws in the tibial tunnel. The initial tensioning affects joint kinematics, graft's survivorship and the degradation rates. An increasing of the graft tensioning reflects an impaired motion and a damage in the cartilage tissues, whereas a low initial tension can induce residual laxity of the reconstructed ligament.

2.4 Tunnel placement in ACL reconstruction

As already indicated, the incorrect positioning of both tunnels for graft fixation is seen as one of the most common reason for suboptimal outcome of the ACL reconstruction and is the main purpose of this thesis. The placement of femoral tunnel too anteriorly in the sagittal plane can lead to a restriction in knee and graft's tightness during flexion movement.

The TT drilling results, usually, in an anatomic placement of the femoral tunnels and in recent years, the TT drilling has been increasingly replaced by anatomic femoral tunnel as such tunnels are believed to offer increased rotational stability, translational and tensioning patterns similar to the native ACL [6].

The isometric tunnel placement was previously indicated as the technique with the better surgical outcome, but in the recent years it is thought that the anatomical procedure increases the resistance to rotational forces and reduces the risk of later osteoarthritis.

The insertion site of the natural ACL and the lateral intercondylar ridge (also known as Resident's Ridge) act as useful leading points to the accurate positioning of the femoral tunnel. The perception of the positioning of Resident's Ridge is important given that inexperienced surgeons can be misled to place femoral tunnels in incorrect positions and with the knowledge of these landmarks the positioning of the tunnels can be more accurate. There is another ridge, the lateral bifurcate ridge that separates AM of the PL femoral bundles and it is also used as a landmark for the femoral attachments.

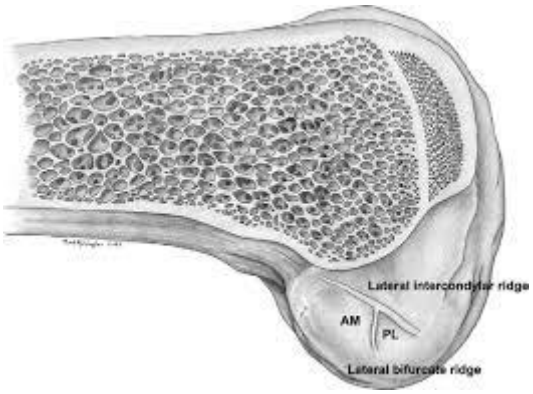


Figure 6 - Illustration of the anatomical structures of the ACL femoral landmark [12].

For the tibial tunnel, it is very important to successfully accomplish the objectives of the surgery outcome and avoid complications (knee pain, incomplete ROM, and graft impingement). The ideal positioning of the tibial tunnel should be at the centre of the natural footprint of the ACL in the intercondylar area. The outside entry into the tibial tunnel is placed about 4 cm from the tibial joint line and 2 cm medial to the tibial tubercle. Of course, an ideal tibial tunnel positioning should prevent the neo-ligament to impinge PCL [6].

Chapter 3

3. Thermomechanical shape-memory polymers

Thermomechanical shape-memory polymers (SMPs) have a network with netpoints and molecular switches. These latest entities can either be relaxed or fixed and this ability allows the material to change from a natural to a programmed shape, after a programming cycle that is developed based on a transition temperature (T_{trans}), that can be the glass transition temperature (T_{glass}) or the melting temperature (T_m) of the material.

The shape-memory effect can be activated under a large range of different stimuli and the changing of shape, as well as the recovery of natural shape ability are quantified in a specific way.

In this chapter, these topics will be analysed in a more scrutinized way for further understanding of the possibilities of these characteristics' application in the medical device under study.

3.1 Shape-memory polymers

This type of materials is emerging as a class of active polymers that have dual-shape capability. A shape-memory polymer has the ability to change its shape in a pre-programmed way from a permanent shape A to a working-shape B when exposed to appropriate stimuli. This capability is not intrinsic but results from a combination of the polymer structure and its specific processing considered as polymer functionalization.

Shape A is a temporary shape obtained by mechanical deformation and subsequent fixation of that state. This process also determines the shape's shifting, resulting in shape B, which is the permanent shape. Eventually, these kinds of polymers, with the right programming cycle can assume up to

three or four different shapes, giving their users the possibility to apply them in a wide range of different devices and conditions [13].

The permanent shape is a result of conventional processing method and, afterwards, through a programming process, the sample is deformed and fixed into a temporary shape A. When exposed to an external stimulus the polymer recovers its natural shape B and this programming recovery can be repeated several times, with different temporary shapes in subsequent cycles. The polymer's programming cycle can happen in a much shorter period of time when compared with metallic shape-memory alloys and this specific kind of polymers allows a much higher deformation rate when compared with metallic materials.

The polymer network is equipped with suitable stimuli-sensitive molecular switches and netpoints based on a physical interaction. The latter entity determines the permanent shape of the entire network and can be of a chemical (covalent bond) or physical (intermolecular interactions) nature. The netpoints act as polymers' hard segment and their domains have the highest thermal transition temperature (T_{perm}), whereas the chain segments with the second highest thermal transition (T_{trans}) act as molecular switches. If the working temperature is higher than T_{trans} the switching segments will be in a flexible form and an entropic elastic behaviour of the polymer will be developed, and the material will perform the shape changing [13].

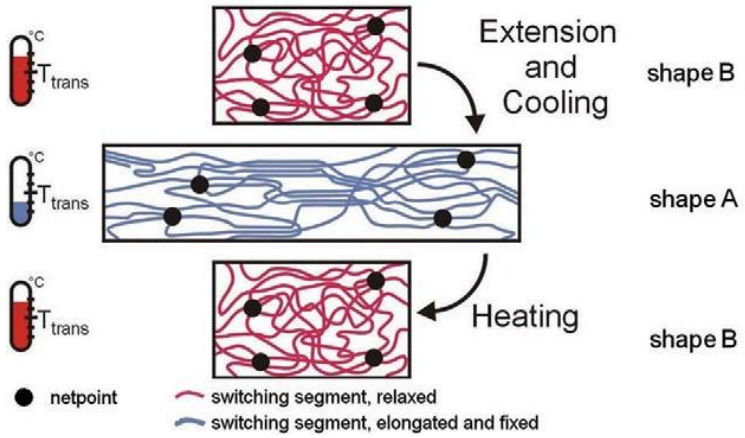


Figure 7 - Molecular mechanism of the thermally induced shape-memory effect [13].

3.2 Programming cycle

In a typical stress-controlled programming cycle, the specimen is fixed into a tensile tester and elongated to ε_m (maximum strain) with the molecular switches opened (step 1) of Figure 8. This opening is performed in thermally induced shape-memory materials with their heating to a temperature higher than T_{trans}, T_{high}. For instance, in light-induced shape-memory materials, the

opening of molecular switches is achieved with irradiation of suitable wavelengths to cleave photosensitive bonds.

After this, the strain is maintained for a small timeframe for the polymer chains to relax and afterwards the experiment is continued with a stress-controlled mode. Under constant stress (σ_m) the temporary shape is fixed by closing of the molecular switches (step 2). The closing of the molecular switches occurs in thermally induced shape-memory materials with a controlling cooling down to a temperature below T_{trans}. Then, the strain is reduced until a stress-free condition achieved under 0 MPa (step 3) of Figure 8. Finally the molecular switches are opened again, in a constant 0 MPa tensile stress, giving rise to the contraction of the test specimen and resumption of its permanent shape (step 4) [13].

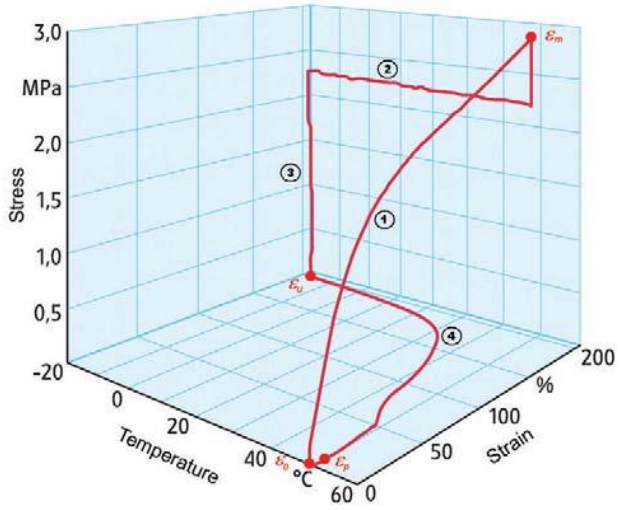


Figure 8 - Typical stress-strain-temperature diagram, for a thermoplastic SMP with a thermally induced shape-memory effect [13].

3.3 Quantification of the shape-memory effect

The several properties of a shape-memory polymer are quantified with cyclic mechanical tests where the polymer is under different external stimuli. However, since the most frequent external conditions are related to heat or light, the test procedures most frequently developed are thermo-mechanical or photo-mechanical tests.

The shape-memory effect is quantified with the percentage of shape fixing (shape fixity ratio R_f) and the extent of shape recovery (shape recovery ratio R_r). The R_f describes the ability of a given polymer to fix the mechanical deformation applied during the programming process, it is equal to the amplitude ratio of the fixed deformation to the total deformation:

$$R_f(N) = \frac{\varepsilon_u(N)}{\varepsilon_m} \tag{3.1}$$

In equation (3.1) the $\varepsilon_u(N)$ is related to the strain after relaxation in the n^{th} cycle and ε_m is the maximum strain, whereas the recovery ratio quantifies how well the permanent shape has been memorized by the material and is defined in a strain-controlled protocol as

$$R_r(N) = \frac{(\varepsilon_m - \varepsilon_p(N))}{(\varepsilon_m - \varepsilon_p(N-1))} \tag{3.2}$$

where ε_p is the strain after recovery. The recovery ratios of SMPs are in the range of 80-90, while the shape fixities depend on the test protocol [14].

3.4 Activating the shape-memory effect

SMPs are known and used in different applications because they can recover large strains when under external stress, increasing temperature, UV-light or compression. The temperature effect can be activated indirectly as well, using a magnetic field, electric current or infrared light, for example. The change of a temporary shape to the original one is influenced by the amount of mechanical deformation affecting the temporary shape, that is saying, the programming of the material. Recently, multi-shape (more than double-shape memory polymers) memory effect has been studied, and there are several examples of materials that have a temporary shape A and change to another temporary shape B and finally to the permanent shape C, which opens a whole new range of different possibilities.

Multi-shape effect can take advantage of different independent transition temperatures or a broad glass transition of the material. This fact can be considered as an infinite number of transitions, leading to the theoretical possibility of infinite number of memorized shapes. Within a range of T_g there is the possibility to, in theory, fix and recover several temporary shapes by changing the temperature in small quantities, which would be an outstanding innovation in the material's industry [14].

The programming of a given material consists in fixing a permanent shape with the netpoints and the switching segments allowing their deformability. Additionally, it involves the quantification and determination of the temperatures and stimulus that will change the material's shape. The netpoints can be of chemical (covalent cross-links) or physical (intermolecular interactions) nature. Stimuli-sensitive switches that form additional cross-links are required to allow reversible fixation. These additional cross-links

are established by reversible chemical bonds, intermolecular interactions, or solidification of switching domains when cooled below their T_{trans}, such as T_g and T_m or liquid crystalline transition temperatures [14].

To summarize, the shape-memory polymers have a material network with netpoints to determine the permanent shape and stimuli-sensitive molecular-switches responsible for the shape-memory effect that changes the part's shape. These polymers are able to assume different sizes or shapes under thermal variations, above and under the T_{trans}, that can be triggered direct or indirectly (for example with irradiation or electrical current); light-induced situation through the incorporation of reversible photoreactive molecular switches or compression and consequent deformation and these properties make SMPs a very important class of polymers in a wide range of possible applications in different social fields.

3.5 Poly(lactic) acid

Poly (lactic) acid or polylactide (PLA) is one of the most extensively studied and used polymer in biodegradable applications. It has a proven potential in the replacement of petrochemical-based polymers for industrial applications or as a leading biomaterial in a broad range of applications. This polymer is well known for its thermoplastic behaviour, high-strength, high-modulus to be used in industrial packaging field as well as in biocompatible/ bioabsorbable applications.

The first synthetization of PLA was made in 1932 by Wallace Carothers and the polymer produced was a low molecular weight (Mw) PLA, after the heating of lactic acid under vacuum while removing the condensed water. At that time, the engineers found it difficult to increase the Mw of the polymers obtained, but, finally, with a ring-opening polymerization (ROP) of the lactide a PLA with higher Mw was produced. Nowadays, there are multiple ways to fabricate PLA, but the process is neither simple nor easy to execute. PLA synthesis requires rigorous control of conditions (temperature, pressure and pH), the use of catalysts and long polymerization times and can be prepared by some polymerization processes from lactic acid including: poly-condensation; ROP and by direct methods such as azeotopic dehydration and enzymatic polymerization, being the ROP and direct polymerization the most commonly used production technics [15].

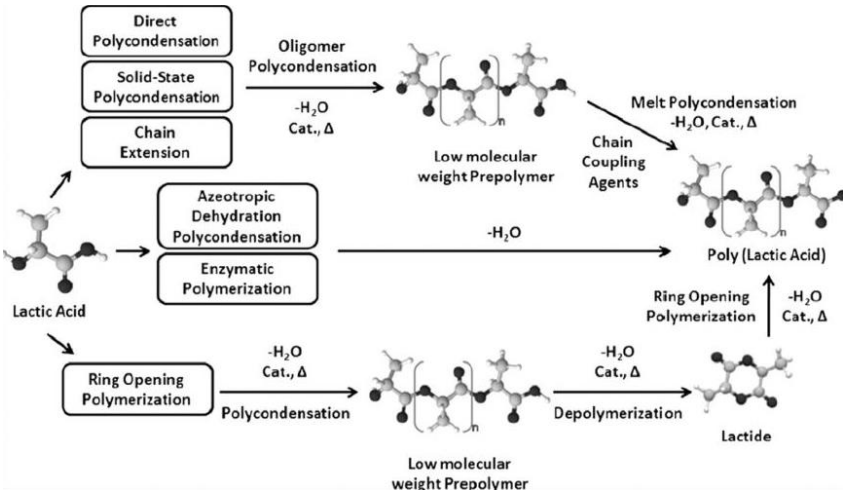


Figure 9 - Synthesis methods for PLA [15].

The PLA synthesis and production have numerous favourable points regarding the eco-friendliness of the final product, as well as the biocompatibility once this material does not produce toxic or carcinogenic effects in contact with human tissues and the degradation products do not interfere with tissue healing. Furthermore, the processability of the material and the spectrum of different manufacturing processes that can be accomplished with PLA makes it a very attractive biopolymer to work with. Additionally, the energy savings in its production is potentially advantageous with respect to cost-savings as well.

The drawbacks of poly(lactic) acid are related with the poor toughness of the material, given the fact that PLA is a very brittle material with less than 10% of elongation at break (which in some cases is also an advantage), and the slow degradation rate. The hydrophobicity and the low cell affinity can, in some cases, lead to an inflammatory process. Another disadvantage of this material hangs on the fact that it is bioinert with no reactive side-chain groups, making its surface and bulk modifications a challenging task [15].

3.5.1 PLA's physical; mechanical and thermal properties

The component's isomers, processing temperature and molecular weight influence the properties of a given material. A very important property of polymers is the rate of crystallinity. Recall that crystallinity is the indication of crystalline region in the polymer with respect to amorphous content and influences hardness, modulus, tensile strength, stiffness, crease and melting points. This property plays a very important role when selecting a polymer for a required application. PLA with the stereoisomer poly(L-lactide) acid (PLLA) content higher than 90% tends to be crystalline, while the lower optically pure is amorphous. The decreasing of PLLA amount in PLA based

polymers decreases the melting temperature and glass-transition temperature.

For amorphous PLA, T_g is one of the most important parameters, because of the changes occurring above this temperature in the polymer network. In fact, for a semi crystalline PLA both transition temperatures are physical parameters that help to predict the material behaviour under specific loads and environments. The T_g determines the upper use temperature for most commercial applications and for semi crystalline PLA both T_g (~58ºC) and T_m (130-230ºC, depending on the structure) are important for determining the use temperatures across various applications. These properties are strongly affected by overall optical composition, primary structure and Mw and the values can be altered considering the production and the composition of the material [15].

Regarding the biodegradation of PLA, the Mw has a significant impact when it comes to degradation, strength and solubility properties. An increment in the molecular weight in PLA will imply a longer degradation rate and a higher molecular weight PLA has a complete resorption time of 2 to 8 years. Therefore, it is mandatory to take this into account when engineering the material for a given application. In the human body, the scission of the main chains of macromolecules and the degradation of the material depends on Mw, crystallinity, purity, temperature, pH and enhancers, additives, etc. The degradation process occurs in two different phases: at first the water penetrates the bulk of the material reducing its molecular weight, hydrolyzation. Afterwards, occurs an enzymatic attack of the fragments and the metabolizing of the fragments results in a rapid loss of polymer mass illustrated in the Figure 10.

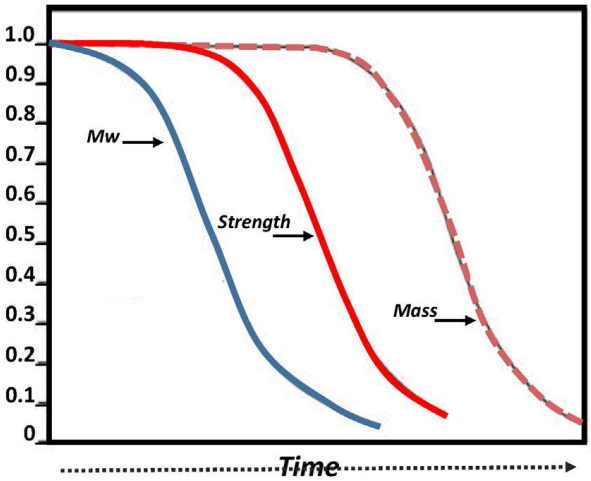


Figure 10 - Generic curves showing the sequence of polymer-molecular weight; strength; and mass-reduction over time [15].

S. Farah et al. stated that semi crystalline PLA is usually preferred over the amorphous when higher mechanical properties are required, because it has a tensile modulus of around 3 GPa, tensile strength of 50-70 MPa, flexural modulus of 5 GPa, flexural strength of 100 MPa and an elongation at break of about 4%. The molecular weight is very important in the mechanical properties and crystallization behaviour. The ability to control the stereochemical architecture allows precise control over the speed and degree of crystallinity, the mechanical properties and processing temperatures of the material [15].

In Table 1 are displayed some mechanical and thermal properties of PLA for general purpose from CES 2018 EDUPACK©. The shape-memory effect of a polymer, as it was stated before, can be activated through a variation in the temperature of the environment where the polymer is in. Because of this, the thermal properties of a given material should be carefully studied before its application. As it can be concluded by looking at the thermal properties, the glass temperature has a range starting at 52ºC until 60ºC. Another key thermal property to the usage of PLA as a memory-shaped polymer is the thermal expansion coefficient (TEC) that is estimated from 126-145 μstrain/ºC. This determines the tendency of mater to change shape, area and volume when subjected to a change in temperature, thus giving a perspective of how PLA will behave under temperature changes.

Table 1 - Properties of Polylactide obtained in CES 2018 Edupack©. (* marked values are estimates).

Mechanical Properties			
Property	**Min**	**Max**	**Unit**
Young's modulus	3.3	3.6	GPa
Specific Strength	2.63	2.87	MN.m/kg
Tensile Strength	47	70	MPa
Elongation	2.5	6	%strain
Flexural Strength	83	108	MPa
Shear modulus	*1.2	1.29	GPa
Poisson's ratio	0.38	0.4	
Hardness – Vickers	17	22	HV
Fatigue Strength (10^7 cycles)	22.2	27.7	MPa
Thermal Properties			
Property	**Min**	**Max**	**Unit**
Melting point	145	175	ºC
Glass temperature	52	60	ºC
Thermal expansion coefficient	*126	145	μstrain/ºC
Maximum service temperature	*45	55	ºC

It is important to notice that, during processing, some changes in PLA structure take place, along with a diminish in the Mw due to chain scission. Furthermore, it was found, that mechanical processing led to quasi disappearance of crystal structure and it could be recovered after a heat treatment of annealing. During the processing of molten PLA, it is also frequent to see a thermal degradation, related both to processing temperature and residence time in the extruder and hot runner. This material is also thermally unstable with a rapid loss of molecular weight when exposed to higher processing temperatures. The thermal degradation starts partially under T_m and there is a higher degradation rate with the increasing of processing temperature.

3.5.2 PLA's biocompatibility

The proximity of materials with human tissue, as well as the time for the *in vivo* application are some of the facts that imply the proper assessment of the safety of materials compatible with human tissues. The biocompatibility of a material is the ability to be compatible with a living tissue or system by not being toxic or injurious and not causing immunological rejection. The classification of a material as biocompatible regards the absence of formation of an intolerable inflammatory reaction that is not proportionate to its advantages. I.e., the material is degraded in the implant site in the body into safe components that will be eliminated from the body, without leaving any consequences to living tissues or systems. The material should also be free of microbial agents and pyrogens or traces of toxic chemicals that were incorporated during preparation/manufacturing or formed during storage or use. The biocompatibility is influenced by several parameters such as the shape, size, surface chemistry and roughness, design morphology and porosity, composition, sterility, duration of contact and degradation [16].

The implementation of a biomaterial leads inevitably to an inflammatory reaction. This reaction occurs in order to avoid tissue damage, insulate and eliminate the foreign material and to start the repairing process. It is called foreign body reaction (FBR), being divided in an acute phase and in a chronic phase. The firstly mentioned phase lasts between hours and days after the implementation and is characterized by the formation of a protein layer on the biomaterial surface. The formation of the layer is accompanied by enhanced expression of adhesion molecules, which leads to extravasation of neutrophils from the bloodstream and their migration to the implant as it is represented in Figure 11 (B). Following the acute phase, neutrophils are replaced by macrophages to coordinate a complex cellular reaction and, afterwards, fuse into foreign body giant cells (Figure 11 (D)) forming a continuous layer encapsulating the biomaterial and thereby protecting the

host from the biomaterial. In the end, this process leads to the formation of a highly fibrous and avascular capsule, thus further isolating the biomaterial in the chronic phase of the process. These cells degrade the biomaterial with time, and their number gradually decreases with the time[16].

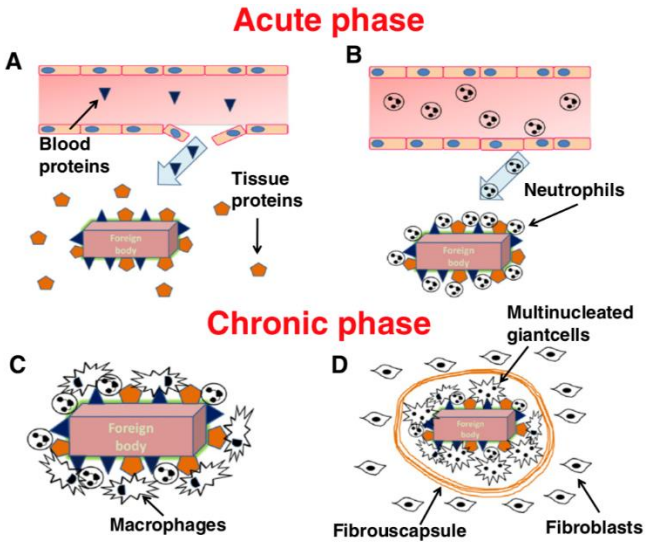


Figure 11 - Schematic representation of acute and chronic phases of FBR [16].

In sum, this particular material has very good biocompatibility properties with high Mw and crystallinity resulting in a lower degradation rate. There are some drawbacks for the usage of PLA in applications where biocompatibility is important because its excessive brittleness and slow crystallization often limit its usage under specific environments and requirements.

3.5.3 PLA-based shape-memory materials for biomedical applications

As previously mentioned, PLA offers some unique features when it comes to biodegradability. Biocompatibility, thermoplastic processability and eco-friendliness, as well as the bioresorbable capability, that can lead to an increase in the use of this material in medical applications due to its unique ability to be completely resorbed in pre-designed time frames ranging from months to a few years. PLA is currently used in a wide spectrum of applications, going from surgical sutures to drug delivery devices, or interference screws for knee, or hand surgeries for non-invasive surgeries. In all these applications PLA is exposed to specific environments and this proves the diversity of characteristics present on this material that can be exploited for a myriad of possible outcomes for medical applications [15].

For biomedical applications, it is important and desirable for a material to have the transition temperature for activation of the shape-memory effect slightly above the body temperature to ensure stable shape fixing in a minimally invasive configuration during surgical delivery and to safely trigger the shape recovery to a preprogramed configuration. The glass transition temperature of PLA around 60ºC is a disadvantage for the *in vivo* direct use because of a potential tissue damage that a high triggering temperature may incur. The *in vivo* degradation profile of PLA-based SMP medical implants should, and usually, is designed to match the intended function being this a key feature for the possible use of the material in a given application [17].

For the shape-memory effect to be accomplished in PLA-based SMPs there are several mechanisms that can be used such as the heat-driven shape recovery; the "plasticizing effect"-triggered shape recovery and an inducing of the shape recovery with chemical structure changes. It is possible to heat the material above T_{trans} and with the rise of the temperature the polymer chain motion is activated either by direct external heat or by heat generated by embedded fillers in response to magnetic, electric and light actuations. Besides heating SMPs above the transition temperature it is possible to trigger the recoiling of the polymer chains decreasing the T_{trans} dynamically by environmental factors, for example reducing the transition temperature with the plasticizing effect of water, leading to the shape recovery. Another option is changing chemical structures of the SMP to decrease T_{trans}.

As shown above there are innumerable possibilities to activate shape-memory effect in PLA-based SMPs and it is also possible to set the mechanical and physical properties of this material to previously designed applications. Thus, it is expected, along this work, to determine some of the specifications of the material to fulfil the requirements of the product in development for orthopaedic surgery of the ACL.

Chapter 4

4. Additive Manufacturing

The speeding up of the technology world makes it mandatory to reduce the time spent during a product development and its 3D modelling allows a faster checking of how the process is evolving. Fused-Deposition Modelling (FDM) is a 3D-printing technology used worldwide and can use polymers, namely thermoplastics, like PLA, to produce 3D-prototypes and final products used in a wide range of industries, offering the possibility to fabricate complex geometries from three-dimensional model data. Biomanufacturing PSIs regards the overcoming of determined constraints that will be detailed along this chapter.

4.1 General considerations on 3D Printing

3D printing is a technique used in the additive manufacturing (AM) field for the fabrication of a full panoply of complex structures and geometries using a three-dimensional computational model constructed in a computer aided design (CAD) software. The process behind the physical models' production consists in the successive printing of superposed layers of material formed on top of each other. The first person to report the development of a process known as stereolithography (SLA) was Charles Hull in 1986 and it was subsequently followed by other processes such as powder bed fusion, fused deposition modelling, inkjet printing and contour crafting (CC), for example.

There have been some new applications with the development of novel materials and AM methods and recently this has reduced the costs of 3D printers, thereby expanding its applications in schools, homes, libraries and laboratories. This has spread these AM techniques throughout the whole world and enhanced the developing of new emerging processes requiring low budget.

In the early days, 3D printing was used extensively by architects and designers to produce aesthetic and functional prototypes due to its rapid and cost-effective prototyping capability, minimising the extra-spending associated to this process, for the development of a product. In recent years, this technique is being used in a wide range of industries from prototypes to products allowing product customization in small-quantities with relatively low cost. This is especially important in the biomedical field, whereby unique patient-specific products are typically required, once it is possible to produce a diverse range of medical implants from CT or MRI tissue replicas [18].

The advantages of 3D printing over some traditional techniques are often are associated to the fabrication of complex geometry with high precision, maximum material savings, flexibility in design and personal customization. There are some different kinds of materials that can be used in additive manufacturing including, for instance, metals, polymers, ceramics and concrete. PLA and acrylonitrile butadiene styrene (ABS) are the mainly used polymers in various applications, and advanced metals and alloys are typically used, for example, in aerospace sector because traditional processes are more time-consuming, difficult and costly. However, the inferior mechanical properties and anisotropic behaviour usually limit the usage of this technique for large scale production, therefore, an optimized pattern of 3D printing priming is important to control flaw sensitivity and anisotropy.

Another important aspect regarding this technique is the mass customisation (the production of a series of personalized goods such that each product can be different while maintaining a low price due to mass production). 3D printing is devoid of the added cost due to mould making and tooling for a customized product. Because of this, mass production of a number of identical parts can be as cost-effective as the same number of different personalized goods, being the change between different designs quite straightforward with negligible added cost and need for special preparation [18].

However, improvements are required, particularly in the fabrication speed and cost reduction, to enhance the efficiency of the 3D printing industry. Also, high costs and time-consumption remain to be major hurdles that inhibit mass production [18].

All stated above shows the importance of a growing field in the engineering world that result in waste reduction of expensive materials and eliminates the assembly process, reducing risks of localized stresses and substantially increasing the freedom of design. Due to all this factors, this is an expanding technology in the manufacturing processes world. Namely in the biomedical applications field.

4.1.1 Polymers for 3D printing

Polymers are the most used class of materials in the 3D printing sector, due to their diversity and ease of adaption to different processes and can be found in the form of thermoplastic filaments, reactive monomers, resin or powder. This type of materials has been used in aerospace, architectural, toy fabrication and medical fields and there are some benefits regarding its usage in 3D printing including the ability to customise geometry with high accuracy.

Furthermore, polymers' processing can be more cost-effective than other traditional formative methods, such as moulding or extrusion for customized products, as aforementioned. On the other hand, pure polymer products built by 3D printing techniques are only often used for conceptual prototypes due to the lack of mechanical properties.

Thermoplastic materials, such as ABS and PLA, can be processed by various 3D printing methods and, particularly for PLA, maintaining optimum resin viscosity at low temperature is a key challenge for its usage. This problem can be overcome increasing printing temperature or with the use of a correct plasticizer [18]. Other drawbacks related to 3D printing techniques are the void formation between subsequent layers creating sometimes additional porosity and reducing mechanical properties; anisotropic microstructure and mechanical properties, because of the nature of layer-by-layer printing (the microstructure of the material inside the layer is different to that of the boundaries between layers, resulting in different mechanical behaviour of the 3D printed part under vertical tension and compression compared to that in the horizontal direction) and divergent aspects from design to execution because of limitations in AM that can produce a few defects that were not expected in the designed element. Some imperfections commonly present in 3D printed parts will be detailed in subsequent sections.

Various 3D printing techniques are available for fabricating polymers namely stereolithography, selective laser sintering, FDM, 3D bioprinting and inkjet printing, but FDM is the most commonly used for the fabrication of polymer composites and thermoplastics with low melting points. However, eco-friendly polymeric materials with the correct physical properties are a major concern for FDM, because, usually, common commercial polymers for 3D printing, such as ABS and PLA, do not meet the desirable outputs. While ABS has good mechanical properties and PLA satisfactory eco-friendliness, these two materials have some drawbacks regarding the unpleasant odour and poor mechanical properties, respectively [18].

The most common types of polymers used for 3D printing are thermoplastic polymers such as ABS, PLA, polyamide (PA) and polycarbonate (PC) and thermosetting powders such as polystyrene, polyamides and photopolymer resins are mostly used for rapid prototyping. However, there

has been an introduction of a reinforcement of polymers with fibres and nano-materials with the aim of enhancing the mechanical properties of the printed products to be used as load-bearing or functional components.

The usage of polymers for 3D printing when mechanical properties are not a concern, and there is a requirement for complex geometries, is recommended. In addition, when it is needed a pivoting and trial-error method for rapid prototyping, polymers fulfil all the requirements because they are cheaper and reduce waste when compared with metals and alloys, or other manufacturing processes.

4.2 Fused Deposition Modelling description

Fused Deposition Processing, whether it is Fused Deposition Modelling, Fused Deposition of Ceramics (FDC) or metals (FDMet), is a Solid Freeform Fabrication (SFF) technique and builds a 3D object layer-by-layer from a previous CAD design where spooled filaments of 1.75mm of nominal diameter are fed into a liquefier head via computer driven rollers. The liquefier head is machine controlled for movement in the horizontal *xOy* plane and the three-axis movement is completed with a fixtureless building platform that moves in the *Oz* direction [19].

FDM machines consist in the guidance of a continuously wound of spool of wax or polymer to a liquefier head throughout a winding path before being fed into a pair of counter rotating rollers, showed in Figure 12. With the heating, the filament softens and melts inside the liquefier to a temperature just above its melting point and the molten polymer/wax is extruded out of a nozzle (with a diameter between 0.25 and 1.27mm) at the end of the liquefier. The force required for the extrusion is of a small magnitude and is performed by the rollers driving the incoming filament [19].

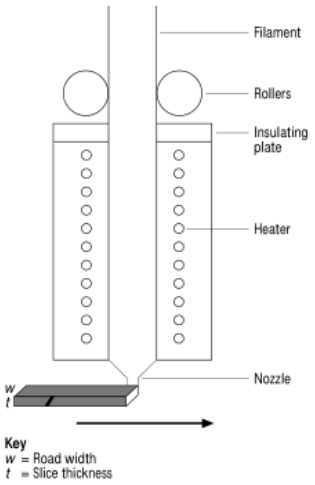


Figure 12 - Conceptual schematic of material feeding in commercial FDM [19].

4.2.1 FDM parameters

This kind of technologies rely on the specification of different parameters, as indicated in Figure 14, that usually include nozzle's temperature, the printing speed, the layer height and the speed of the cooling fan, being the typical printing speeds around 60mm/s. The temperature of extrusion depends on the material's thermal properties and usually, some extruders can reach easily temperatures around 200ºC. This temperature is a key parameter that can harm the end product surface quality because it affects the bond between the filaments which form the piece that is being printed.

For the sake of a better understanding of the parameters that will be used in the 3D printing of the device, some of them should be briefly defined and detailed, regarding, especially, on the layer height; width; print angle; construction orientation; infill and shell thickness.

The layer height has direct influence on the part's surface finishing and it needs to be taken on account once it is affected by the filament's thickness, extruder nozzle diameter and printing speed. As it can be intuitive to understand, a lower layer height will be traduced in a better-finished part and a closer approximation to the virtual model. Most FDM printers have a minimum layer height of 20µm to 300µm. The resolution of the printers is often qualified with this parameter.

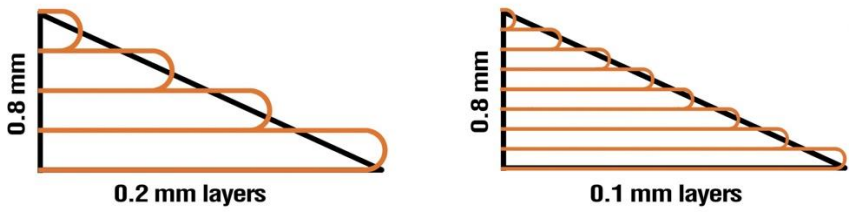


Figure 13 - Illustration of the difference between two distinct layer heights. [20]

Apart from the layer height another important parameter that defines the quality of the finished part is the layer's width, which value is a multiple of the width of the extruder nozzle. Besides both this dimensions, other quantification that needs to be programmed before 3D printing regards the print angle that sets the path that the extruder will make along the print base.

The infill regards the amount of material that will be deposited inside the piece, quantified by its percentage. This parameter is directly related to the desired stiffness for the part and will have influence on the quantity of material that will be used on the 3D printing process. It will also influence the mechanical properties, given the fact that different filling patterns will produce different structural properties on the piece that is being designed.

According to Agarwala et al. the parameters that take place in FDM processes can be divided into four different categories, listed in Figure 14, being these the operation specific, machine specific, materials specific and geometry specific parameters. The optimization of materials specific parameters is required for the development of a new material system for fused deposition (FD) processing and once such a material system has been developed, proper optimization of other process variables should determine the internal and external quality of FD processed parts. The interdependency of these variables makes it difficult to optimize all of them in a straightforward way, but concurrent optimization is required for the sake of fabrication of high quality FDM processed parts [19].

Operation specific	Machine specific	Materials specific	Geometry specific
Slice thickness	Nozzle diameter	Powder characteristics	Fill vector length
Road width	Filament feed rate	Binder characteristics	Support structure
Head speed	Roller speed	Viscosity	
Extrusion temperature	Flow rate	Stiffness (column strength)	
Envelope temperature	Filament diameter	Flexibility	
Fill pattern		Thermal conductivity	

Figure 14 - FDM process parameters [19].

The process' non-optimization for FD leads to serious strength (or other properties) limitations in parts processed by these techniques and even with a complete optimization there are some defects existent in products manufactured with FD processes. Eliminating these inherent imperfections requires the development of new processing strategies in existent FDM systems.

4.2.2 FDM processed parts' defects

An important point regarding FDM are the possible defects that invariably are observed in processed parts, even when a suitable material formulation is developed, and all processing variables are being taken into account. Most of the surface defects showed are related to the state of the art in AM technologies in general, whereas the internal defects are mostly due to limitations in the FDM technologies. As in other engineering applications, the surface defects can be eliminated with surface treatment processes after parts' fabrication, but internal defects usually result in strength limitation, which cannot be eliminated after the processing of the desired part.

The surface defects present on FDM processed parts can be of several natures and are usually related to the inability of FDM systems to produce the most approximate part to the geometries previously designed in a CAD system. The staircase, or registering effect is one of the more easily traceable

defects displayed on fused deposition processed parts and is due to the layer-by-layer production technique. The CAD model is reduced from a 3D volume representation to 2D (two-dimensional) "slices" in which each "slice" is laid down on top of the previous producing the final volume. This layered manufacturing process results in a predictable surface roughness of the outer and inner surface in the build direction as shown in Figure 15. These defects require an increment in time to fabricate the finished part and can be reduced with the aid of smaller layers' thickness, producing better surface finish. At the same time, with smaller thickness, there will be more layers to deposit and the task will be more time-consuming , therefore, the most common practice to obtain the desired surface finish in SFF processed parts is to surface finish the part after its fabrication [19].

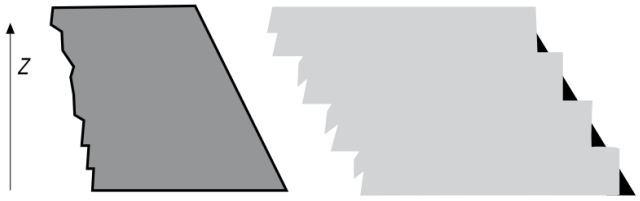


Figure 15 - Schematic showing the formation of the staircase effect on the build direction surface in SFF processed parts (right) when the CAD surface is planar (left) [19].

In the figure below is presented another surface defect that usually occurs in FDM systems, the chordal or curve-approximation errors. The linearization of the curves performed in CAD designs with gross linear approximations is a necessity due to the current requirements of hardware control. Thus, because of this, in FDM systems, the liquefier head is limited to moving in piecewise linear segments and therefore the curved surfaces are produced as shown on the right side of Figure 16 [19].

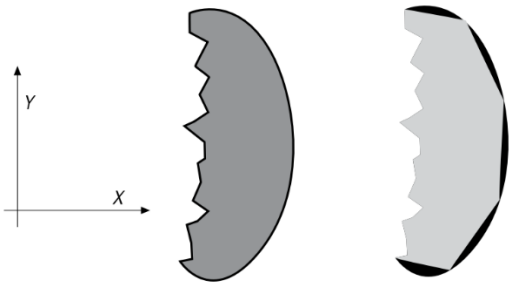


Figure 16 - Schematic showing the formation of the chordal effect on xOy plane in SFF processed parts (right) as a result of linear approximation of the actual curved surfaces (left).

Other key surface defects occur in the top and bottom surfaces of the processed part, because of the contact of the bottom face with the fixtureless table that has a certain degree of roughness, creating a negative image of its

roughness on the under surface of the part as the first layer is deposited. Relating to the top surface, the last layer deposition has a ridged surface due to the rounded top surface of the roads, which may require surface smoothing operation after the 3D printing. Other surface defects usually are related to lack in the "start/stop" optimization and the removal of the support structure bars, which are required sometimes for the production of more complex geometries [19].

When good mechanical properties are required, the inner defects play an important role and these can be related to FDM system hardware and software limitations, poor optimization of the materials characteristics, and poor process optimization. These can be in the form of sub-perimeter voids, voids that are left due to incomplete filling at points where the raster segment turns around at the perimeter; defects between adjacent roads occurring either if there is or there is not physical contact between them or core voids that happen if an incorrect road width is selected for each contour loop, resulting in a void in the centre of the layer.

Because of all these defects that can take place in this kind of produced parts, the planning of a process of this nature should consider several parameters used in AM processes, namely in 3D printing and in FDM. There are several different properties influencing the final quality of the products manufactured, so this regards a comprehensive study of all the different parameters in order to obtain the desired results when a 3D printing part is under production.

Thereafter, extra challenges and characteristics regarding the biomanufacturing and patient-specific instrumentation processing will be stated to show the importance of the development that should take place on the biomedical manufacturing field, as well as in patient customization of healthcare devices.

4.3 Biomanufacturing

The production of medical applications and devices must take into account the active interaction of the proper devices with human tissues and systems, and owing to this fact, there are some requirements for the design of medical devices that are significantly different for this kind of products, e.g. reliability, corrosion resistance, biocompatibility, customization, doctor-intuitive interface, biodegradation and controllability. To achieve all these attributes and characteristics spending the least amount of money possible, advanced manufacturing technologies are needed to produce patient-specific instruments and products at a suitable price for worldwide distribution.

The quality-of-life and the reduction of healthcare global costs are closely related to the development of medical devices and systems. These two factors led to an increment of the global market volume for medical equipment in recent years. As an example, the global market value of knee and hip prostheses reached EUR 9.0 billion in 2011 with 58% of the market located in the USA, 23% in Europe and 19% in Asia-Pacific [21].

The International Academy for Production Engineering created a collaborated group to address the integration of current manufacturing technologies and the development of new methods. Biomanufacturing is the application of design manufacturing technologies to reduce the cost while advancing the safety, quality, efficiency and speed of healthcare service and biomedical science. As shown Figure 17, requires expertise in basic manufacturing processes integrated with machine design, surface modification, precision engineering and metrology under the overarching frameworks of design, life-cycle engineering and speed of healthcare service and biomedical service [21].

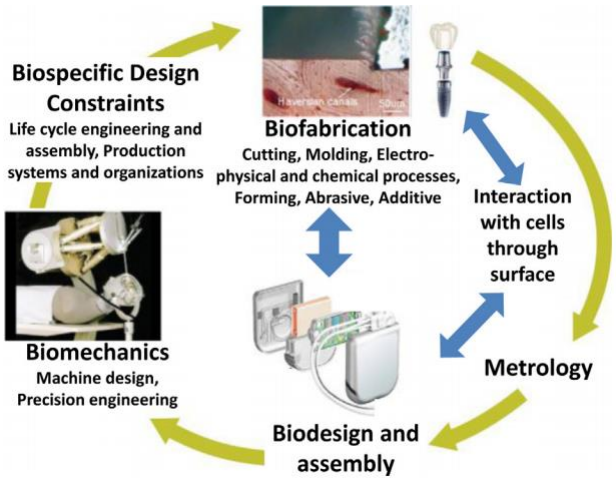


Figure 17 - Overview of biomanufacturing [21].

The biomanufacturing involves the interaction and relation of the materials present in biological tissues (such as bones, muscles, etc) and biomaterials. During the processing of living tissue, the equipment used in the medical environment and all the materials that will be in contact with the body have to overcome several specific constraints that are present in the biomedical applications.

The design strategy of biomedical devices is getting more complex during the years because of the development of manufacturing technologies and the appearance of new biomaterials. These challenges can trigger the ingenuity and creativity of the engineers and medical doctors that are currently trying to develop new ways to enhance the quality of the applications and consequently the quality-of-life of the patients. The design

control process needs to validate the design with a wide range of tests regarding biocompatibility, biomechanics, electrical safety, etc.

The life-quality expectations are rising, and the demographic trends will increase the demand for medical systems, and, from a health economics point of view, the successful diffusion of new products is always dependent on the interdependences of international healthcare markets with the patients, healthcare providers, health insurance funds and the healthcare industry as market players. M. Mitsuishi et al. plotted the cost difference of a new mechanical application compared to an established one against the effectiveness difference of the two methods as it is shown in Figure 18. Any new treatment in the upper left quadrant is inappropriate, being the opposite true for the lower right section: such innovations should be introduced in the market. Most new developments belong to the upper right section. In this case, the decision of whether the cost difference is acceptable to gain a defined amount of effectiveness is very complex. The discussion is at least as complex in the lower left section, where the limited financial resources limit the amount of cost reduction and what is the balance that could justify a certain reduction in effectiveness [21].

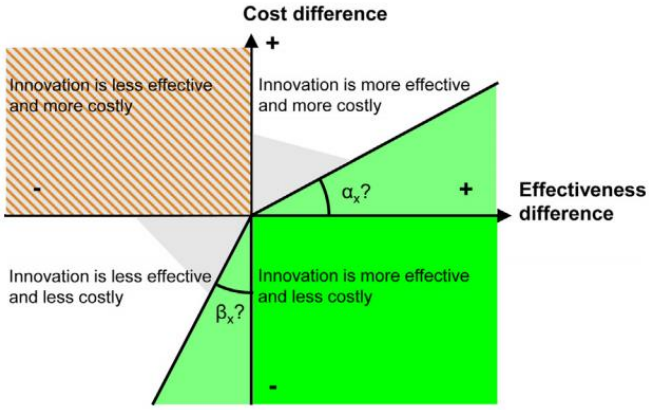


Figure 18 - Cost-effectiveness chart for healthcare innovations [21].

An important challenge of medical engineering is the interaction between the engineer and the healthcare provider since the engineer cannot have the required knowledge of the medical fields and, because of this, the definition of the patient needs, as well as the ease of usage of these specific products always requires the involvement of a medical doctor.

Another key point about the biomanufacturing of medical applications is the personalization. Clinical evidence has demonstrated that personalized medicine and devices are better in terms of treatment as well as efficiency for many procedures. Because of the lack of cost effectiveness, mass production of personalized components in current medical applications is inefficient and sub-optimized. For example, in an operation room, devices of various sizes

need to be ready, but only a few will be used during the procedure. This is the so-called "just-in-case" system in healthcare which is costly to the society [21]. It is needed some research to develop new cost-effective procedures and devices to increase the efficiency of hospital resources and this work will show some innovation process in one of the most frequent orthopaedic procedures.

Some other aspects are making the mission of biomanufacturing more difficult regarding the chemical, thermal and radiation processes and the sterilisation of the device before usage. Biocompatibility (the ability of a material to perform with an appropriate response in a specific application) is another requirement that usually challenges the production of a device, because it limits the range of possible materials that could suit the needs for a designated function of a product and will be further scrutinized in this document.

Medical interventions are conventionally performed based on the ability and judgement of the individual surgeon, whereas advanced diagnostic equipment, CT and MRI for instance, is fully automated. Because it is not an automated process, the accuracy of the medical intervention depends to a large extent on the surgeon's skills. The combination of surgeons' experience with the precision and rich data that a mechanical system can offer enhances the overall clinical performance. What biomanufacturing strives to offer is an increasing precision of the medical interventions to push up the life-quality expectancy of world population, using PSI and Data analysis software, for example.

4.4 Patient-Specific Instrumentation

The work that will be detailed throughout this thesis is the production of a PSI that guides and assists the arthroscopic ACL reconstruction. In other words, a device that is produced using AM, fully customized to the patient, and should enhance the precision of a designated function that a standardized product, or technique, was performing weakly.

After the collection of the geometrical and structural data obtained preoperatively by CT or MRI it is possible to produce a 3D model of a device and, after the conclusion of this modelling process, using AM, the customized product can be used in a wide range of medical applications. These items could be produced from plastics and biomaterials and should either be removed after the application or biodegrade with time inside the human body.

The advantages of PSI remain controversial and are related to the reduction in time and better accuracy of the application, whereas the disadvantages are associated to the higher direct cost (that can be overcome

with the higher efficiency of the hospital resources) and an increment in the exposure to radiation to collect data for the 3D model.

D.R Lionberg et al. made a study regarding the cost-effectiveness of PSI for a total knee arthroplasty (TKA) and found that the total time inside the operating room had decreased when comparing to Computer Assisted Surgery (CAS). In addition, it was concluded that the accuracy of PSI was inferior to CAS, but better than the performance of the surgery without the customized instrumentation. It is important to notice that the cost of a robot to perform this kind of surgery is very high. Furthermore, they lack results, and the cost savings of PSI (despite the higher direct purchase price, comparing with their non-use or buying expensive surgery-robots), were achieved as a result of an improvement in operative room efficiency and reduction in total operative time. So, PSI may be applied in institutions where work output is rewarded with increased income, that is to say, where there are many clinical cases to operate in a short-period of time [22].

The possibility of PSI allowing non-expert surgeons to achieve the same saw cut accuracy as expert surgeons was studied by Gareth G. Jones et al. for the unicomportamental knee arthroplasty (UKA) and they concluded that overall (as expected), using conventional instrumentation expert surgeons were significantly more accurate than trainee surgeons performing the designated function. However, PSI immediately allowed the same trainee surgeons, who had not previously performed the technique, to achieve the same level of overall accuracy as the expert surgeons in some procedures, and even more in others. The conclusions of this study were that assistive technology (in the form of PSI in this case), way cheaper than robotics, allows inexperienced surgeons to achieve the same level of accuracy as expert surgeons [23].

Both of these papers were not related to the arthroscopic ACL reconstruction and, particularly for this surgical procedure there were no findings of PSI's usage. Thus, this is one of the reasons why this thesis is going to be based on this medical application. It is expected that the development of a PSI to help all orthopaedic surgeons achieve more precision in the femoral tunnel placement for the ACL graft will help in the future surgical outcome worldwide.

Chapter 5

5. Finite Element Method

The finite element method (FEM) is a procedure for the numerical solution of the equations in differential or integral form that govern the problems found in nature. For this reason, it is seen as a numerical technique to solve partial differential or integral equations obtaining the evolution in space and/or time of one or more variables representing the behaviour of a physical system. FEM can also be used to solve many field problems, such as torsional deformation of bars, irrotational flow or steady state heat transfer problems. These last will be fully detailed during this chapter for 3D problems.

5.1 Solid mechanics fundamentals

In order to better understand the subsequent chapters, this chapter focuses on the description of the solid mechanics fundamentals, for three-dimensional solids, behind the numerical applications presented in this work. After the fundamentals are explained and clarified, a brief summary of the standard FEM procedure will be exposed.

Thereafter, to allow a better comprehension of the experiments, simulations and practical procedures performed throughout this work, the FEM for heat transfer problems will be also detailed in this chapter.

5.1.1 Stress and Strain

Let us consider a continuous three-dimensional elastic solid with a volume V and a surface S, like the one showed in Figure 19. The surface of the solid can be split into two kinds: the surface where the external forces are prescribed (S_f) and the surface on which the displacements are prescribed (S_d). The forces

applied to the solid can be body forces (f_b) and surface forces (f_s) in any distributed fashion in the volume of the solid.

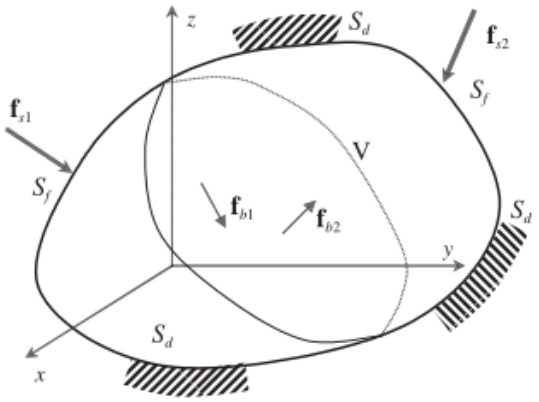


Figure 19 - Solid subjected to forces applied within the solid (body force) and on the solid's surface (surface force) [24].

Figure 20 shows the stress components of any point in the solid, indicated on the surface of an "infinitely" small cubic volume and, on each surface, there will be the normal stress component, and two components of shear stress. Therefore, there are six components in a single point in three-dimensional solids [24].

The stress tensor is often written in the vector form as follows:

$$\boldsymbol{\sigma}^T = \{\sigma_{xx}\ \sigma_{yy}\ \sigma_{zz}\ \tau_{yz}\ \tau_{xz}\ \tau_{xy}\} \tag{5.1}$$

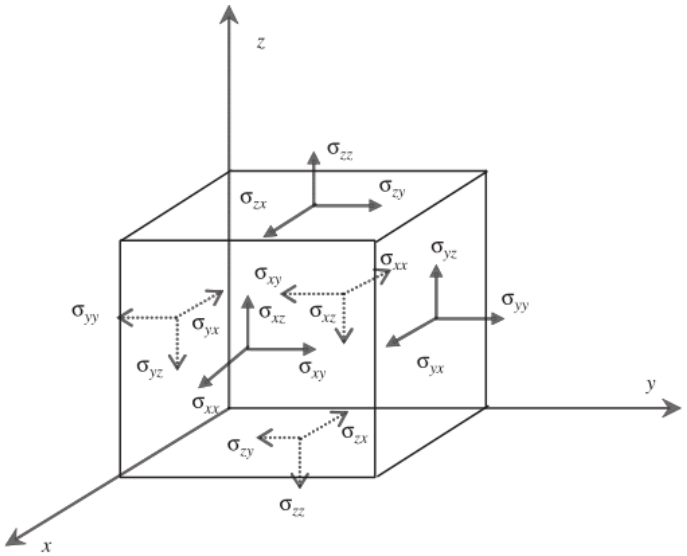


Figure 20 - Six independent stress components at a point in a solid viewed on the surfaces of an infinitely small cubic block [24].

Corresponding to the six stresses tensor, six strain components are present at any point within a solid and it is also possible to write them in a similar vector form:

$$\boldsymbol{\varepsilon}^T = \{\varepsilon_{xx}\ \varepsilon_{yy}\ \varepsilon_{zz}\ \gamma_{yz}\ \gamma_{xz}\ \gamma_{xy}\} \tag{5.2}$$

With the displacement vector composed by three different components, being them the displacement in *x*, *y* and *z* axis and defined as:

$$\boldsymbol{u} = \begin{Bmatrix} u(x,y,z) \\ v\ (x,y,z) \\ w\ (x,y,z) \end{Bmatrix} \tag{5.3}$$

strains, the changes of displacement per unit length, can be obtained from the derivatives of the displacements in the following way:

$$\begin{gathered} \varepsilon_{xx} = \frac{\partial u}{\partial x}\ ;\ \varepsilon_{yy} = \frac{\partial v}{\partial y}; \varepsilon_{zz} = \frac{\partial w}{\partial z} \\ \gamma_{xy} = \frac{\partial u}{\partial y} + \frac{\partial v}{\partial x}; \gamma_{xz} = \frac{\partial u}{\partial z} + \frac{\partial w}{\partial x}; \gamma_{yz} = \frac{\partial v}{\partial z} + \frac{\partial w}{\partial y} \end{gathered} \tag{5.4}$$

With the aid of a matrix of partial differential operators $\boldsymbol{L}$, obtained by inspection of equation (5.4)

$$\boldsymbol{L} = \begin{bmatrix} \frac{\partial}{\partial x} & 0 & 0 \\ 0 & \frac{\partial}{\partial y} & 0 \\ 0 & 0 & \frac{\partial}{\partial z} \\ 0 & \frac{\partial}{\partial z} & \frac{\partial}{\partial y} \\ \frac{\partial}{\partial z} & 0 & \frac{\partial}{\partial x} \\ \frac{\partial}{\partial y} & \frac{\partial}{\partial x} & 0 \end{bmatrix} \tag{5.5}$$

the six strain-displacement relationships of (5.4) can be rewritten in the matrix form:

$$\boldsymbol{\varepsilon} = \boldsymbol{L}\boldsymbol{u} \tag{5.6}$$

5.1.2 Constitutive equations

The relationship between stresses and strain in the material of a solid is given by the constitutive equation, often termed as Hooke's law. The generalized Hooke's law for general anisotropic materials, in the matrix form, is given for the next equation:

$$\boldsymbol{\sigma} = \boldsymbol{c\varepsilon} \tag{5.7}$$

where **c** matrix is the constitutive matrix composed of material constants, which are normally obtained through experiments [24]. For isotropic materials, $\boldsymbol{c}$ can be reduced to

$$\boldsymbol{c} = \begin{bmatrix} c_{11} & c_{12} & c_{12} & 0 & 0 & 0 \\ c_{12} & c_{11} & c_{12} & 0 & 0 & 0 \\ c_{12} & c_{12} & c_{11} & 0 & 0 & 0 \\ 0 & 0 & 0 & (c_{11}-c_{12})/2 & 0 & 0 \\ 0 & 0 & 0 & 0 & (c_{11}-c_{12})/2 & 0 \\ 0 & 0 & 0 & 0 & 0 & (c_{11}-c_{12})/2 \end{bmatrix} \tag{5.8}$$

where the constants c_{11} and c_{12} are calculated in the following manner

$$c_{11} = \frac{E(1-\nu)}{(1-2\nu)(1+\nu)};\ c_{12} = \frac{E\nu}{(1-2\nu)(1+\nu)} \tag{5.9}$$

in which E and ν are the Young's modulus and the Poisson's ratio, respectively. The shear modulus G of the material is given by,

$$G = \frac{E}{2(1+\nu)} \quad \text{or} \quad G = \frac{c_{11}-c_{12}}{2} \tag{5.10}$$

As it is easy to conclude, for an isotropic material, if there is information about the Young's modulus and the Poisson's ratio, G can be calculated using equation (5.10) [24].

5.1.3 Static equilibrium equations

The determination of the static equilibrium equations is performed considering an infinitely small element, requiring equilibrium of forces in all directions. For this infinitesimal solid the dynamic equilibrium equations are

$$\begin{cases} \frac{\partial \sigma_{xx}}{\partial x} + \frac{\partial \tau_{xy}}{\partial y} + \frac{\partial \tau_{xz}}{\partial z} + F_x = 0 \\ \frac{\partial \tau_{yy}}{\partial x} + \frac{\partial \sigma_{yy}}{\partial y} + \frac{\partial \tau_{xz}}{\partial z} + F_y = 0 \\ \frac{\partial \tau_{xz}}{\partial x} + \frac{\partial \tau_{xz}}{\partial y} + \frac{\partial \sigma_{zz}}{\partial z} + F_z = 0 \end{cases} \tag{5.11}$$

and in a concise matrix they can be given by

$$\boldsymbol{L}^T \boldsymbol{\sigma} + \boldsymbol{f_b} = 0 \tag{5.12}$$

where $\boldsymbol{f_b}$ is the vector of external body forces in x, y and z directions:

$$\boldsymbol{f_b} = \begin{Bmatrix} f_x \\ f_y \\ f_z \end{Bmatrix} \tag{5.13}$$

Regarding displacements, the equation (5.12) can be rewritten using equations (5.6) and (5.7):

$$\boldsymbol{L}^T \boldsymbol{c} \boldsymbol{L} \boldsymbol{u} + \boldsymbol{f_b} = 0 \tag{5.14}$$

5.2 FEM fundamentals

When Finite Element Method is used to solve mechanical problems governed by partial differential equations, the problem domain is first discretized into small elements. In each of these elements is assumed a profile of displacements in simple forms to obtain element equations that are assembled together with adjoining elements to form the finite element equation for the whole problem domain.

Once these equations are created for the global problem domain, they can be solved easily for the entire displacement field. This procedure seems simple, but for complex geometries or field variables the determination of discretized system equations is a difficult task and a principle has to be followed in order to solve them routinely for the final displacement field [24].

5.2.1 Strong and weak forms

The partial differential system equations are string forms of the governing system of equations for solids. This strong form requires strong continuity on the dependent field variables (the displacements u, v and w, for 3D solids)

and obtaining the exact solution for a strong form of the system equation is, usually, a very difficult task for practical engineering problems.

With the objective of creating a weak form there are two different methods widely used: energy principles, particularly suited for problems of mechanics of solids and structures and the weight residual method that is a more general mathematical tool applicable for solving all kinds of partial differential equations, for example heat transfer problems.

The weak form is an integral form and requires a weaker continuity of the field variables. Due to the weaker requirement on the field variables, and the integral operation, a formulation based on a weak form often produces more accurate results with a set of discretized system equations, especially for more complex geometries. The FEM is a typical example of successfully using weak form formulations, leading to a set of well-behaved algebraic equations if the problem domain is discretized properly [24].

5.2.2 FEM procedure

The FEM procedure can be summarized with a domain discretization, the division of a body into a given number of elements, being this procedure called meshing and usually performed with the aid of pre-processors that generate unique numbers for all elements and nodes for the solid structure. An element is formed connecting its nodes in a pre-defined consistent way to create the connectivity of the element, forming the entire domain of the problem without any gap or overlapping. After the domain is completely discretized there is a displacement interpolation using shape functions, or interpolation functions, for the nodes in the element, which are predefined to assume the shapes of the displacement variations across the coordinate system.

Once the shape functions are constructed, the FE equation for an element can be formulated with the local stiffness and mass matrix and local element force vector. Given the FE element equation, there should take place a coordinate transformation to relate the local coordinate system to the global coordinate system, defined on the whole structure, to make it possible to assemble all the element equations to form the global system equation. After the coordinate transformation is performed, the global FE system equation can be obtained with the global stiffness and mass matrices, the vector of all the displacements at all the nodes in the entire problem domain and the vector of all the equivalent nodal force vectors.

Once the FE system equation is obtained the imposition of displacement constraints match the conditions imposed to the structure, such as displacement constraints (supports).

The final step is the solving of the global FE equation obtaining the displacements at all nodes of the domain. With this data it is then possible to

retrieve the strain and stress in any element and therefore analyse the structure under the conditions imposed during the procedure.

5.3 FEM for heat transfer problems

5.3.1 Field problems

The following will detail the use of FEM to solve the steady state heat transfer that can be termed as one of the many field problems. The approach to derive FE equations in heat transfer conditions is a general approach to solve partial equations using the FEM, which can be applicable to other field applications governed by a similar type of partial differential equation.

The system equations for 3D linear steady state field problems can be given by the general form of the Helmhotz equation:

$$D_x \frac{\partial^2 \emptyset}{\partial x^2} + D_y \frac{\partial^2 \emptyset}{\partial y^2} + D_z \frac{\partial^2 \emptyset}{\partial z^2} - g\emptyset + Q = 0 \tag{5.15}$$

where $\emptyset$ is the field variable, and D_x, D_y, D_z, g and Q are constants whose physical meaning is different for distinct problems (and materials) and depend on the external conditions that are subjected to the domain. In heat transfer problems, $\emptyset$ is the temperature, D_x, D_y, D_z are the thermal conductivity coefficients, g is the convection coefficient and Q is the heat supply.

5.3.2 Weight residual approach for FEM

When the governing equation for the problem is known it is convenient to use the weighted residual approach to formulate the FEM system equations and the equation (5.15) can be rewritten as

$$f(\emptyset(x, y, z)) = 0 \tag{5.16}$$

where f is given as

$$f\big(\emptyset(x, y, z)\big) = D_x \frac{\partial^2 \emptyset}{\partial x^2} + D_y \frac{\partial^2 \emptyset}{\partial y^2} + D_z \frac{\partial^2 \emptyset}{\partial z^2} - g\emptyset + Q \tag{5.17}$$

It is generally difficult to obtain an exact solution of $\emptyset(x, y, z)$ which satisfies (5.16). Therefore, an approximate solution of $\emptyset(x, y, z)$ is sought for, which satisfies (5.16) in a weighted integral sense, such as

$$\int W\, f\big(\emptyset(x, y, z)\big)\, dx\, dy\, dz = 0 \tag{5.18}$$

in which W is the weight function. It is expected that the solution for $\emptyset(x, y, z)$ is a sufficiently good approximation of the exact results. This is the basic idea behind the weighted residual approach, that can be used in the FEM to establish the discretized system equations.

To ensure a good approximation, the problem domain is divided into elements, as described before, and for each element, it is assumed that

$$\emptyset^h(x, y, z) = \boldsymbol{N}(x, y, z)\, \boldsymbol{\varphi}^{(e)} \tag{5.19}$$

where the superscript h indicates that the field variable is approximated, and the shape functions matrix is

$$\boldsymbol{N} = [N_1 \quad N_2 \quad N_3 \ldots N_{nd}] \tag{5.20}$$

and nd subscript is the number of the nodes present in each element and N_i, with $i = (1, 2, 3, \ldots nd)$, are the shape functions values. In equation (5.19) $\boldsymbol{\varphi}^{(e)}$ is the field variable at the nodes [24].

The Galerkin method uses shape functions as the weight function and the residual calculated at all nodes within the volume (V_e) of an element is then evaluated by the equation

$$\boldsymbol{R}^{(e)} = \int_{V_e} \boldsymbol{N}^T\, f\big(\emptyset(x, y, z)\big)\, dV \tag{5.21}$$

Afterwards, the total residual of each node is assembled and enforced to zero to establish the system equation for the whole system [24].

5.3.3 Three-dimensional heat transfer problem

For three-dimensional problems a given volume can be divided into different 3D elements and, for one element, the residual can be obtained by the Galerkin method as follows

$$\boldsymbol{R}^{(e)} = -\int_{V_e} \boldsymbol{N}^T \left(D_x \frac{\partial^2 \emptyset^h}{\partial x^2} + D_y \frac{\partial^2 \emptyset^h}{\partial y^2} + D_z \frac{\partial^2 \emptyset^h}{\partial z^2} - g\emptyset^h + Q \right) dV \tag{5.22}$$

where the minus sign is added mainly for convenience. This integration must be evaluated to obtain the element matrices.

Throughout a mathematical manipulation, using first the product rule for differentiation and then Gauss's divergence theorem, the residual is now given, in matrix form, by the following expression

$$\boldsymbol{R}^{(e)} = \boldsymbol{b}^{(e)} + \left[\boldsymbol{k}_D^{(e)} + \boldsymbol{k}_g^{(e)} \right] \boldsymbol{\varphi}^{(e)} - \boldsymbol{f}_Q^{(e)} \tag{5.23}$$

where $\boldsymbol{b}^{(e)}$ is related to the gradient of temperature (or heat flux) across the surface (Γ_e) of the element given by

$$\boldsymbol{b}^{(e)} = -\int_{\Gamma_e} \boldsymbol{N}^T \begin{bmatrix} D_x \frac{\partial \emptyset^h}{\partial x} & D_y \frac{\partial \emptyset^h}{\partial y} & D_z \frac{\partial \emptyset^h}{\partial z} \end{bmatrix} \boldsymbol{n}\, d\Gamma \tag{5.24}$$

being $\boldsymbol{n}$ a unitary vector, normal to the surface given by

$$\boldsymbol{n} = \begin{Bmatrix} n_x \\ n_y \\ n_z \end{Bmatrix} \tag{5.25}$$

and $\boldsymbol{k}_D^{(e)}$ and $\boldsymbol{k}_g^{(e)}$ are, respectively, the matrixes related to the thermal conduction and convection and are calculated as follows:

$$\boldsymbol{k}_D^{(e)} = \int_{V_e} \left(\frac{\partial \boldsymbol{N}^T}{\partial x} D_x \frac{\partial \boldsymbol{N}}{\partial x} + \frac{\partial \boldsymbol{N}^T}{\partial y} D_y \frac{\partial \boldsymbol{N}}{\partial y} + \frac{\partial \boldsymbol{N}^T}{\partial z} D_z \frac{\partial \boldsymbol{N}}{\partial z} \right) dV \tag{5.26}$$

$$\boldsymbol{k}_g^{(e)} = \int_{V_e} g\, \boldsymbol{N}^T \boldsymbol{N} dV \tag{5.27}$$

The $\boldsymbol{f}_Q^{(e)}$ is the vector associated with the external heat applied on the element, obtained with the integral in the next equation

$$\boldsymbol{f}_Q^{(e)} = \int_{V_e} g\, \boldsymbol{N}^T \boldsymbol{N} dV \tag{5.28}$$

The integral in equation (5.26) can be rewritten in the matrix form with the definition of the matrix $\boldsymbol{D}$,

$$\boldsymbol{D} = \begin{bmatrix} D_x & 0 & 0 \\ 0 & D_y & 0 \\ 0 & 0 & D_z \end{bmatrix} \tag{5.29}$$

and $\boldsymbol{B}$ (being nd the number of nodes of the element under analysis) given by

$$\boldsymbol{B} = \begin{bmatrix} \frac{\partial \boldsymbol{N}}{\partial x} \\ \frac{\partial \boldsymbol{N}}{\partial y} \\ \frac{\partial \boldsymbol{N}}{\partial z} \end{bmatrix} = \begin{bmatrix} \frac{\partial N_1}{\partial x} & \cdots & \frac{\partial N_{nd}}{\partial x} \\ \frac{\partial N_1}{\partial y} & \cdots & \frac{\partial N_{nd}}{\partial y} \\ \frac{\partial N_1}{\partial z} & \cdots & \frac{\partial N_{nd}}{\partial z} \end{bmatrix} \tag{5.30}$$

Using the two previous equations it can be verified that

$$\boldsymbol{B}^T\boldsymbol{D}\boldsymbol{B} = \frac{\partial \boldsymbol{N}^T}{\partial x} D_x \frac{\partial \boldsymbol{N}}{\partial x} + \frac{\partial \boldsymbol{N}^T}{\partial y} D_y \frac{\partial \boldsymbol{N}}{\partial y} + \frac{\partial \boldsymbol{N}^T}{\partial z} D_z \frac{\partial \boldsymbol{N}}{\partial z} \tag{5.31}$$

therefore, the equation (5.26) can be rewritten as follows:

$$\boldsymbol{k}_D^{(e)} = \int_{V_e} \boldsymbol{B}^T\boldsymbol{D}\boldsymbol{B}\, dV \tag{5.32}$$

The result of the last equation is exactly the same as the matrix that would be obtained with Hamilton's principle (an energy principle) used in solid mechanics, except the matrix of material elasticity is replaced by the matrix of heat conductivity. The same happens with the matrix of thermal convection and the mass matrix obtained with the energy principle, so it is observed that the Galerkin method produces the same set of FE equations as those produced by the energy principle [24].

With all these equations and data, and the determination of the element matrices, the residual defined by equation (5.23) can now be assembled for the global domain and enforced to equal zero, which will lead to the following global system equation:

$$\boldsymbol{K}\boldsymbol{D} = \boldsymbol{F} \tag{5.33}$$

where $\boldsymbol{K}$ is the sum of $\boldsymbol{k}_D$ and $\boldsymbol{k}_g$. The last equation has the same form as that for static mechanics problems, but regards a different variable field (temperature), calculated using other material properties, specific for heat transfer problems, such as, for example, thermal conduction and convection matrixes [24].

Chapter 6

6. Software validation

Throughout this work the FEM simulations will be performed using an academic software, developed at FEUP, in the Computational Mechanics Research Laboratory - CMech-Lab (cmech.webs.com), the Finite Element Method Analysis Software (FEMAS). This software can solve different computational mechanics problems using not only FEM, but also meshless methods. The software validation will be made on a comparative basis running a benchmarking example with only the FEM, in different mesh types and sizing, in both FEMAS and ANSYS©. The purpose of this example is to compare the final results regarding the structure displacements and stresses, as well as the plotting of the stresses along interest lines on the solid.

6.1 Finite Element Method Analysis Software

As aforementioned, this software was developed at the Faculty of Engineering and can be used to solve a wide spectrum of different mechanical applications using the FEM and meshless methods. This software is implemented in MATLAB© and has a graphical user interface (GUI) that allows the user to build or import models and run the numerical analysis. The range of parameters that set the numerical analysis is immense and this software also has the ability to import meshes and models generated in specialized software and then perform numerical analysis on the imported meshes.

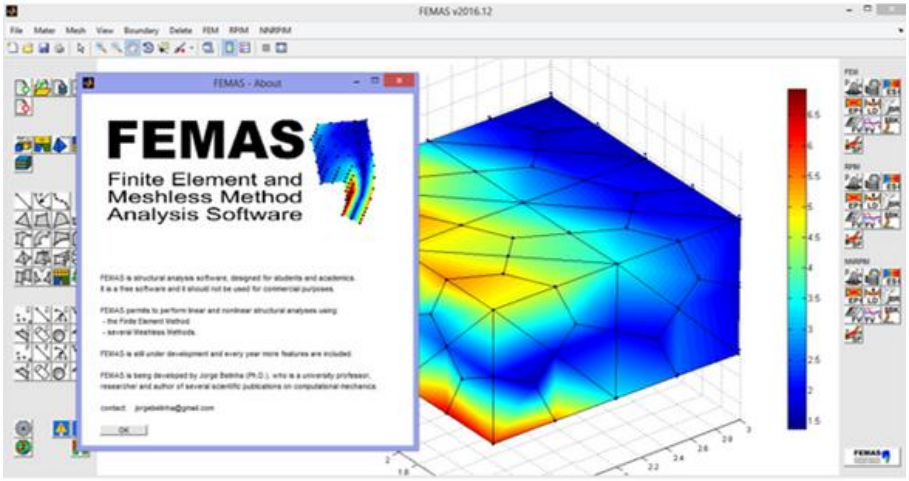


Figure 21 - Graphic user interface of FEMAS [25].

The Radial Point Interpolation Method (RPIM) and the Natural Neighbour Radial Point Interpolation Method (NNRPIM) are two different meshless methods supported by FEMAS. The given software, which is permanently being improved and developed, is now able to perform the several analyses, such as linear elastostatic; non-linear elastostatic; crack propagation; free vibrations; bone tissue remodelling; buckling; static fluid flows and steady heat transfer.

The validation example was performed with the linear elastostatic analysis which is divided into three phases being them the pre-processing, with the construction of the shape functions and the integration of the mesh followed by the processing. This second phase is based on a standard computational mechanics procedure. The first phase of the processing is the construction of the material matrix, followed by the determination of the local stiffness matrices (assembled afterwards into the global stiffness matrix). Then, the force vector is constructed, and the essential boundary conditions are imposed. The final stage of this particular phase is the calculation of the displacement field used to obtain the strain and, consequently, the stress field. The final phase is the post-processing using the GUI, where the chosen field variables can be represented throughout the analysed component. The data of the computational simulation is stored in an Excel© file with a matrix with all the information about the application (from the nodal coordinates until all the stress and strain information for each node).

6.2 Cook's Membrane - Convergence example

The benchmarking example used to validate the academic software is the Cook's membrane, which was analysed in two and three dimensions with the FEM in both ANSYS© and FEMAS [26]. This is a very common example and

it is supposed to have as outcomes the displacements and stresses registered on the structure for different meshes parameters. The simulations were performed in ANSYS© and FEMAS in two kinds of different meshes both in 2D and 3D cases. The properties of the material used in the study are similar to the structural steel and are shown in Table 2:

Table 2 - Material properties used o tests.

Property	Value
Young Modulus (E)	2.5e5 MPa
Poisson's Ratio (v)	0.3

The membrane geometry is presented in the figure below and, as it is shown in it, the structured is fixed on the edge [AB] and is loaded along the edge [CD] by an edge traction with a total load of 1N. On the right-hand side figure below there is the indication that the displacement along *Oz* axis (*w*) of the plane was assumed to be zero for better results, because it would make it possible to guarantee that the vertical displacement (*v*) along *Oy* would not be affected by a deformation along the thickness of the structure. The non-existence of this displacement also represents a non-distortion of the mesh on 3D simulations in the tetrahedral case.

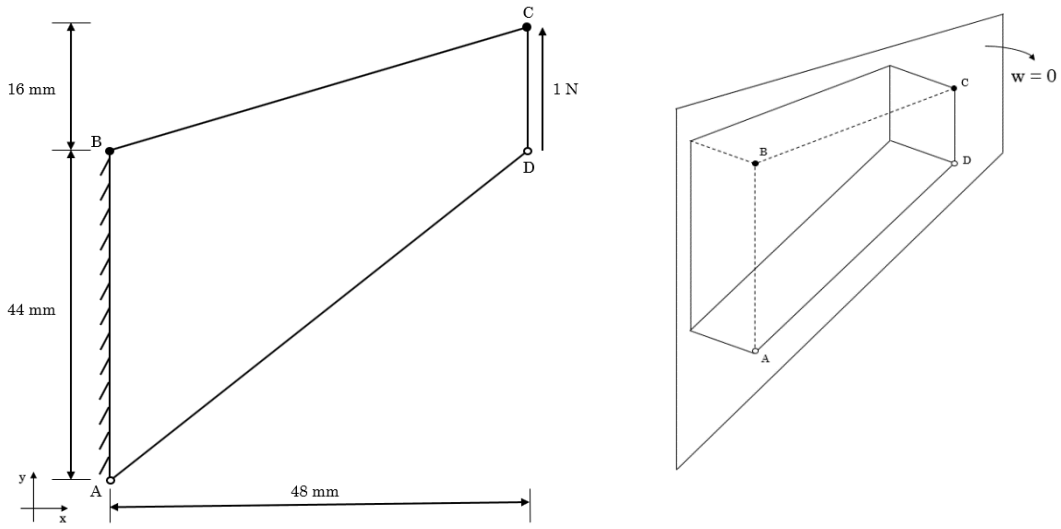


Figure 22 – Two (left) and three-dimensional (right) geometry (in mm) of the Cook's membrane.

For the 3D simulation, the thickness *T* of the membrane was variable according to the nodal distance along the [CD] edge. The thickness' dimension definition was associated to the use of three nodes in its direction and their nodal distance, which was defined by the distance between the nodes in de *x0y* plane in the 16mm edge for each different mesh. This procedure was used

throughout the whole process for the sake of a fully regular meshing of the structure, as it can be observed in the figure below. It is simply to deduce that increasingly refined meshes will have smaller thicknesses associated.

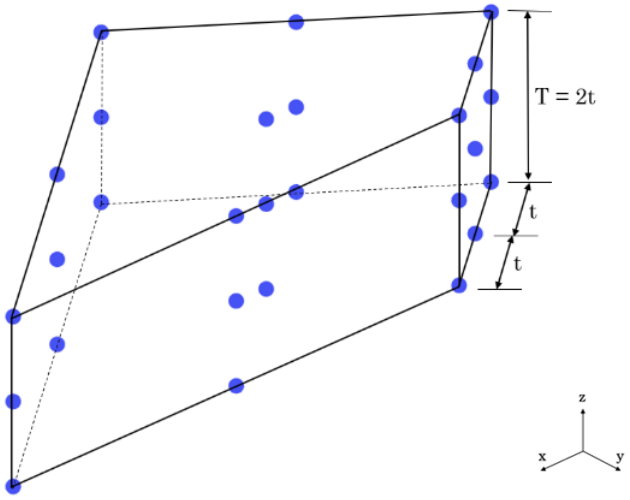


Figure 23 – Thickness (T) calculation with nodal distance t.

In Figure 23 it is shown a 3D structure with 2x2 divisions on the *xOy* plane and another 2 divisions on the thickness direction. The number of divisions in this last dimension is fixed, while the number of elements on *xOy* plane will increased for the double in each test. This increment will reduce the nodal distance between the nodes, and, because of this fact, the thickness of the structure will continually decrease with refined meshes.

6.2.1 Meshing

The 2D analysis were performed using quadrilateral and triangular meshes whereas the 3D simulations were carried out using tetrahedral and hexahedral elements. The number of elements across the edges on the xOy plane was of 2^n with $n = (1, 2, 3, 4, 5, 6, 7)$ for the two-dimensional simulations and $n = (1, 2, 3, 4, 5)$ for the 3D, due to computational limitations.

The following tables resume all the information regarding the number of elements and nodes used in the 2D and 3D simulations, as well as the thickness of the membrane in the three-dimensional studies (Table 4).

Table 3 - Meshing parameters for two-dimensional simulations.

2D	div *xOy*	elements	nodes
M1	2	4	9
M2	4	16	25
M3	8	64	81
M4	16	256	289
M5	32	1024	1089
M6	64	4096	4225
M7	128	16384	16641

Table 4 - Meshing parameters for three-dimensional simulations.

3D	div *xOy*	div T	T	elements	nodes
M8	2	2	16	8	27
M9	4	2	8	32	75
M10	8	2	4	128	243
M11	16	2	2	512	867
M12	32	2	1	2048	3267

Some of the meshes used both on 2 and 3D tests are shown on the figures below. As it can be observed, the triangular (2D) and tetrahedral (3D) meshes, showed on the right-hand side of Figure 24, are different when comparing the ones obtained in FEMAS and ANSYS©. The academic software can generate structured triangular meshes contrary to ANSYS©, where the meshes are not structured and therefore the final results differ more because of this. Both rectangular (2D) and hexahedral (3D) meshes are structured on both software and consequently the convergence of the results is supposed to be better on these examples.

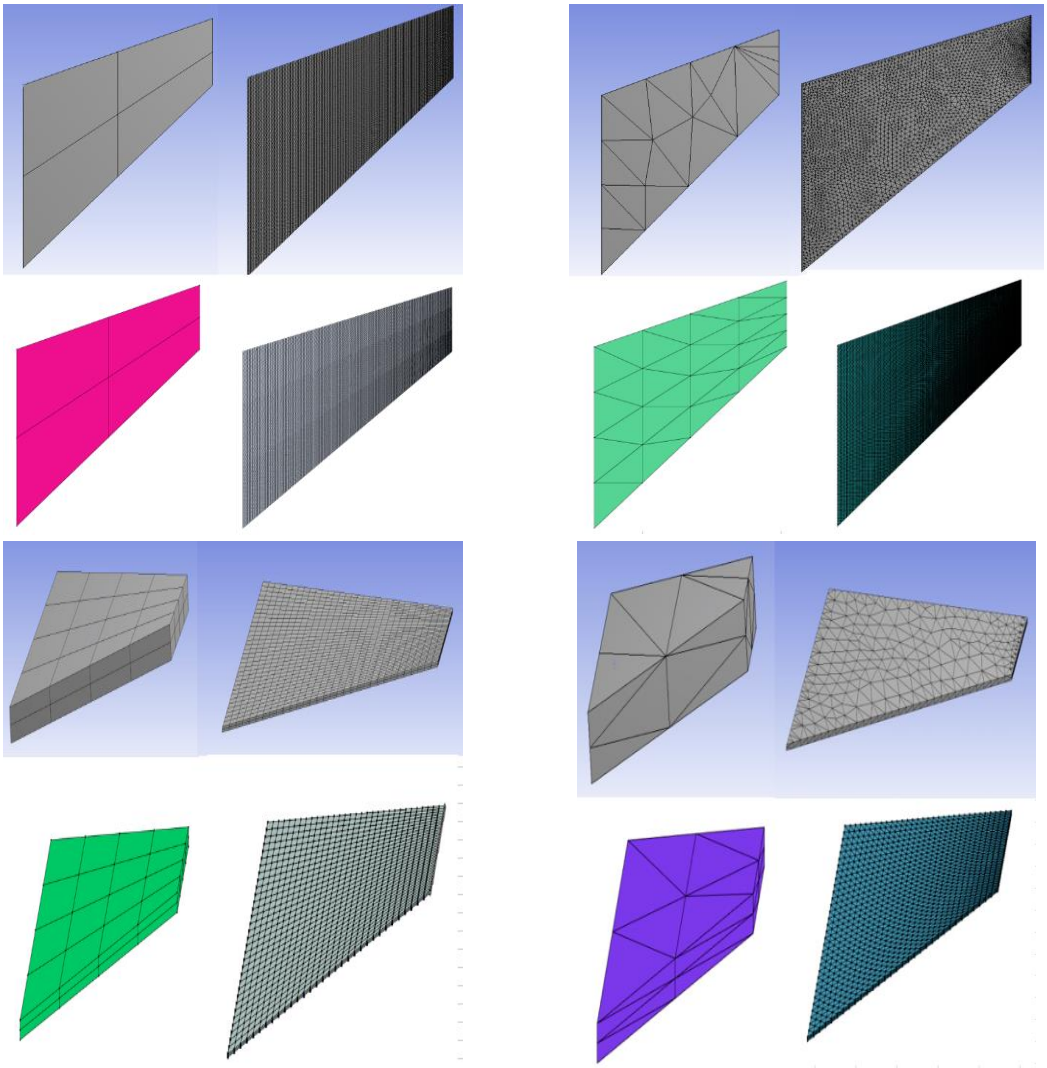


Figure 24 - Different meshes comparison between ANSYS (with a blue background) and FEMAS (with a white background).

6.2.2 Results and discussion

To certify the validation of the software in use, the results (of FEMAS and ANSYS©) must approximate into a converged value, generating a plateau of solution values with the increase of nodes discretizing the problem domain, for both the 2D and 3D tests.

Recalling Figure 22, the results registered were both the horizontal and vertical displacements for the point C and the Effective-Stress (Von Mises) and normal-stress along the *Ox* direction for point B for every simulation performed along the process. The results related to the quadrilateral and hexahedral meshes are expected to have a better relation due to the better quality of the meshing used, whereas the triangular and tetrahedral meshes should not be able to deliver results showing the same accuracy and convergence rate. It is also important to state that the convergence study of

the 3D simulations, because of the use of sparser meshes (due to computational limitations), is not capable to deliver a plateau of convergence as it is expected in 2D simulations.

Firstly, the results of the displacements obtained in the tests performed will be compared and, only posteriorly, the comparison of the stresses' results (both in value and in colour-map) will be made. The results of displacements found in the point C in Figure 22 for the analysis performed in two dimensions are shown in the following graphics, in Figure 25 and in Figure 26. As expected, the results for the 2D simulations converge to a value, supposed to be very close to the final converged result. The obtained final values (for the denser mesh) were approximately: 1.25e-4mm for the horizontal displacement and (-)9.38e-5mm for the vertical displacement.

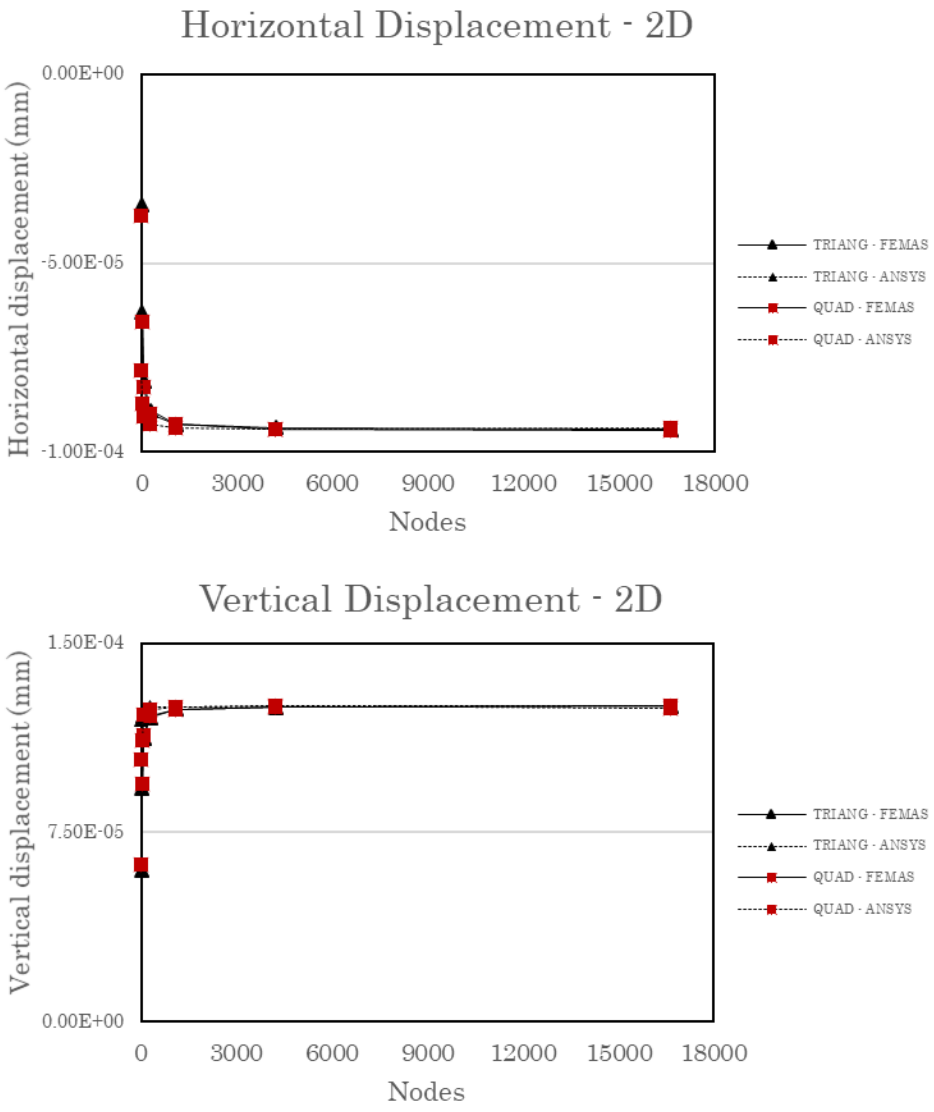


Figure 25 - Horizontal (above) and vertical (below) displacements results for 2D simulations.

For 3D simulations the results obtained (see Figure 26) on the same point with the hexahedral meshes in both software have almost the same results in every simulation performed, whereas the tetrahedral elements based meshes do not present the same high converge rate as the hexahedral meshes. Notice that the denser tetrahedral mesh (3267 nodes) is not sufficient to achieve the value obtained the equivalent hexahedral meth. This was verified with the simulations, and the values are consistent with the assumptions made before the software analysis. Additionally, because the meshing method was not the same in both software for the tetrahedral elements and because the mesh was the same in ANSYS© and in FEMAS, in hexahedral case, the hexahedral results are very close to each other and the evolution of the curve obtained is identical for both computational analyses carried out. These results allow to validate FEMAS software.

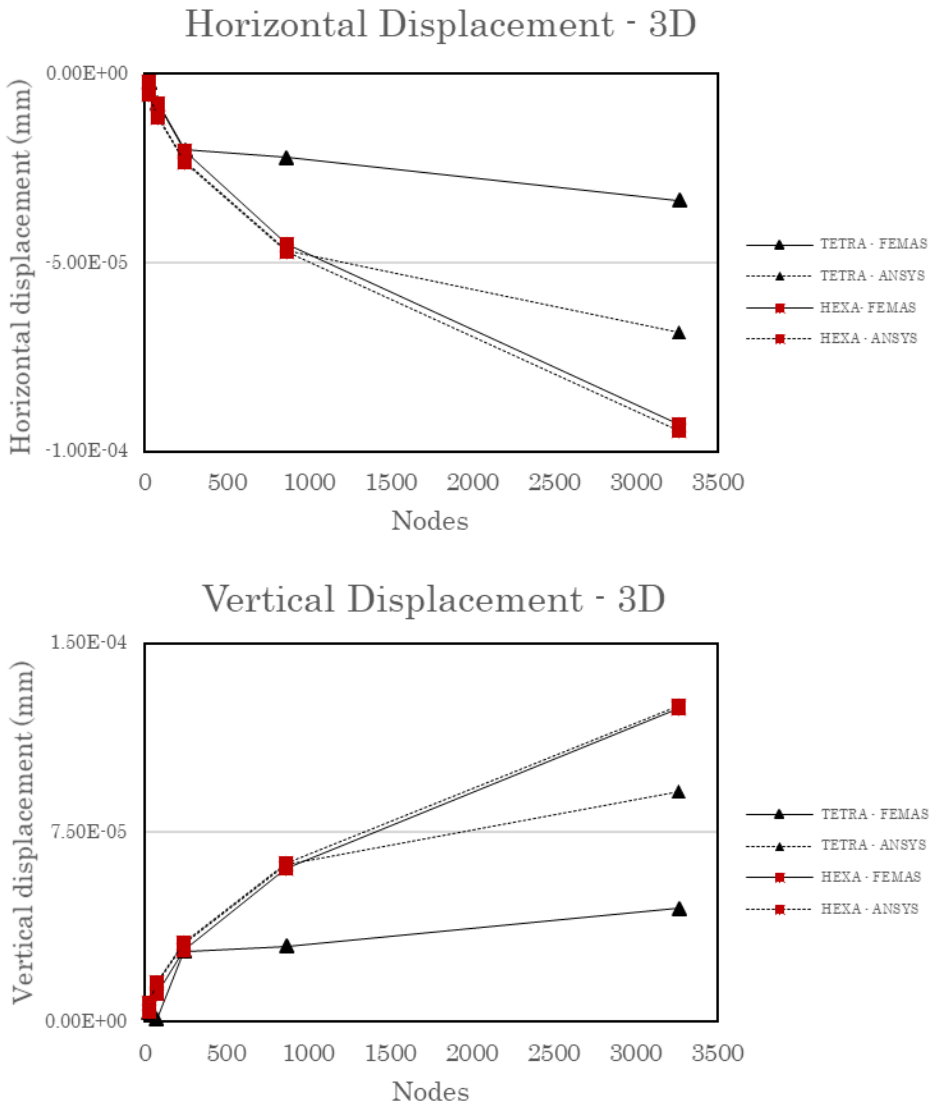


Figure 26 - Horizontal (above) and vertical (below) displacements results for 3D simulations.

As outlined above, the simulations performed in two dimensions have the most refined meshing parameters, leading to 16384 elements (128x128 along the edges). This number of elements is more than enough to show the convergence of every kind of simulation to a certain value and a plateau of results. As it is intuitively easy to observe, and shown in the previous graphics, the results' difference between both software decreases with the rise of the number of nodes. With all this, it is proven the validity of FEMAS to perform 2D simulations with good-quality results when meshes are refined enough.

Regarding now the 3D simulation, because of a smaller number of nodes used, the possible convergence and the plateau of values was not achieved. The impossibility of performing 3D tests with more elements was vital to the inability to achieve those kinds of results, but in spite of the meshes' sparseness used, in the hexahedral method, the results obtained in FEMAS were very close to ANSYS©, proving the validation of the software when comparing the same meshing method.

In relation to the stresses' results, the assumption of better convergence for the 2D analysis is maintained. However, it may exist a larger difference between the results of both software related to the extrapolation of the tensions from the integration points to the nodes. This can explain the differences of the values registered both for the 2D and 3D simulations, especially in sparser meshes and when using different meshing methods as it occurs with triangular and tetrahedral based meshes in FEMAS and ANSYS©.

As previously mentioned, the results stored for the comparison of values obtained in both software were the normal-stress along the *Ox* axis and the Effective-Stress (Von-Mises) for the point B of the Figure 22.

Regarding 2D simulations there is a plateau of values obtained with more refined meshes and the convergence was achieved as well, for stress calculations. There are some differences registered that, maybe, are related to the extrapolation of the values calculated from the integration points to the nodes of the elements, but it is proven, once again, that the software can obtain good results for tensioning components.

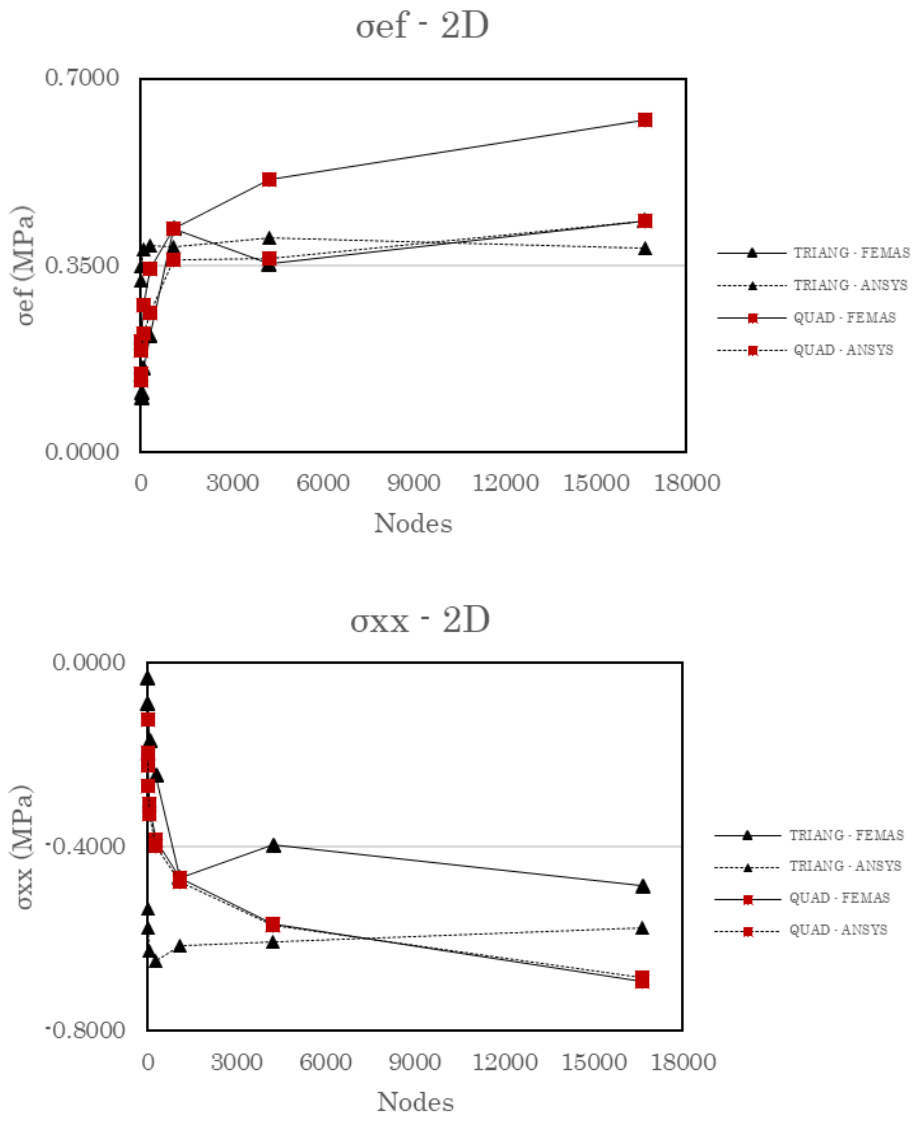


Figure 27 - Effective-stress (Von Mises) (above) and Normal-stress along *Ox* (below) for two-dimensional simulations.

About 3D stresses' analysis, the values are slightly different in the tetrahedral elements on the refined mesh for the normal-stress along the axis *Ox*, but for the same meshing parameters of the hexahedral meshing the evolution of the results was very satisfactory, and the values are practically the same, especially in σ_{ef} graphic. There is a particular case, for sparser meshes, of a peak registered in both (tetrahedral and hexahedral) of M9 mesh (Table 4) in ANSYS, but these results should be admitted as a numerical error due to the lack of elements in the analysis that originated a difference in the obtained data.

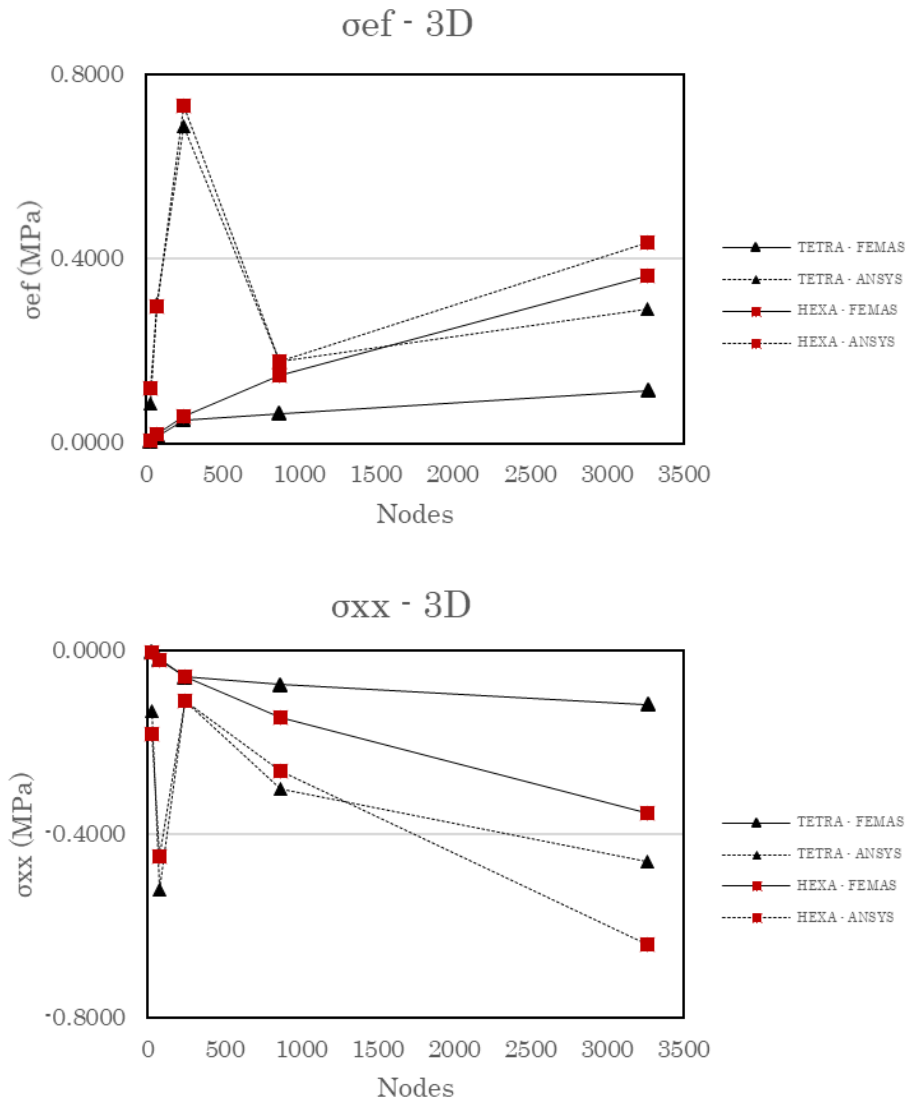


Figure 28 - Effective-stress (Von Mises) (above) and Normal-stress along Ox (below) for three-dimensional simulations.

Again, for the 2D and 3D simulations the obtained values were very accurate to what was previously expected for all types of elements used and the evolution of the curve demonstrates that the academic software can generate results as good as a commercial software used worldwide. The stresses obtained, when the meshing elements were the same, were very close for both software and, once again, the 2D analysis produced better results than the 3D. The values for the stresses given by FEMAS differ more from the ANSYS© than the displacements because of the extrapolation of the stresses from the integration-points to the nodes, as aforesaid. This data can be verified with the information displayed in the graphics above, and software validation is again verified for the calculation of stresses in a particular point of a given structure.

The colour-maps generated by FEMAS and ANSYS© are detailed in the figures below. These were acquired directly after the simulation was completed in both software and Figure 29 and Figure 30 are related to the 2D simulations performed, whereas Figure 31 and Figure 32 regard the 3D. These figures show the maximum and minimum values as well obtained.

The comparison of 2D simulations showed closer values for both software. The figures show identical maps for refined meshing, which does not happen in sparser meshes because of the lack of integration points in the elements. Observing the figures, the Effective-Stresses (Von Mises) had values close to zero across the surface except in the region of point B (see Figure 22), under tensile stress. Regarding Normal Stress along *Ox* a tensile loading is observed along all surface except in the region in study (point B, Figure 22) that is under compressive loading.

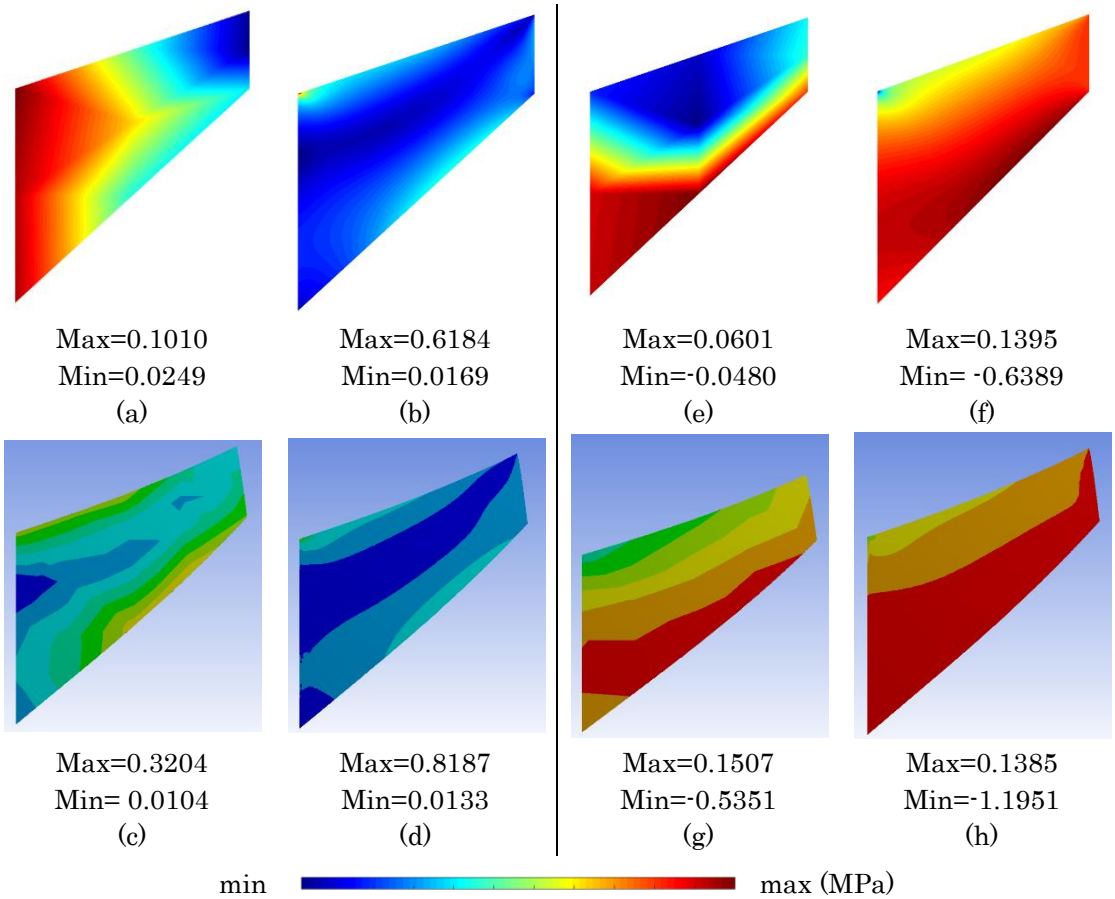


Figure 29 – Triangular 2x2 FEMAS (a) and ANSYS© (c); 128x128 FEMAS (b) and ANSYS© (d) σef values; 2x2 FEMAS (e) and ANSYS© (g); 128x128 FEMAS (f) and ANSYS© (h) σxx values

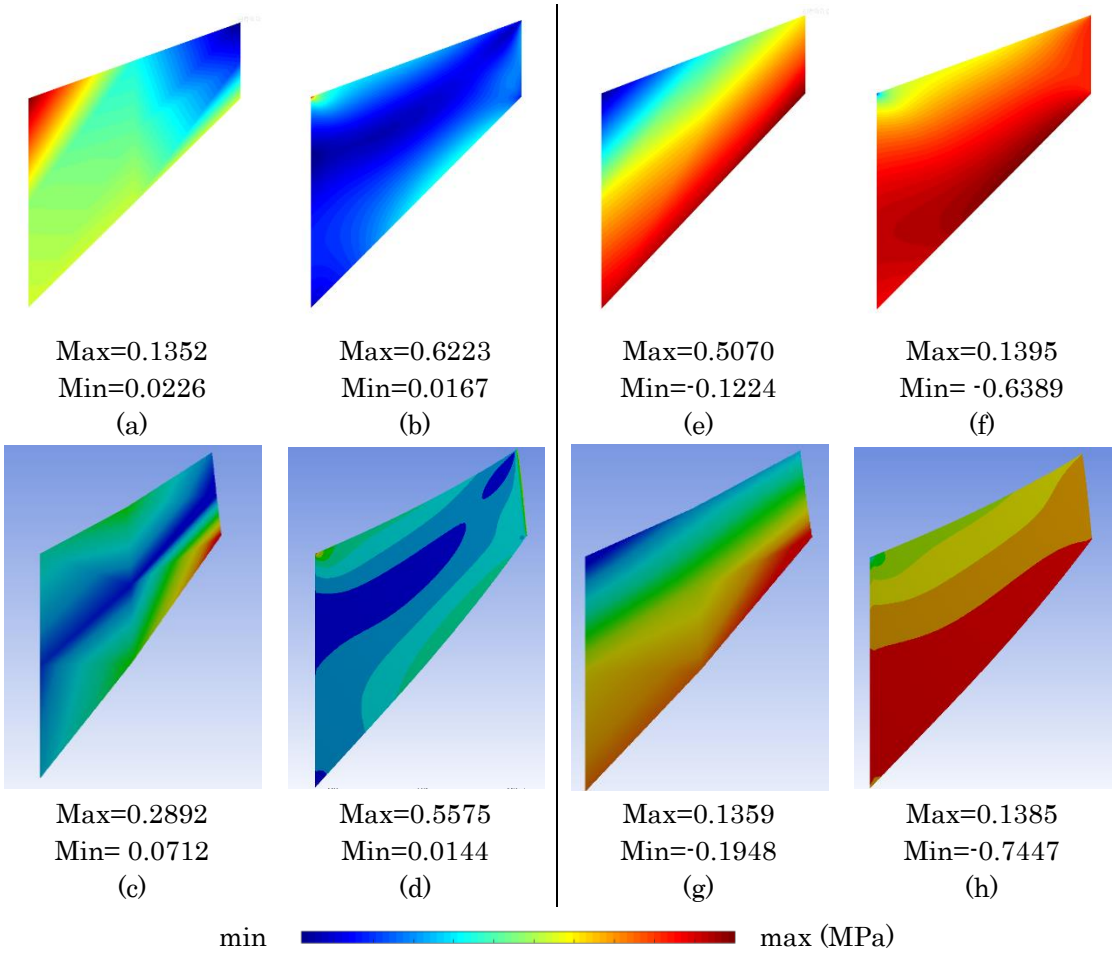


Figure 30 - Quadrangular 2x2 FEMAS (a) and ANSYS© (c); 128x128 FEMAS (b) and ANSYS© (d) σef values; 2x2 FEMAS (e) and ANSYS© (g); 128x128 FEMAS (f) and ANSYS© (h) σxx values.

About the 3D simulations, both software registered a good approximation with the 32x32 meshing, especially with hexahedral elements. In comparison with Figure 29 and Figure 30, the colour-maps have the same configuration with the Effective-Stresses (Von Mises) being distributed with values close to zero along the surface and the Normal Stress along *Ox* registering a large area where the loading represents a compressive stress in the lower region of the plots. Regarding σ_{ef}, there is again, in the region where the values were measured, tensile stresses performed by the load of 1N. The values were not as approximate as the 2D analyses performed by both software, especially with tetrahedral meshes, but it is proven the capability of FEMAS to perform correct FEM simulations, as well as the performance of this software to calculate and originate the colour maps of a structure under a specific loading.

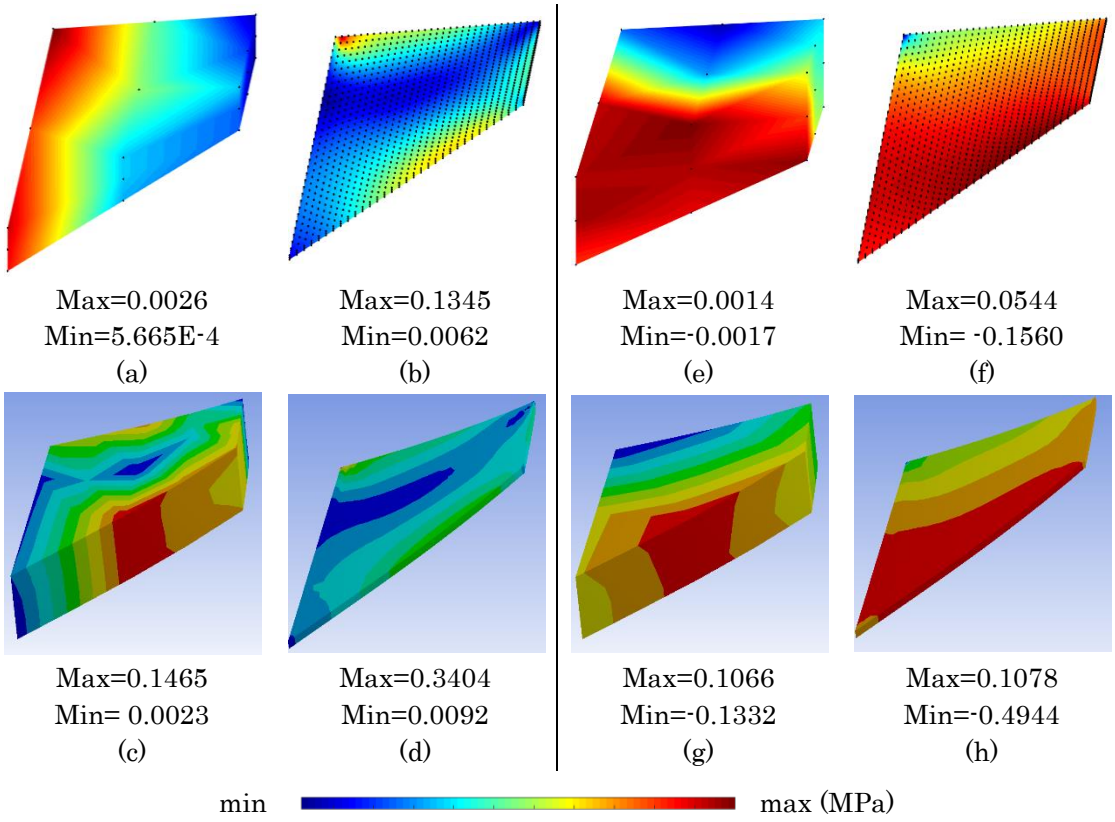


Figure 31 – Tetrahedral (3D) 2x2 FEMAS (a) and ANSYS© (c); 32x32 FEMAS (b) and ANSYS© (d) σef values; 2x2 FEMAS (e) and ANSYS© (g); 32x32 FEMAS (f) and ANSYS© (h) σxx values

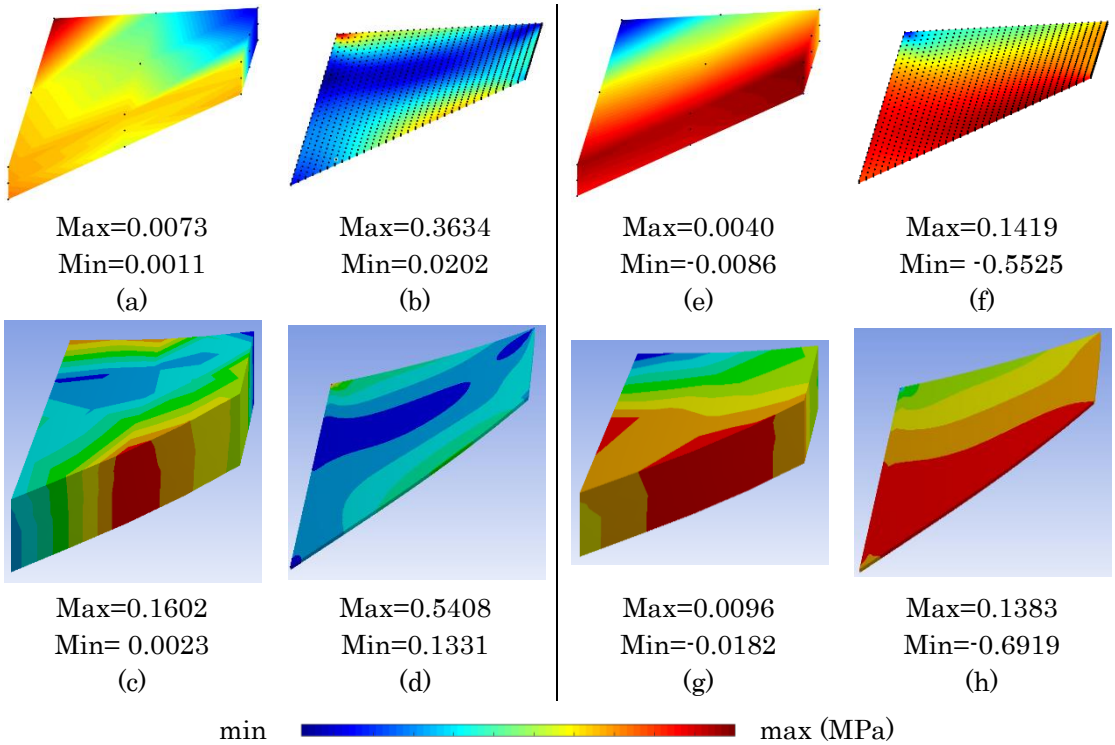


Figure 32 - Hexahedral (3D) 2x2 FEMAS (a) and ANSYS© (c); 32x32 FEMAS (b) and ANSYS© (d) σef values; 2x2 FEMAS (e) and ANSYS© (g); 32x32 FEMAS (f) and ANSYS© (h) σxx values

Chapter 7

7. PSI development

The instrument developed during this work is a PLA-based device that is supposed to adapt to the intercondylar notch geometry of the femur (after unfolding when exposed to the human-body temperature, 37ºC), being a fully customized PSI. All the aspects regarding the development (for instance, its shape, material properties and unfolding mechanism) will be thoroughly detailed in the course of this chapter throughout several tests and experiments to reach a possible solution that fulfils all the requirements. The approach used along this section was to carry out small-scale tests and, with their insights, move towards a real scale model of the instrument.

7.1 PSI requirements

The device under development during this work must comply several aspects in order to perform its functions correctly, regarding its dimensions, shape, mechanical and thermal properties. It is a SMP based device that allows orthopaedic surgeons to perform ACL arthroscopic reconstructions more accurately, guiding the tunnel placement to the correct position, previously studied and determined by the healthcare provider. This medical procedure is, as aforementioned, a minimally invasive surgery and because of this constraint, this device must have a cylindrical shape to fit the tube-shaped instruments showed in Figure 3, at low temperature (possibly 0ºC). When in contact with human tissues, it must be able to unfold assuming its working-shape, due to a heat-transfer process because of the temperature gradient (ideally from 0 to 37ºC, but presumably higher) to which the device is exposed inside the human body.

There are several constraints that should be respected for the further development of the PSI. Briefly, the PSI must fulfil:

1. Biocompatible material;
2. Thermoplastic material that suits 3D-printing technology requirements;
3. Patient-Specific properties, being customizable for each patient;
4. Cylindrical temporary shape at low temperature (below 37ºC);
5. Shape-changing ability;
6. Adaptability to intercondylar notch geometry (at 37ºC).
7. Determine the exact positioning and angle of the femoral tunnel drilling.

Regarding the first aspect, the material to be chosen should be biocompatible and biodegradable at some extent (it is impossible to remove all its content during surgery so there will always exist left-overs that must be absorbed in a rapid and easy manner by the human-body). This material must have a thermoplastic behaviour to comply the 3D-printing technology demands. AM and 3D-printing enable the possibility of patient-specific customization, which is what is intended for this kind of devices and that is why this will be the manufacturing process adopted to produce this instrument.

In what concerns the changing shape ability, this product has to fit, folded into a cylindrical shape, inside the tube-shaped instruments through where it will be putted in place during the surgical procedure. After its insertion in the human body, it must unfold when exposed to a temperature gradient (from the temperature in which it was previously stored until the 37ºC of the human tissues). In the unfolded state it should have a geometry analogous to the intercondylar notch, creating a negative geometry of this osseous entity. These unfolding effect will be performed with the aid of two different TEC materials that are expected to behave differently with the same temperature increment, where the one with the lower coefficient will expand less and be forced to deform by the material, which will register higher thermal expansion.

To accomplish these restrictions, an unfolding geometry has to be studied and dimensioned, respecting the dimensions of the instruments used throughout the medical procedure whilst respecting the intercondylar notch geometry.

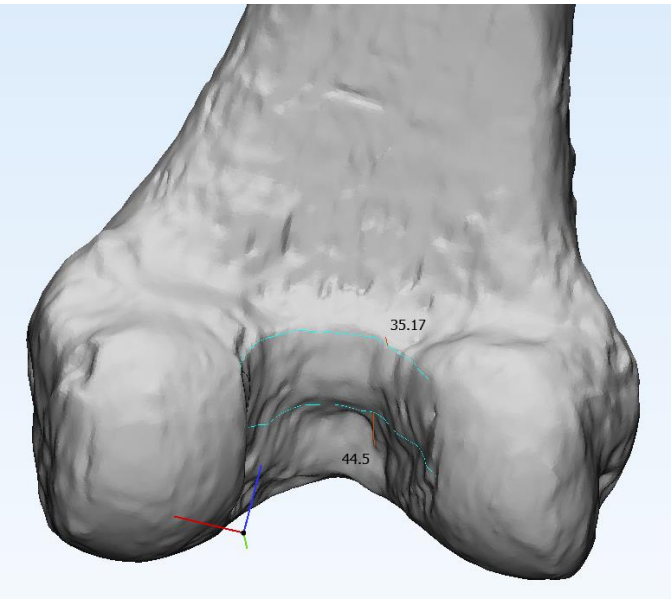


Figure 33 - Intercondylar notch proximal (35.17mm) and distal (44.50mm) portions length of a Femur model from CMECH-Lab database.

A key particularity in the healthcare provider point of view is the correct positioning to perform the drilling of the femoral tunnel in the predetermined positioning. The orthopaedist has to be able to choose the correct positioning through a CT and/or MRI generated model and these PSI will be produced in a way that this position should not be altered during the surgical procedure.

7.2 Small-scale 2D testing

Figure 33 shows a gross measurement of the length that should be totally covered by the PSI, obtained from a 3D model of a generic femur (from the database of CMECH-Lab). The less available space for the unfolded shape, the more challenging it will be to accomplish all the constraints showed in the previous section, since that a smaller structure is harder to deform under a heat-transfer process.

Consequently, the length chosen firstly and set as an objective to design the structure was the 35mm of the proximal portion. The solution to the unfolding process firstly tested was a division of these 35mm into smaller patches (1mm length) and the small-scale testing were carried out examining the thermal expansion of these substructures (with a fixed edge), with different configurations and designing.

The small-scale samples, with 1mm length, consist in two different patches formed by two distinct materials, one of which possesses a lower TEC compared to the other. The goal of assuming two different coefficients relies on the fact that the higher TEC material, corresponding to the higher

deformation rate during the heat-transfer process, will force a differential deformation between materials, leading to the pretended shape's formation. The material properties used as an input in FEMAS to perform the steady heat transfer simulations are shown in Table 5 . These material properties were obtained from CES Edupack PLA properties, as well as from some companies' technical datasheets.

Table 5 – Materials' mechanical and thermal properties used in small-scale tests [27].

Property	Material 1	Material 2	Unit
Young Modulus	3600	3600	MPa
Poisson's ratio	0.38	0.38	
Thermal Diffusion Coefficient	0.09	0.09	J/msK
Thermal Expansion Coefficient	41e-6 [28]	145e-6	strain/ºC

The patches' shape, design and material distribution across the samples make up the decision-making process of the PSI development and all the heuristics used to evaluate the influence of these parameters will be detailed in a thorough manner over the next subsections.

The tests were performed with the device unfolded, because it would be easier to design the samples' geometry and to simulate its behaviour under a constant heat-flux of a thermal gradient to the 37ºC. For the sake of this product development it is desired to observe the sample folding under these conditions. This behaviour was assumed to be possible to extrapolate to the inverse case, which is the actual function that it is required to accomplish, assuming that the material behaves elastically and expands from the folded to the unfolded position with the same values.

It was also assumed that all the 1mm portions of the final model should behave the same way, i.e., that they should have the same displacements between the beam's ends and, consequently the same angles.

To assess the feasibility of these first tests, the quantification of these parameters (displacement and angles) is necessary. The fixed edge implies a symmetry condition, so the real-scale tests will be performed with half model's length aiming a 90º folding of the geometry. These 90º guarantee that the whole PSI will fold the 180º required to adapt the femoral geometry and accomplish the given function, this condition will be detailed ahead in this work for further comprehension.

The entire model should have 35mm as stated before, but, given the fact that this is simply a generic measure, the calculations and tests were performed to a model with a length of 34mm, in order to have swifter modelling and designing processes, given that half a model would have 17 mm, instead of 17.5mm.

Once the model should fold 90º through the 17mm length, in the small-scale tests, regarding the 1mm samples, the angle between the lower edge and the end edge (r.h.s) of the 1mm samples is given by:

$$\frac{90}{17} = 5.294° \tag{7.1}$$

assuming the same folding ability for each one of the 1mm samples.

With the previous equation, it can be consequently obtained the desirable displacement (u):

$$\tan^{-1}\left(\frac{u}{1\ mm}\right) = 5.294° \Leftrightarrow\ u = 0.0926\ mm \tag{7.2}$$

Once these values are obtained, it indicates that (theoretically) the final 17mm model can fold until the 90º and the entire device (with 35mm length) can reach the femoral geometry (180º folding), accomplishing its requirements.

Now that the goal values were established, it will be shown the experimental methods used to reach the desired displacement and angles, that were focused on the geometry changing in a first approach and, in a second phase, were focused on the setting of a minimal temperature gradient to achieve the objectives of these tests. These first tests were performed to check which material distribution and configuration would allow higher displacements and, from that point on, that configuration could be used in the subsequent tests.

The goal of these small-scale tests is also to obtain insights that can lead to a more expeditious researching process when it comes to test the full-sized device, because not all the previous assumptions will be confirmed after a thorough examination of the results obtained.

7.2.1 Patch's shape selection

Initially, the first heuristic analysed was the possibility to choose between a rectangular or a splined patch. These two possibilities were taken into account because the first one was the simplest and easiest to design, whereas the second, theoretically, could favour the stress distribution resulting from the heat-transfer process.

The 1mm sample was divided, as previously stated, into two different patches, as shown in Figure 34. The patches in red have the higher TEC. Thus, for this reason, is the red material that will force the deformation of the other patches, showed in white. The experimental method used to assess

which was the evolution of the sample's deformation with patch's length ("a" in Figure 34) variation was to progressively increase this dimension (in 0.1mm intervals), as it is represented in the figure below, and perform a simulation under de temperature gradient of 37ºC, set as the ideal gradient because with this temperatures, the storing temperature of the device in development could be around 0ºC which can be reached with a regular freezer, without the need of a specialized hospital freezer which can withstand lower temperatures. This fact would also mean a lower amount of money needed to be invested by the Hospitals to implement this technologies.

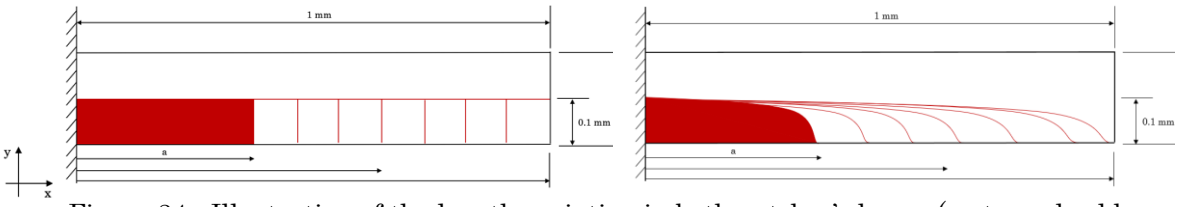


Figure 34 - Illustration of the length variation in both patches' shapes (rectangular l.h.s and splined r.h.s).

The results for the total displacement in the end edge midpoint and the maximum Effective-Stress are shown in Figure 35. After analysing the available data, it is possible to conclude that increasing the length of the patch (increasing the amount of higher TEC material) will also increase the deformation registered.

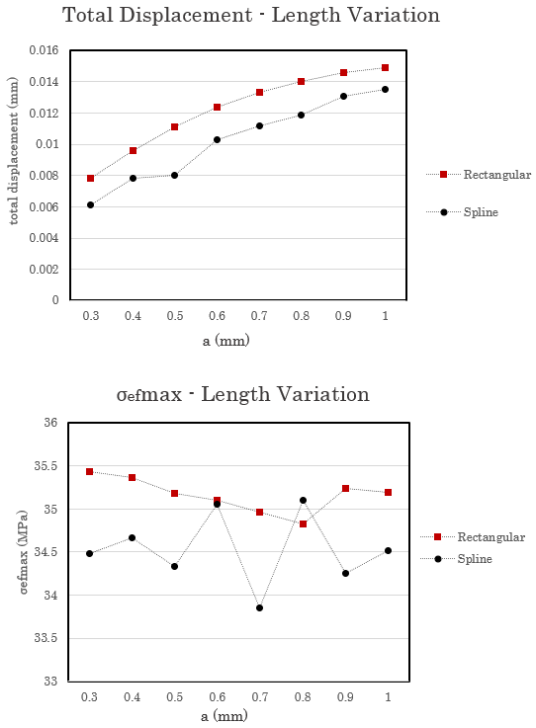


Figure 35 - Total displacement (above) and Effective-Stress (Von Mises) (below) evolution curves with patch's length increment.

Figure 35 allows one to conclude that the rectangular shaped patches translate into higher deformation rates with, generally, higher Effective-Stresses, in almost every case analysed. Even though this shape exhibits higher Effective-Stresses values, the maximum stress obtained with these simulations, as can be concluded when comparing the values showed in Figure 35 and Table 1 (see page 24), is well below the Tensile Strength of PLA. Consequently, from this point of view there are no drawbacks when it comes to choose the best shape to use in the final model. After checking the results obtained, it is possible to draw the conclusion that increasing the length of the patch also increments the displacements after the heat-transfer, preferably using the rectangular shape, once it is the one in which the deformation rates are higher. Regarding the patch's shape, a rectangular shaped patch is preferable, but there is a need to verify if these results are also observed in the width variation tests.

Once tested the length influence in samples' behaviour, it is necessary to assess which width is ideal to produce better results. Altering the patch's width is another aspect that needs to be tested to obtain the ideal patch shape and sizing. The simulations used to attest the best width were carried using a patch's length of 0.9mm, again in 1mm samples. The experimental method used was the same as in the previous test, this time changing the widths (represented as "e" in the drawings and graphs) from 0.05 to 0.15mm, in 0.025mm increments.

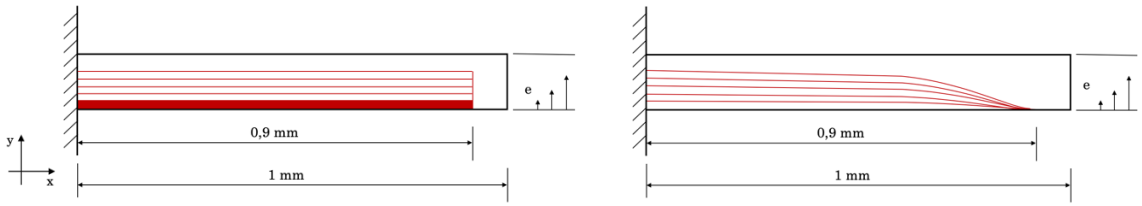


Figure 36 - Illustration of the width variation in both patch shapes (rectangular l.h.s and splined r.h.s).

The results (for total displacement (measured again in the end edge midpoint) and maximum Effective-Stress along the sample) given by the simulations are presented in Figure 37. Again, the rectangular shaped patch produced higher total displacements and stresses. For width variation, incrementing these dimension implies higher stress along the sample, but, as it happened in the previous test, the values registered were below the PLA's Tensile Stress. Yet again, these values do not imply a change regarding the material selection.

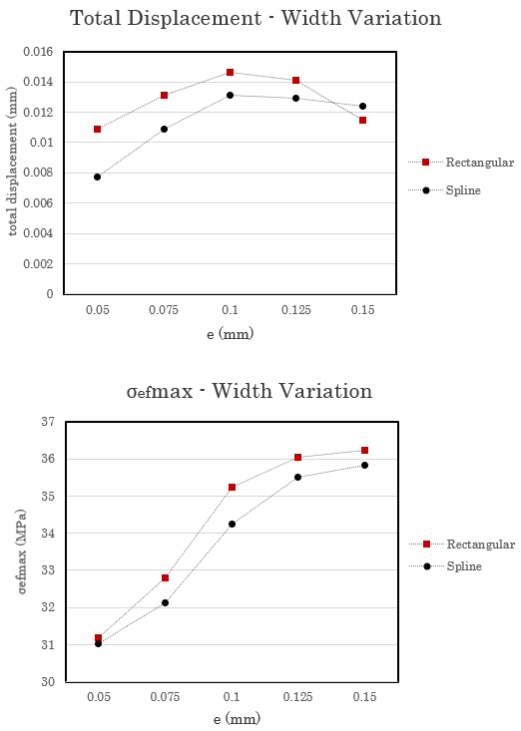


Figure 37 - Total displacement (above) and Effective-Stress (Von Mises) (below) evolution curves with patch's width increment.

Analysing the total displacement evolution curve, the more suitable patch's width is exactly half of the sample's width and this tendency was observed for both rectangular and splined shaping. The geometries that registered higher displacements were the 0.9mm and 1mm rectangular patches, both with 0.1mm of width, with 0.0147 and 0.0149mm, respectively, which are quite far from the final objective of these small-scale tests, see equation (7.2).

Once both tests are concluded, there are some ideas that can be already taken from the first simulations' results. Combining the insights given by both dimensional tests, the patch's geometry that induce more displacements would be a rectangular shaped, with half of the sample's width and a length that should be somewhere in between [0.9; 1] mm. There is some uncertainty regarding the possibility of using a patch's length correspondent to the total of the sample's, since it can be important to have a material alteration between patches, in the final model, to enhance deformations and the unfolding ability of the completed device.

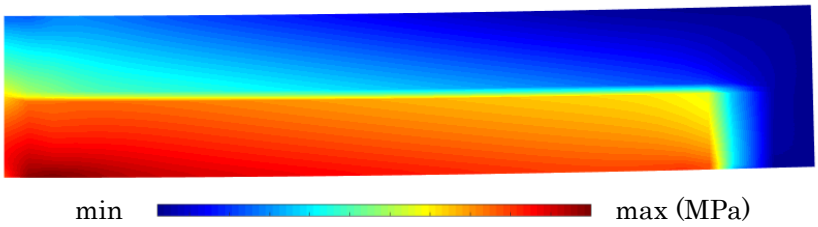


Figure 38 - Effective-Stress (Von Mises) obtained with a 0.9mm length patch, with a width of 0.1mm. (Min = 6.572 MPa; Max = 35.238 MPa)

Other possibilities that were considered regarded the using of several patches (with more material alterations along the sample, theoretically incrementing the deformation registered) or one single patch with different widths guaranteeing the material alteration between the different widths and, simultaneously, comply with the condition of having the total length of the patch with the sample's length (incrementing the amount of material with higher TEC). The first hypothesis was performed using a constant width of 0.1mm (the width that produced better displacements results) and changing the patch's length and, consequently, the interval between them. The second one consisted in changing both widths (e1 and e2 in Figure 39 r.h.s) and changing the patch's length, maintaining the interval between patches in 0.1mm. The results of the tests are displayed in graphics in Figure 40 and Figure 41.

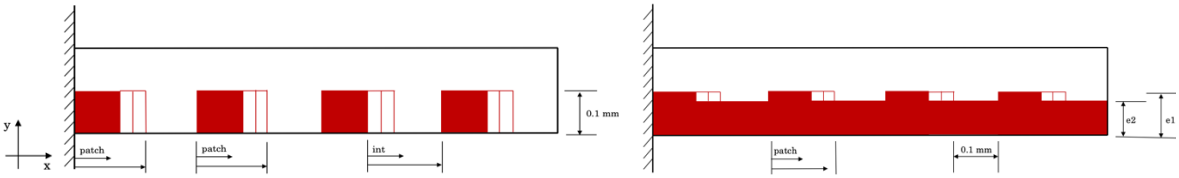


Figure 39 - Illustration of several patches (l.h.s) and different widths in one single patch (r.h.s).

In relation to the several patches case, it can be concluded that it did not improve neither the maximum total displacements nor the Effective-Stresses when compared to previous testing methods, once the results were almost the same as the registered in the rectangular patched (0.9 and 1mm) sample. Again, incrementing the patch's length improves the displacements observed, as it was expected, and the results for the stresses were almost the same. Another conclusion that can be taken from the graphs is that raising interval's length between patches decreases the total displacements observed, due to the fact that the amount of material with higher TEC used is lower. In what concerns to the Effective-Stresses, there is a peak in the 0.1mm patches, but apart from that, the values registered are concordant to the first tests performed, so there are no advantages in using the best geometry configuration obtained in this testing method.

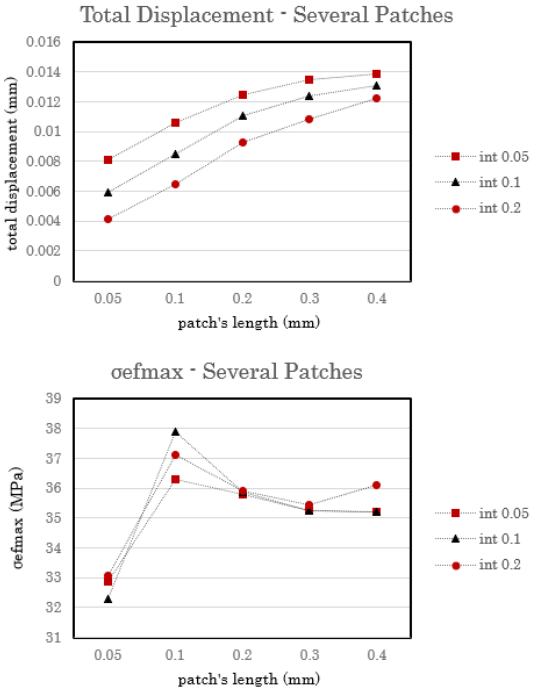


Figure 40 - Total displacement (above) and Effective-Stress (Von Mises) (below) evolution curves with several patches' configuration.

Concerning the using of one major patch with 1mm length with width variation along it, should increment the obtained values, since it was the geometry configuration that increased the amount of material with higher TEC. This experimental method involved changing the patch length and widths, i.e., there are two dependent variables being changed at the same time, and because of this, the conclusions that could be taken from it can depend on different aspects, becoming more difficult to determine which factors (and for what reason) are influencing the results generated by the simulations. Given the aforesaid, these tests were taken on, not to register a proper evolution curve but instead, to try to obtain a geometry that incremented substantially the displacements registered in previous testing methods.

Figure 41 shows the evolution curves of this testing methods and it can be observed that there is not a tendency in the results other than the fact that the 0.05mm patches registered smaller displacements and the 0.2mm recorded higher Effective Stresses. This insight is quite relevant because it states that more material changings across the length do not imply larger displacements. Instead, it is the shape and dimensioning of this material alteration that lead to higher deformation rates.

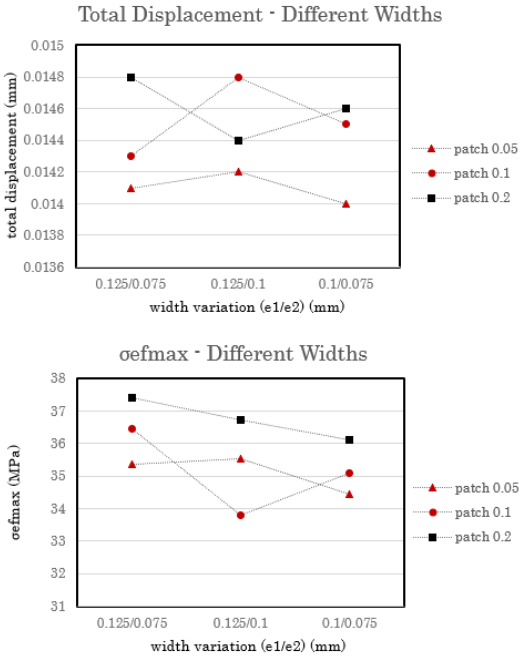


Figure 41 - Total displacement (above) and Effective-Stress (Von Mises) (below) evolution curves with one single patch with width variations.

The displacements obtained with the 0.125/0.075mm widths and 0.2mm patches' length, and 0.125/0.1mm with 0.1mm patches' length were the geometries that registered the best results with 0.0148mm of total displacement, comparing to the 0.0147mm of the 0.9mm, and the 0.0149mm of the 1mm rectangular patches of the first tests. These values are still below the final objective intended for these small-scale tests. Again, the Effective-Stress values are not close to the Tensile Strength of PLA, which allows to ignore these indicators to select the best geometry.

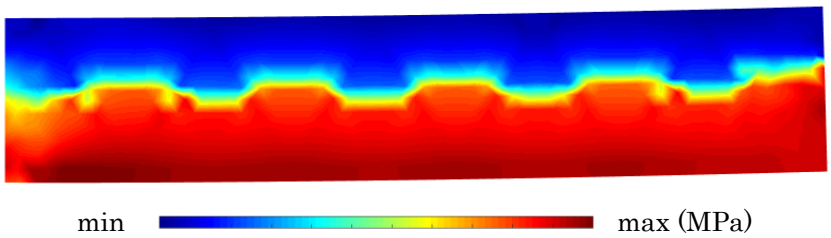


Figure 42 - Effective-Stress (Von Mises) obtained with width variation between 0.125/0.1mm and patch's length of 0.1mm. (Min = 7.538 MPa; Max = 33.784 MPa)

Once these values are almost the same as the ones previously obtained and the modelling of the geometries, as well as the meshing methods associated to it are more cumbersome, it was opted to use the geometry that was previously concluded to be the best: a rectangular patch with a length between the [0.9; 1]mm and a width of 0.1mm.

Given the fact that the results are still below the 0.0926mm intended, some principles that were being used in the previous tests, were changed in order to enhance the samples' folding ability.

As the deformations obtained using the previous methods were still below the objectives set, the existent FEMAS code was changed with the addition of a MATLAB© routine programmed (detailed on Appendix A) in order to swiftly apply large deformations using an incremental procedure based on small deformation theory. The routine will be further on identified as the "Incremental Procedure" for the FEM simulations. The theory that triggered its development is related to the study of infinitesimal conditions associated with varying a solution P of a problem to slightly different solutions Pε, where ε is a small number, or vector of small quantities [29].

The Incremental Procedure was used to divide the entire loading resultant from the thermal gradient in N (*n_incr* was the variable's name in the MATLAB© code) small quantities (that can be changed depending on the user's intention) and apply these quantities successively with small increments until the entire loading was achieved. Thus, the FEM solution of each small increment i (the displacement field $\boldsymbol{u}_i$) updates the geometry of the problem for the next increment $i+1$, by updating its nodal mesh ($\boldsymbol{X}_{i+1} = \boldsymbol{X}_i + \boldsymbol{u}_i$). This process allows to update the domain configuration in each increment, simulating a folding mechanism closer to the reality across the FEM simulations carried out.

After the routine's implementation in FEMAS, the geometries previously chosen should be tested to check the detection of some differences in the results. Once again, the colour-map of the stresses obtained is shown in Figure 43 and the maximum value of the total displacement was 0.015mm (almost the same, but slightly higher than previously obtained), with an angle of 0.418º, which are still 84% lower than the values intended, as follows:

$$difference = \frac{\|0.015 - 0.0926\|}{0.0926} = 84\% \tag{7.3}$$

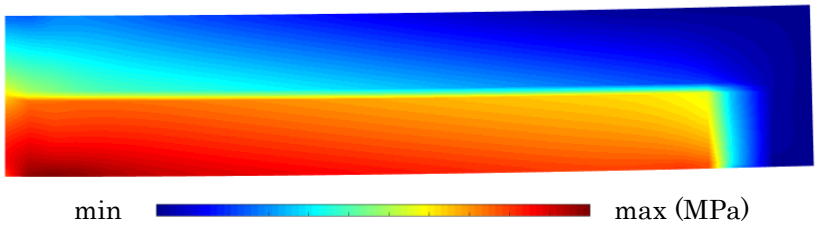


Figure 43 - Effective-Stress (Von Mises) obtained with a 0.9mm length patch, with a width of 0.1mm using the Incremental Procedure. (Min = 8.496 MPa; Max = 41.046 MPa)

With Figure 43 and the simulation performed with the Incremental Procedure approach, the displacements obtained are slightly higher, so this

routine can be used along the next FEM simulations to enhance the folding process, and its effect will have more impact in tests with larger geometric dimensions, closer to the reality.

Given the fact that the goal values are far away from the ones obtained with the simulations carried out until this point, it was decided to increase the temperature gradient to assess which was the minimal temperature difference that was needed to reach the goal values. This was a topic to be investigated, because if the temperature gradient was unfeasible (a temperature that was impossible to reach with an existent technology) or unachievable with the aid of a hospital freezer (because it only withstands minimal temperatures in the range of -90ºC, as will be detailed later on) the geometry or the material should be changed in order to obtain a device that can fulfil all the requirements.

After some iterations, and trial-error method, the gradient temperature needed to reach the 0.0926mm displacement (or 5.294º) was 250ºC, displayed in Figure 44, and the total displacement obtained was 0.0929mm (with an angle of 5.208º).

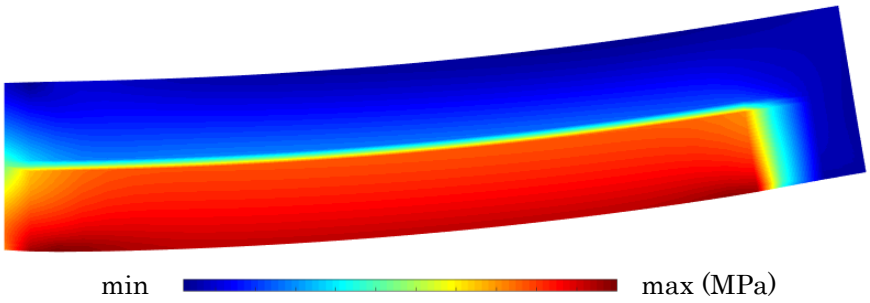


Figure 44 - Effective-Stress (Von Mises) obtained with a 0.9mm length patch, with a width of 0.1mm using the Incremental Procedure, with a temperature gradient of 250ºC. (Min = 52.617 MPa; Max = 243.431 MPa)

Although the displacements obtained are according to the objective, this temperature gradient of 250º is very high and difficult to obtain, which hinder its current usability under these conditions. In addition, the Effective-Stresses are much higher than the Tensile Strength of PLA, which is another aspect that assesses the impossibility of using the current geometry and sizing.

7.2.2 Patch's geometry and sizing alteration

As aforementioned, the dimensions used in the first tests performed made impossible the accomplishing of the theoretical folding expected for a total model of the PSI, based on the assumption that every sample of 1mm behaved the same way in the final model. Consequently, some preconditions had to be

changed in the small-scale samples. Diminishing the entire patch dimensions was the first idea, since that if there is a lower sample's width, it would be easier to fold. The total sample's length should not be changed, once it does not constraint the deformation of both materials. Actually, a higher length of the sample could enhance its folding ability, but when the total model was tested, there would be less material changing zones, which would not affect positively the results.

Adding to the variation of the sample's width, the approach thought was to induce a void in between both materials 1 and 2 along the patch's length. With this void, the material's behaviour was easier to predict, as well as it was expected to increase the obtained displacement differential, since there are less constraints to the deformation of the higher TEC material (material 2 in Figure 45). So, there were made some calculations to traduce the model's behaviour with the new configuration and thereby determine the maximum sample's width to force the materials to fold in the desired amount.

For instance, the geometry would be designed with the total width used in previous tests (0.2mm), inserting a void of 0.1mm between both materials (both with 0.05mm width), as can be seen in Figure 45.

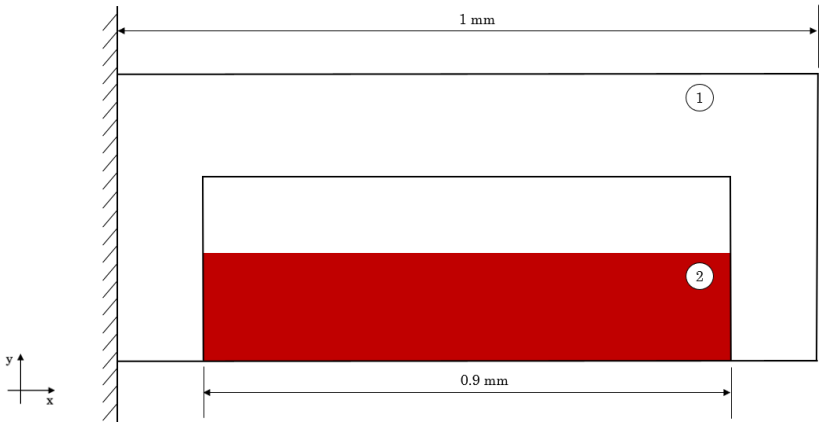


Figure 45 - New sample's configuration with a void between materials 1 and 2, used as model to the first calculations.

When exposed to the body temperature of 37ºC, both materials should deform in a distinct manner, showing different deformations along the length, as shows Figure 46. Note that the deformations are not at scale, being this figure a schematic representation of the expected deformation.

The theoretical quantification (under a thermal gradient (ΔT) of 37ºC and a patch's length (L_i) of 0.9mm) of the linear deformation along the length (notated as *Ox* axis) for both materials is given, based on the thermal linear expansion for solids, as an approximation, by:

$$\varepsilon_{xx}^{1} = \alpha_1 \Delta T = 41 \times 10^{-6} \times 37 = 1.517 \times 10^{-3}$$
$$\varepsilon_{xx}^{2} = \alpha_2 \, \Delta T = 145 \times 10^{-6} \times 37 = 5.365 \times 10^{-3} \quad (7.4)$$

being the displacement:

$$\delta_{xx}^{1} = \varepsilon_{xx}^{1} \, L_i = 1.517 \times 10^{-3} \times 0.9 = 1.363 \times 10^{-3} \, mm$$
$$\delta_{xx}^{2} = \varepsilon_{xx}^{2} \, L_i = 5.365 \times 10^{-3} \times 0.9 = 4.828 \times 10^{-3} \, mm \quad (7.5)$$

Once both displacements are obtained, the difference between them (δ) is easily calculated with the equation (7.6). This δ is the linear horizontal distance between the midpoints of the end edges.

$$\delta = \delta_{xx}^{2} - \delta_{xx}^{1} = 3.463 \times 10^{-3} \, mm \quad (7.6)$$

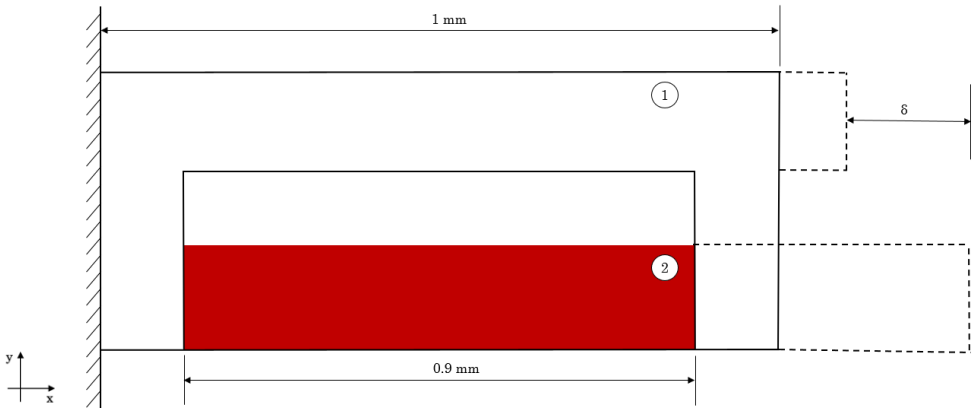


Figure 46 - Illustration of the deformation along the length of both materials, resultant from the heat-transfer process.

Clearly, the deformation does not occur just along the *Ox* axis, also across the width of the sample, and the Figure 47 shows an approximation of the resulting geometry after the process. Again, the following figure is not at scale, being a representation to let one understand why and how the calculations were made.

Because there are two deformations in the sample, the end edges are not vertical anymore, occurring an angle (θ) from the differential displacement. This angle allows the quantification of the goal values, because, once again, the final intention is to obtain a θ equal to 90º in the 17mm final model. Because of this, the quantification of the goal angle that should be obtained in the 1mm small-scale samples is:

$$\frac{90}{17} = 5.294° \quad (7.7)$$

Note that this is the same value that was set as a goal to perform the last section testing methods, but this angle is now measured between a vertical distance, between both midpoints of the end edges (λ), and δ. The final θ should be 90º, because, to reach the desired folded device, the final sample of the entire model should be in a vertical position, consequently, its end edges horizontally placed with θ as 90º.

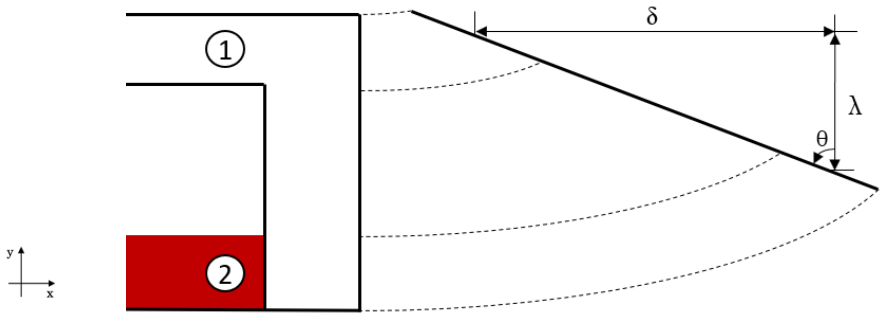


Figure 47 - Illustration of the real deformation happening during the heat-transfer process.

The λ obtained by the calculations will allow one to set the width of the final model, in a way that it will determine the maximum distance that is (theoretically) possible to use in order to accomplish the goals set, given certain conditions. The total width is thus obtained straight-forwardly, once λ is determined. So, now that all the variables needed to calculate which is the maximum vertical distance between the midpoints of the end edges are established, it is possible to calculate λ, given by the following:

$$tg(\theta) = \left(\frac{\delta}{\lambda}\right) \Rightarrow tg(5.294°) = \left(\frac{3.463 \times 10^{-3}}{\lambda_{max}}\right) \Leftrightarrow \lambda_{max} = 0.0374\ mm \qquad (7.8)$$

As λ_{max} is already quantified, the maximum distance between the midpoints of the patches that theoretically can, under a temperature gradient of 37ºC, allow the model to fold, is 0.0374mm. Therefore, in order to make it simpler to model the final geometry, the λ used was of 0.035mm.

Once λ is now defined, the samples' geometry to use in the first real-scale tests could be modelled and is showed in Figure 48. This geometry maintained, as previously stated, the 1mm samples, and the 0.9mm of patch's length. Some changes were made, regarding the void insertion and the placement of the patch. Initially, the patch was on the left of the sample, and it was moved to a centred position because, with this configuration there were two material changes across the sample's length, and it was expected to enhance the folding of the device. The selected void has a width of 0.005mm, because a bigger void could compromise the structural integrity of the PSI. λ

was designed to respect the 0.035mm length, and it is calculated with several components regarding the patch's and void's widths, as follows:

$$\frac{patch_1}{2} + void + \frac{patch_2}{2} = 0.015 + 0.005 + 0.015 = 0.035\ mm \tag{7.9}$$

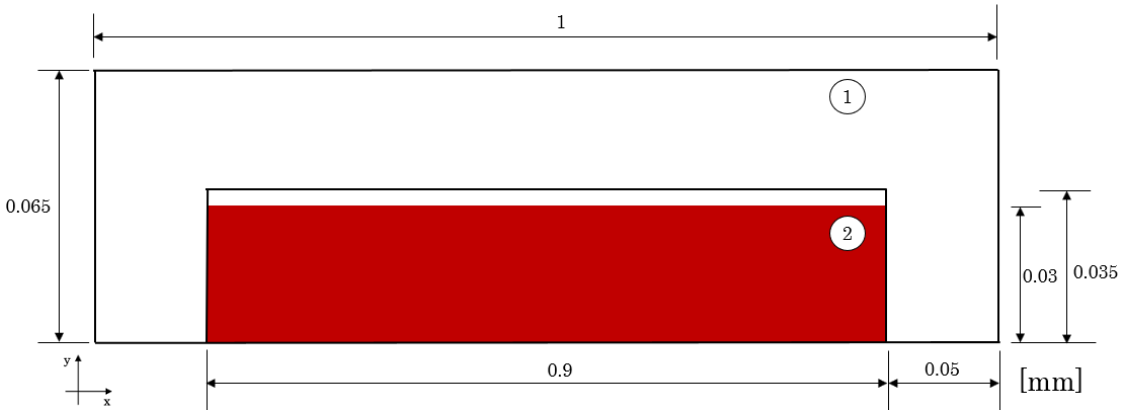


Figure 48 - Samples' geometry used in first 2D real-scale tests.

The sample's geometry presented in Figure 48 was assumed to be the final geometry that would accomplish the proposed objectives, and, assuming the calculations could give an accurate approximation of what would be presented after the simulations were performed, the first final 2D models were designed with the repetition of these 1mm samples through a length of 17mm.

7.3 Real-scale 2D testing

Once again with the Incremental Procedure, the first simulations, that should show the total folding of the structure until a vertical position, were carried out using the geometry showed in Figure 48. The results, for the Effective-Stresses (Von Mises) are displayed in Figure 49.

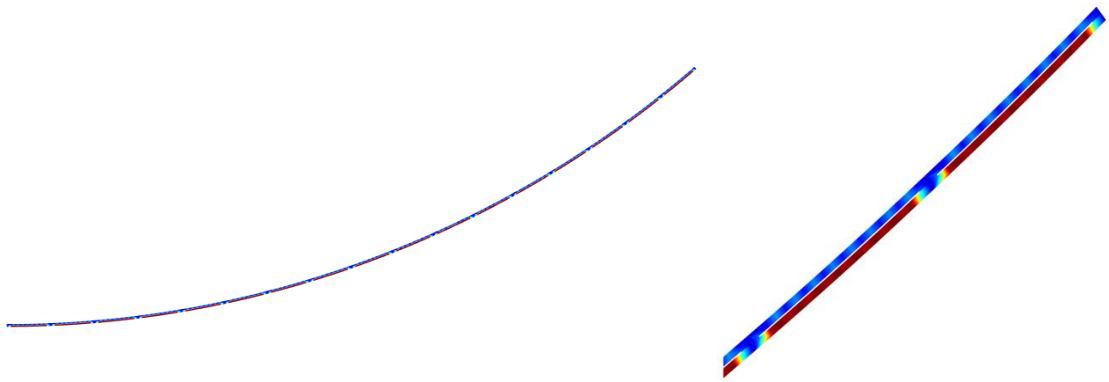




Figure 49 - Effective-Stress (Von Mises) for the 17mm model (l.h.s) with the Incremental Procedure, under a temperature gradient of 37ºC and a Zoom-In the final patch (r.h.s). (Min = 7.186 MPa; Max = 30.089 MPa)

Analysing Figure 49 thoroughly is possible to see that the results were not what was formerly calculated and the angle, between the vertical displacement of the final edge's midpoint and the horizontal distance between it and the fixed edge, was still far from the 90º that should be visible in this conditions. Another aspect that should be noted is that the Effective-Stresses are still below the Tensile Stress of PLA (see Table 1, page 24), so this still does not compromise the device's design. The results shown in the previous figure and their quantification allow the conclusion that the calculations performed were not an accurate approximation of what was previously established.

The next step taken was to carve each edge of the 1mm small samples. This carving process should create stress-concentration points, as well as ease up the folding process. All the measures of the performed carves are displayed in Figure 50.

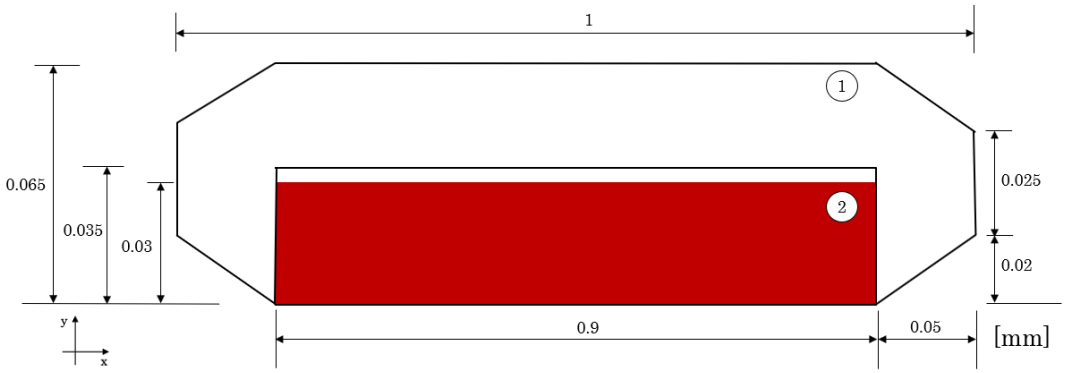


Figure 50 - Samples' geometry used in carved 2D real-scale tests.

The simulations carried out with the geometry represented in Figure 51 slightly enhanced the folding of the structure, but, as it can be concluded after checking it below, not enough to accomplish the total folding of the device. The stress-concentration could make it impossible to use this configuration, but the values are, once more, below the limits of the material in use.

The displacements registered were not what was expected, which means that even with lower width it is impossible, under the thermal gradient of 37ºC, to accomplish the desired values.

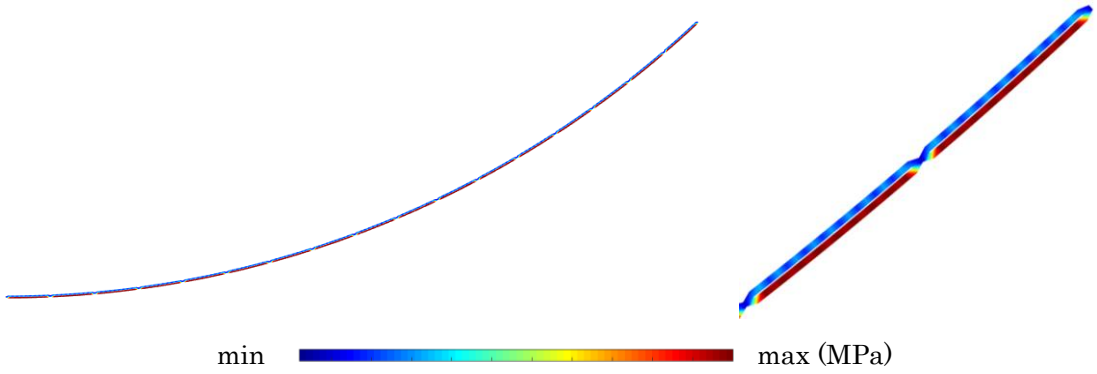


Figure 51 - Effective-Stress (Von Mises) for the 17mm carved model (l.h.s) with the Incremental Procedure, under a temperature gradient of 37ºC and a Zoom-In the final patch (r.h.s). (Min = 6.283 MPa; Max = 30.194 MPa)

After all the tests performed, both in small and real-scale, it was starting to be difficult to create more efficient geometries and patch distributions. Even with the void in between the materials, the displacements did not reach the goal values. Thus, it was decided to keep the last developed geometry and vary the thermic gradient.

7.3.1 Temperature gradient alteration

Since the geometries tested could not perform correctly under the 37ºC temperature gradient, this value should be changed, in such way that could allow the full folding process desired to this 2D tests.

The temperature gradient is calculated subtracting to the 37ºC of the human-body, which is the final temperature to which the PSI will be exposed, the temperature that the device will be stored after the 3D printing, inside a hospital freezer. Before the thermal gradient was changed, a research was made and it was found that there are several medical freezers that withstand the temperatures around -90ºC [30]. So, the maximum gradient that can be used in this case, to make it affordable and viable to use immediately in the orthopaedical market is:

$$\Delta T = T_{final} - T_{initial} = 37 - (-90) = 127℃ \quad (7.10)$$

It is important to state that lowering the temperature required to conserve the PSI inside the health-care institution, will increase the costs incurred when investing in this technology, since it will demand state-of-the-art devices to store the devices. This technology is often quite expensive, so, the risks that were incurred lowering the width of the model and could, eventually, harm its structural integrity, were precisely incurred to make it possible to design these PSIs with current technologies.

After a trial-error ΔT changing, the minimal temperature gradient that was found to be enough to fold the device in a sufficient manner was 80ºC, so, the storing temperature would be -43ºC, which is within the usual range of temperatures withstood by current hospital freezers. Using again the carved geometry designed previously (see Figure 50) with a FEMAS project that had a temperature gradient of 80ºC, the results obtained are satisfactory and accomplished the final goal of these 2D testing, folding the 90º that were desired, as can be seen in Figure 52.

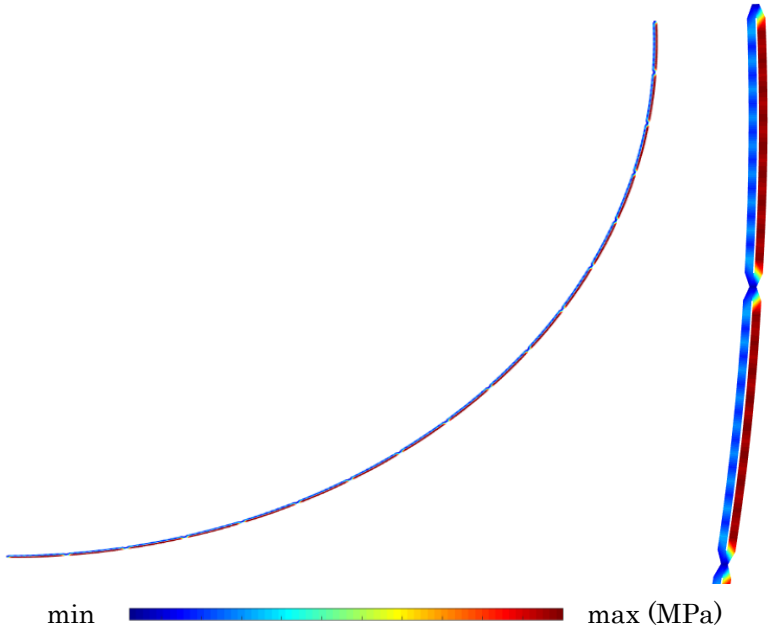


Figure 52 - Effective-Stress (Von Mises) for the 17mm carved model (l.h.s) with the Incremental Procedure, under a temperature gradient of 80ºC and a Zoom-In the final patch (r.h.s). (Min = 16.860 MPa; Max = 65.612 MPa)

After observing Figure 52, one can conclude that, even with higher Effective-Stresses, the values do not overpass the Tensile Strength of PLA, which make this temperature gradient suitable for the desired application. The values for Effective Equivalent-Strains were in between [0.355; 1.299] % thus below the PLA's Elongation (see Table 1, page 24) and, therefore good values to attest the application of this final geometry and temperature gradient to the development of this PSI technology. In FEMAS the Equivalent-Strains are calculated as follows:

$$\varepsilon_{eq} = \sqrt{\frac{3\left(\varepsilon_{xx}^2 + \varepsilon_{yy}^2 + \varepsilon_{zz}^2\right)}{2} + \frac{3\left(\gamma_{xy}^2 + \gamma_{yz}^2 + \gamma_{xz}^2\right)}{4}} \tag{7.11}$$

7.4 3D geometry validation

Once obtained a geometry that could accomplish the proposed objectives, a 3D test is needed to assess if the third-dimension could interfere in the displacements registered in the two-dimensional tests. To model the 3D device an extrusion of the 2D geometry was performed.

Figure 53, in l.h.s, highlights the final device's dimensions. The height was obtained after a checking of the ACL femoral tunnels' diameter, usually about 8.5mm. To assure that a bigger tunnel could be used, in future tests, a 9mm diameter hole will be inserted in the final PSI model. To fit this hole, a total height of 13mm was tested, and if it folds sufficiently, this geometry is validated and can be used along the future dimensioning and designing processes [31].

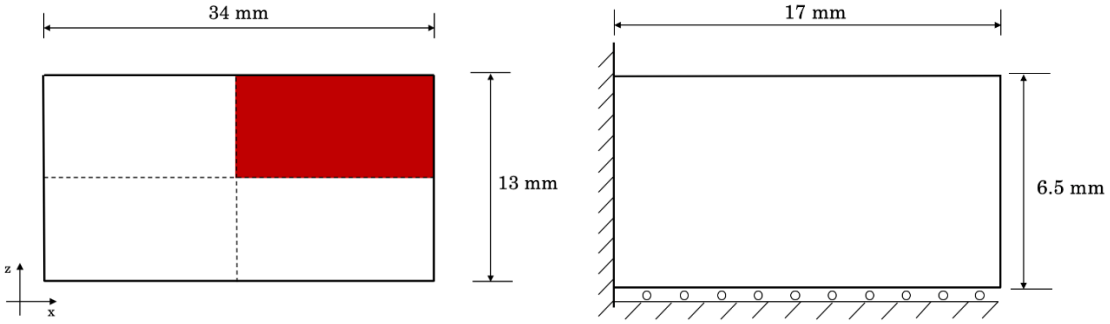


Figure 53 - Geometry's side dimensions to perform the first 3D tests.

Another important issue to justify is the use of a quarter of the entire model. Due to the model's natural symmetry along the planes Oxy and Oyz planes, (Figure 53 in l.h.s.), symmetry assumptions can be taken in order to reduce the analyzed model (reducing the computational cost of the analysis), as in Figure 53 (r.h.s) and Figure 54. A fixed plane is used as a symmetry condition, and the lower plane simply has a boundary condition of a fixed displacement along the height. With this last, it was assured that the model would not have a distortion in this direction that could affect the results. These simplifications allow the user to perform simulations with a lower number of nodes, analyzing the entities under the same conditions faster.

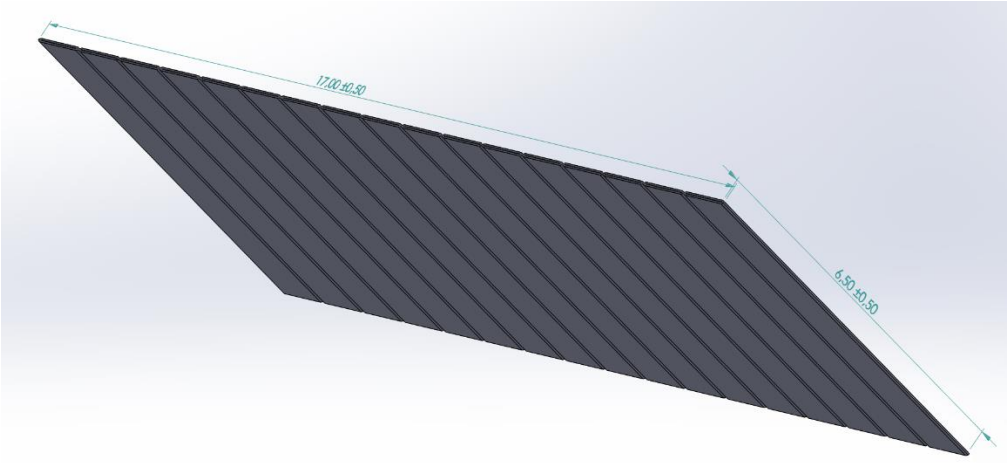


Figure 54 - 3D device modelled in SOLIDWORKS© with its dimensions.

The 3D simulations were carried out in FEMAS with a thermal gradient of 80ºC. The geometry, originally constituted by a default material, was imported from SOLIDWORKS© to FEMAP©, so it could be meshed, and afterwards to FEMAS. This process was used throughout the whole work with all the models that were designed in SOLIDWORKS© and are displayed subsequently. Another MATLAB© routine was written to automatically match the nodes to their correct material, performing the "Materials' Attribution" routine (see Appendix B), attributing the ones that were supposed to be made out of the highest TEC material to material 2 and the rest to material 1, as it is shown in Figure 55 and detailed in the MATLAB© code in Appendix B.

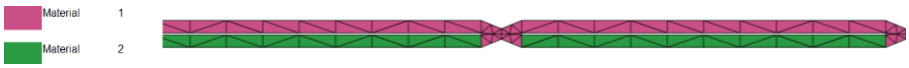


Figure 55 - Final geometry's materials after a FEM simulation with the Incremental Procedure with Materials' Attribution.

Another important computational limitation regarded the number of nodes that could be used in 3D simulations. To have sufficiently refined meshing parameters in the top/bottom geometries, needed to verify the folding mechanism, it was difficult to have a large number of elements along the height of the model, otherwise, the computational cost and time needed to carry out the 3D simulations would not be supported by the resources disposed along this work's development. The number of nodes used in this simulation was about 8500, which is supposed to be in the convergence plateau values that was not reached in Cook's Membrane - Convergence example section in 3D tests.

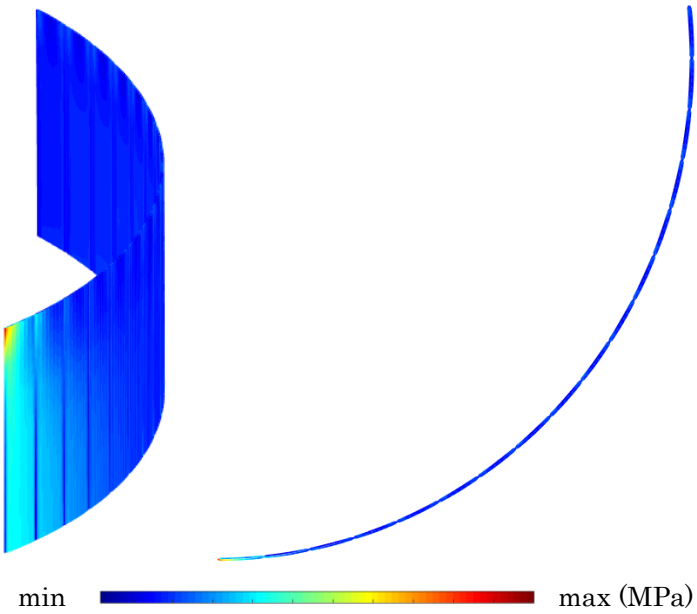


Figure 56 - 3D Effective-Stresses (Von-Mises) colormaps generated with FEMAS, in a 3D view (l.h.s) and a top view (r.h.s).

Analyzing the 3D image, on l.h.s of Figure 56 it is easy to find a peak of stress in the fixed edge. These values theoretically should be of the same order of magnitude as the ones obtained in the 2D tests, and once these values were concordant with PLA's Tensile Strength, these 3D Effective-Stresses must also accomplish this condition. This peak is due to an incorrect behavior of tetrahedral meshes under flexion loading and a sparse mesh along the height of the structure.

Figure 56 allows one to draw the conclusion that this geometry can also be used in 3D, once the results are concordant with the ones previously accomplished, with a 90º folding of the entire structure, this time with an extrusion of 6.5mm (half of the total 13mm height).

7.5 Tunnel drilling hole

After the validation of the 3D model without additional features, the first addition to the original structure was made in order to design the hole that will accommodate the drill that will perform the femoral tunnel. This hole will influence the behavior showed by the first 3D model, hence, there is a need to assess if the divide will perform the folding process correctly with this insertion.

The model designed in SOLIDWORKS© was half of the complete device due to the symmetry condition (same boundary conditions constraining the structure) along the 34mm length, as displayed in the three subsequent figures (Figures 57, 58, 59).

The dimensions used were the same as before (6.5mm height and, now, 34mm of total length, see Figure 58) and the hole dimensions are displayed in Figure 59. The hole diameter is 9mm, to suit the average femoral tunnel drilling sizes, consulted in several papers [31].

This time, because the length is now the complete length, the device should evidence a total folding of 180º.

Because of all these differences, regarding the insertion of the hole to perform the femoral tunnel, the geometry will be tested firstly under 80ºC of thermal gradient. If the folding is not complete, some changes must be performed in order to obtain the desired values. The variables that can be altered regard the thermal gradient that can still be increased until 127º (see equation (7.10)) and the TEC of both materials. This last, should only be changed once the thermal gradient of 127ºC is proven to be insufficient to fold the entire geometry.

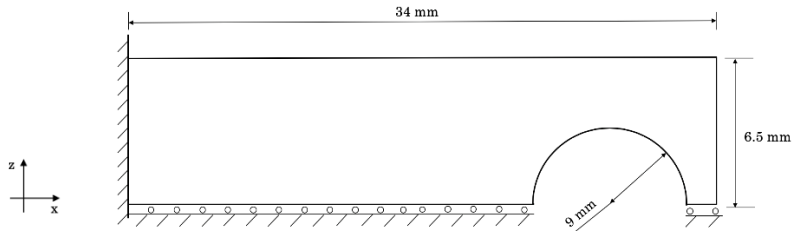


Figure 57 - 2D illustration of boundary conditions imposed to the structure to be modelled in SOLIDWORKS© and analysed in FEMAS.

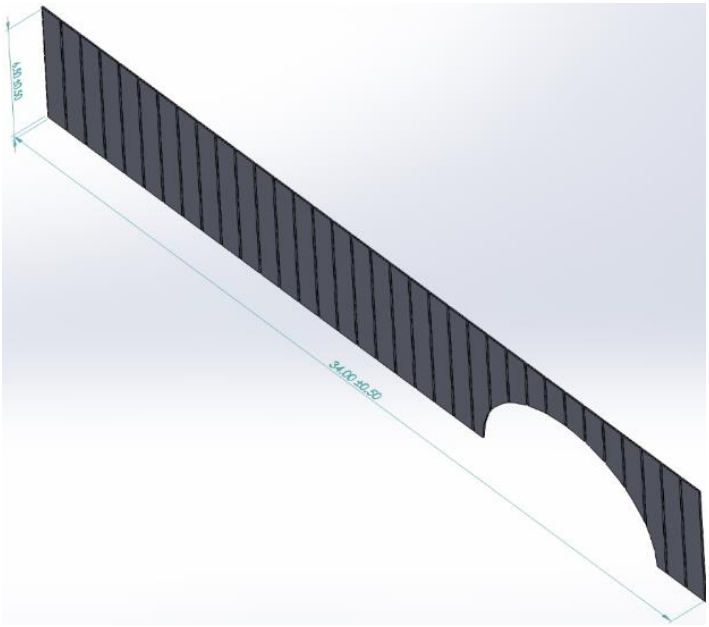


Figure 58 - 3D half device modelled in SOLIDWORKS© with is dimensions and the tunnel drilling hole.

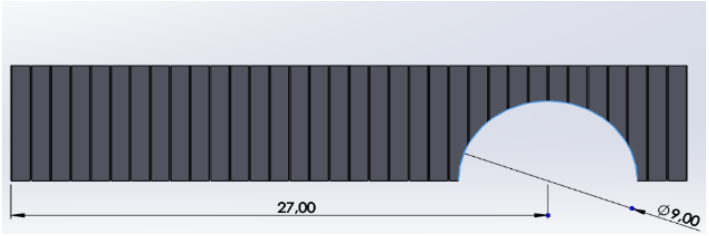


Figure 59 - tunnel drilling hole dimensions and positioning in the SOLIDWORKS© model.

The FEM analysis with the complete length and the insertion for the tunnel positioning was performed under an 80ºC thermal gradient and with the same TEC used for each material. The results are shown in Figure 60, and registered the same peak of stresses, explained before.

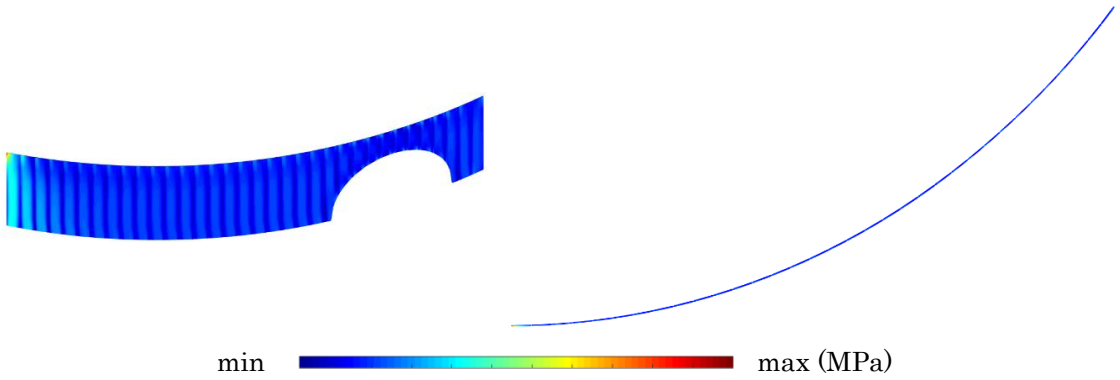


Figure 60 - Effective-Stresses (Von-Mises) colormaps generated with FEMAS, in a 3D view of the entire component with the tunnel positioning hole (l.h.s) and a top view (r.h.s), under 80ºC of temperature gradient.

As it is noticeable in Figure 60 on l.h.s, the entire model did not fold the desired amount, once this time, it was needed a 180º folding. Again, the peak of tensions was noticeable which reinforces the conclusions of a bad behaviour of tetrahedral meshes under flexion. So, under these conditions of material properties and thermal gradient, this geometry would not accomplish the folding as it should. Given these insights, it is needed a temperature gradient changing in order to successfully proceed with the device's development.

7.5.1 Temperature gradient alteration

Once the structure did not perform as desired under the previous conditions, some variables had to be changed. A testing was performed with the maximum temperature gradient of 127ºC (being the device storing temperature of -90ºC, as in equation (7.10)). If under these conditions the model did not fold in the desired manner, it meant that the materials in which

the model is being developed are not suitable for their function, hence, the difference between TEC should be increased.

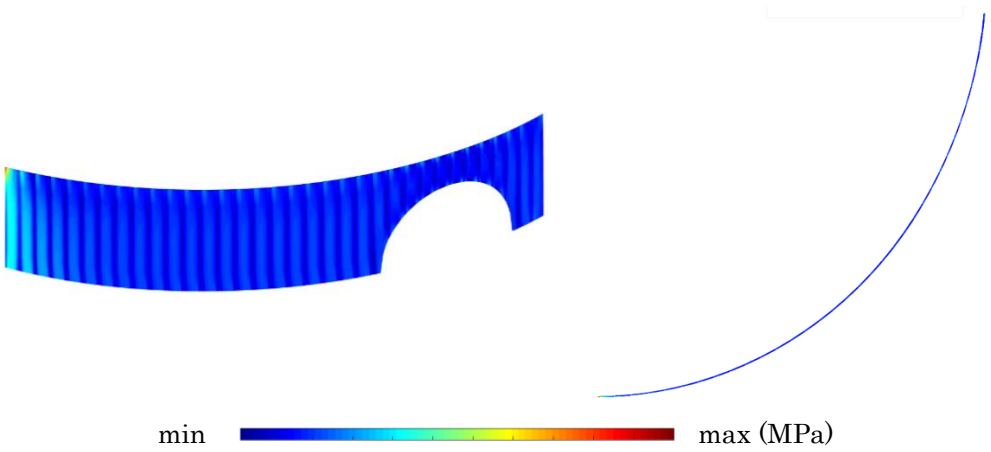


Figure 61 - Effective-Stresses (Von-Mises) colormaps generated with FEMAS, in a 3D view of the entire component with the tunnel positioning hole (l.h.s) and a top view (r.h.s), under 127ºC of temperature gradient.

The l.h.s of Figure 61, once again with the peak of stresses aforementioned, illustrates the instrument's inability to fold under a thermal gradient of 127ºC and the material properties exposed in Table 5.

As it is easy to conclude, the possibilities regarding the alteration of temperature gradient between the values established as possible to implement with the present technologies were over. In addition, the TEC difference between material 1 and 2, both PLA's, was the highest possible. Given this data, obtained with these tests, the possibilities to implement the mass-production and distribution of this devices with both refrigeration and materials current technologies had been eliminated and the next step taken was to change the TEC difference between both materials, increasing the highest TEC.

7.5.2 Thermal expansion coefficient alteration

Once the material properties of both PLA used in previous tests could not meet the requirements under a temperature gradient of 127ºC, they should be changed to a value that could accomplish the desired functions. It is important to clarify that this new material could be a non-existing material, or at least, a material that already exists with this properties' values, but, for example, is not suitable for 3D printing because of the non-thermoplastic behaviour. Thus, this next study is a theoretical approach, to quantify which are the physical and thermal properties that are needed to produce a device that can perform as intended. The 3D printing and thermoplastic behaviour of the material were not taken into account for these subsequent tests.

From this point on, the comparison of the Effective-Stresses and Effective Equivalent Strains with the values of PLA present in Table 1 were proven to be inconsequential.

All the aforementioned set the need to change a variable of the process and a trial-error method was used to obtain the desired TEC difference between material 1 and 2. The other properties should be the same as the ones presented in Table 5 with the constant increment of the Material 2 TEC, until reaching the 180º folding.

Table 6 – Materials' mechanical and thermal properties used in the tunnel drilling hole tests, first alteration of material 2's TEC.

Property	Material 1	Material 2	Unit
Young Modulus	3600	3600	MPa
Poisson's ratio	0.38	0.38	
Thermal Diffusion Coefficient	0.09	0.09	J/msK
Thermal Expansion Coefficient	41e-6 [28]	170e-6	strain/ºC

After these inputs were set to FEMAS, the FEM simulation was performed under a thermal gradient of 127ºC again, and the results are displayed in Figure 62. As before, this alteration in the thermal property of the second material was insufficient and another value should be used in order to reach the 180º folding of the entire structure.

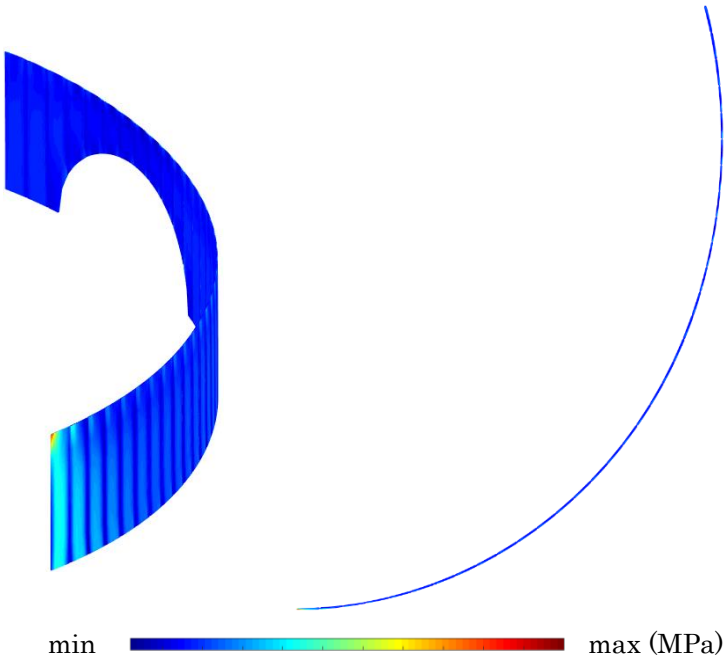


Figure 62 - Effective-Stresses (Von-Mises) colormaps generated with FEMAS, in a 3D view of the entire component with the tunnel positioning hole (l.h.s) and a top view (r.h.s), under 127ºC of temperature gradient and with material 2's TEC of 170e-6 strain/ºC.

The values were the ones previously used, with a subsequent increasing of material 2's TEC, from 170 to 250e-6 strain/ºC.

Table 7 – Materials' mechanical and thermal properties used in the tunnel drilling hole tests, second alteration of material 2's TEC.

Property	Material 1	Material 2	Unit
Young Modulus	3600	3600	MPa
Poisson's ratio	0.38	0.38	
Thermal Diffusion Coefficient	0.09	0.09	J/msK
Thermal Expansion Coefficient	41e-6 [28]	250e-6	strain/ºC

Once defined these properties in FEMAS, the simulation was carried out under a thermic gradient of 127ºC. This time it was expected the full folding of the device of 180º.

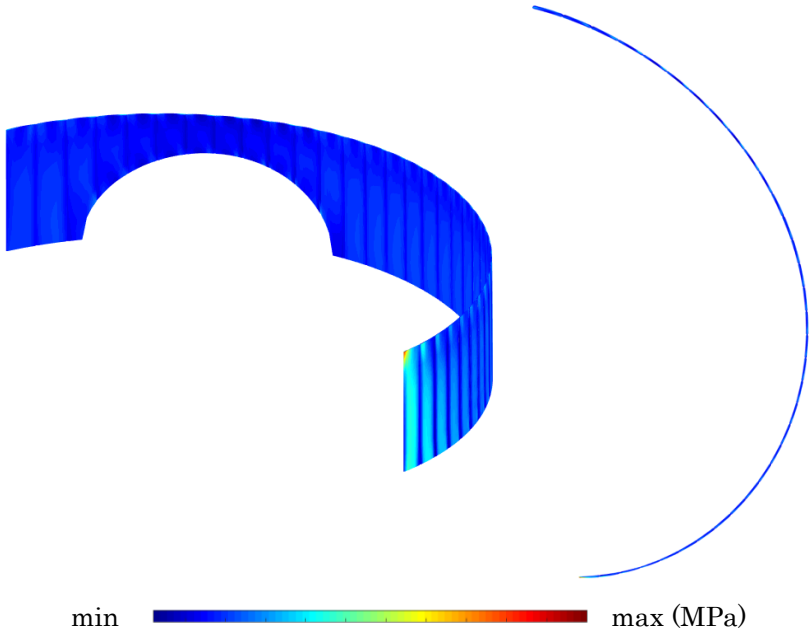


Figure 63 - Effective-Stresses (Von-Mises) colormaps generated with FEMAS, in a 3D view of the entire component with the tunnel positioning hole (l.h.s) and a top view (r.h.s), under 127ºC of temperature gradient and with material 2's TEC of 250e-6 strain/ºC.

Figure 63 shows the accomplishing of the total folding of the geometry with a temperature gradient of 127ºC and TECs of 41e-6 and 250e-6 for material 1 and 2, respectively. These are the conditions that assure the required function at this stage of the development of the PSI.

After the testing of the folding process from a "linear" geometry, to obtain insights about the behaviour of the geometries and materials used in these tests, from the small to the real-scale, as well as the comparison between the 2D and 3D models under certain conditions, the next step taken was to test the actual mechanism that the device will be exposed to, the

unfolding geometry from a "cylindrical" shape to the geometry of the femoral bone.

7.6 Unfolding process

As said and presented before, for example in Figure 54, the geometries imported to FEMAS, designed in SOLIDWORKS© and meshed in FEMAP©, were all designed with a linear shape. After finishing the folding tests of all the geometries, performed throughout this section, one more MATLAB© routine was written in order to "fold" the linear geometry before the FEM simulation, to test the unfolding of the geometries under different conditions, named "Folded Geometry" routine (consult Appendix C). It is a mathematical function that transformed the nodal coordinates (x, y, z) of the meshed solid (initially in the linear configuration) to an approximation of what can be considered a cylindrical shaped model.

This routine was programmed to obtain, in an expeditious, manner a folded geometry, once the pattern repetition and copying the geometries of thirty-four 1mm samples that constitute the entire model along a circumferential path would be a cumbersome task. The mathematical function was developed in such way that allowed the resultant geometry to fulfil the requirements of the devices that are used in orthopaedical surgical procedures with a maximum diameter of 8mm.

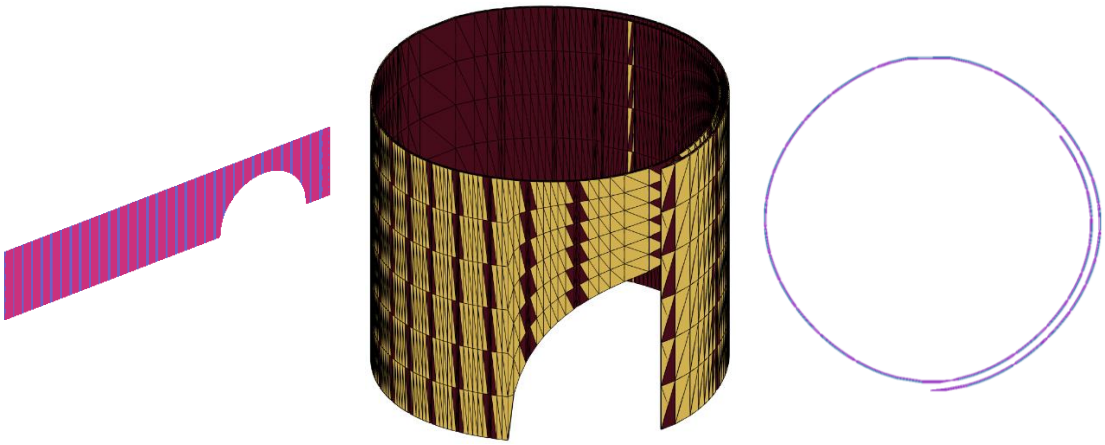


Figure 64 – Linear (l.h.s), before, and cylindrical geometry, from a 3D perspective (centre) and a top view (r.h.s), after the Folded Geometry routine that folded the device previously to the simulation.

Figure 64 shows the geometry before and after the Folded Geometry. As a mathematical approximation some elements of the meshed solid were distorted, but it was assumed that these distortions would not be enough to hinder the FEM simulations. In addition, there are some elements that are not well assigned to the correct material, due to some limitations of the

Materials' Attribution routine. It was once more assumed that these small errors would not influence significantly the results of the FEM simulations.

With the folded geometry programmed and established on FEMAS, the first test of the device's unfolding mechanism was performed. The conditions were the same as the ones that were concluded to be enough to fold the device before (shown in Table 7), except this time the starting geometry was cylindrical instead of linear. It is expected to see a folded shape close to 180º, that could adapt to the femoral geometry, as it was obtained in Figure 63.

The results are displayed in Figure 65, and show an insufficient unfolding of the device, once that would be able to adapt to the femur, which means that the TEC of material 2 should be again incremented.

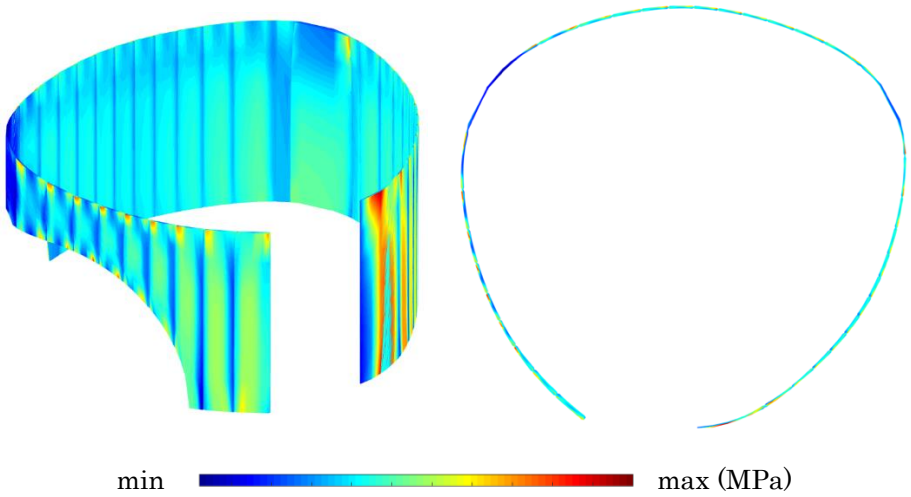


Figure 65 - Effective-Stresses (Von-Mises) colormaps generated with FEMAS, in a 3D view of the entire component with the tunnel positioning hole (l.h.s) and a top view (r.h.s), starting from a cylindrical shape, under 127ºC of temperature gradient and with material 2's TEC of 250e-6 strain/ºC.

7.6.1 Thermal expansion coefficient alteration

After the first simulation starting with the folded geometry results proved the lack of unfolding ability with a material 2's TEC of 250e-6 strain/ºC, a sequential increment of this thermal property was made in order to test again if the unfolding process could now be enough to fulfil the requirements preset.

The first try with this procedure was to use a material 2's TEC of 320e-6 strain/ºC. This time it is expected a complete unfolding of the geometry, and, once again, if it is not complete, this property needs to be incremented again.

Table 8 – Materials' mechanical and thermal properties for the unfolding test, first alteration of material 2's TEC.

Property	Material 1	Material 2	Unit
Young Modulus	3600	3600	MPa
Poisson's ratio	0.38	0.38	
Thermal Diffusion Coefficient	0.09	0.09	J/msK
Thermal Expansion Coefficient	41e-6 [28]	320e-6	strain/ºC

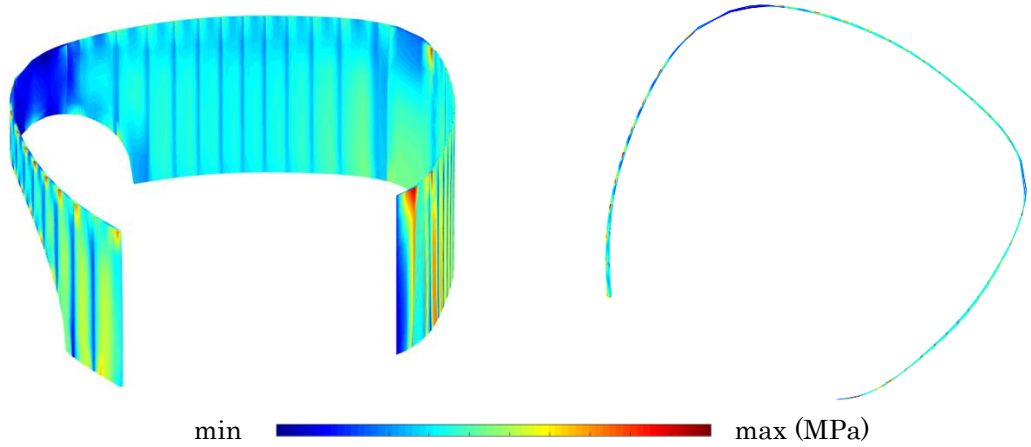


Figure 66 - Effective-Stresses (Von-Mises) colormaps generated with FEMAS, in a 3D view of the entire component with the tunnel positioning hole (l.h.s) and a top view (r.h.s), starting from a cylindrical shape, under 127ºC of temperature gradient and with material 2's TEC of 320e-6 strain/ºC.

As it is easy to conclude when analyzing the r.h.s of Figure 66 the unfolding mechanism of the model was not completed in the desired manner and a sequential increasing in the TEC of material 2 was again performed, this time for 420e-6 strain/ºC, as stated in Table 9.

Table 9 – Materials' mechanical and thermal properties for the unfolding test, second alteration of material 2's TEC.

Property	Material 1	Material 2	Unit
Young Modulus	3600	3600	MPa
Poisson's ratio	0.38	0.38	
Thermal Diffusion Coefficient	0.09	0.09	J/msK
Thermal Expansion Coefficient	41e-6 [28]	420e-6	strain/ºC

Figure 67 proves that with a TEC of material 2 of 420e-6 strain/ºC it is possible to unfold the device from a cylindrical shape into a geometry that can suit the femoral bone and its entities, with an angle close to 180º. This figure also allows one to see that with these magnitudes of TECs values, there is a distortion of the tunnel drilling hole that will be detailed further in subsequent sections.

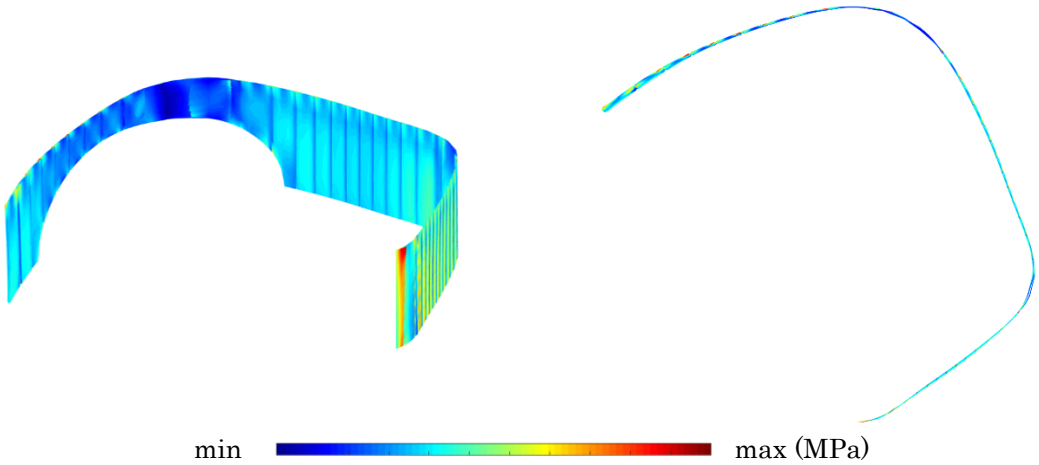


Figure 67 - Effective-Stresses (Von-Mises) colormaps generated with FEMAS, in a 3D view of the entire component with the tunnel positioning hole (l.h.s) and a top view (r.h.s), starting from a cylindrical shape, under 127ºC of temperature gradient and with material 2's TEC of 420e-6 strain/ºC.

Once analyzed Figure 67, it is possible to see an expansion registered in the drilling hole, due to the thermal expansion of the model. Because this can become a factor that undermines the device's usage effectiveness it would have to be solved in order to accomplish its designated function.

7.6.2 Ellipse shaped tunnel drilling hole

Due to the aforementioned problem showed in Figure 67 related to the expansion of the hole that should have roughly the same dimensions (accounting the needed tolerances) of the drill that will perform the femoral bone, the possibility to design the hole as an ellipse that could expand to a more circular form was tested.

The procedure to obtain the dimensions' quantification that would be used in the ellipse was a numerical and simple mathematical formulation, where a ratio (α) between the desired (Di) and the expanded diameter after the simulation (Di^*) would determine the quantification of the ellipse diameter (Df), see Figure 68.

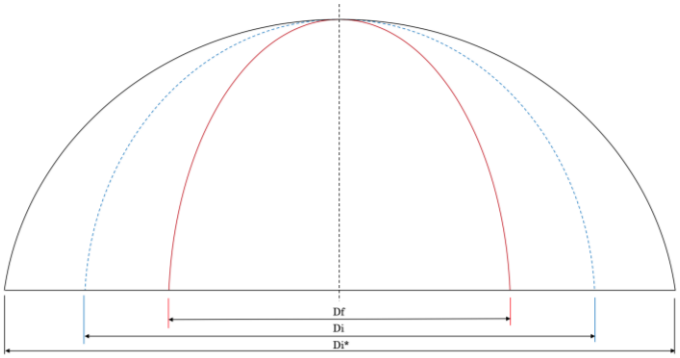


Figure 68 - Graphical illustration of the determination of ellipse diameter (Df) using the expansion of the tunnel drilling hole.

The ratio between Di and Di^* is given by:

$$\frac{Di}{Di^*} = \alpha \tag{7.12}$$

and expresses the relation between the designed hole diameter before and after the heat transfer and the expansion that happens with it. This relation was used to determine the diameter of the ellipse that will be further designed and, after the expansion, theoretically, the final diameter will be the desired Di. The quantification of the final ellipse diameter is given as follows:

$$D_f = \alpha\, D_i \tag{7.13}$$

After the simulation showed in Figure 67 the value for Di^* was determined and D_f was calculated in order to design a new model in SOLIDWORKS© and test it under the conditions previously used. After this simulation, it can be concluded, if the final diameter is the same as the previously desired, that this numerical approach can be applied and the tunnel drilling precision can be enhanced with this detail.

Table 10 – Hole's shape changing calculation values.

Di (mm)	9
Di^* (mm)	16.345
D_f (mm)	4.949

The quantification of D_f allowed the new design of the model in SOLIDWORKS©. This time the hole is designed as an ellipse and is shown in Figure 69, as well as its dimensions. The hole center point is positioned in the same place as before and it is expected to be observed an expansion of the ellipse to a more circular shape.

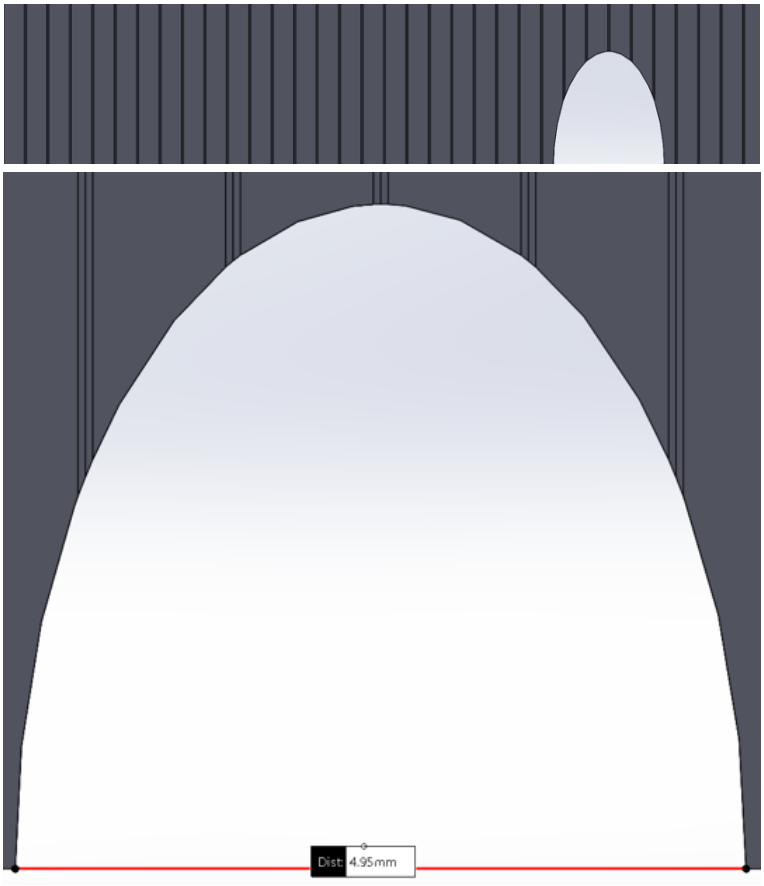


Figure 69 - 3D device modelled in SOLIDWORKS© with ellipse shaped hole positioning (above) and Df diameter dimension (below).

This model was tested under the predefined conditions displayed in Table 9 and the results are detailed in Figure 70. The unfolding mechanism remained almost the same as the one registered in Figure 67 (r.h.s) and, given this fact, it is shown that the ellipse shaped tunnel drilling hole would not comprise the results performed by the structure in what regards the unfolding process.

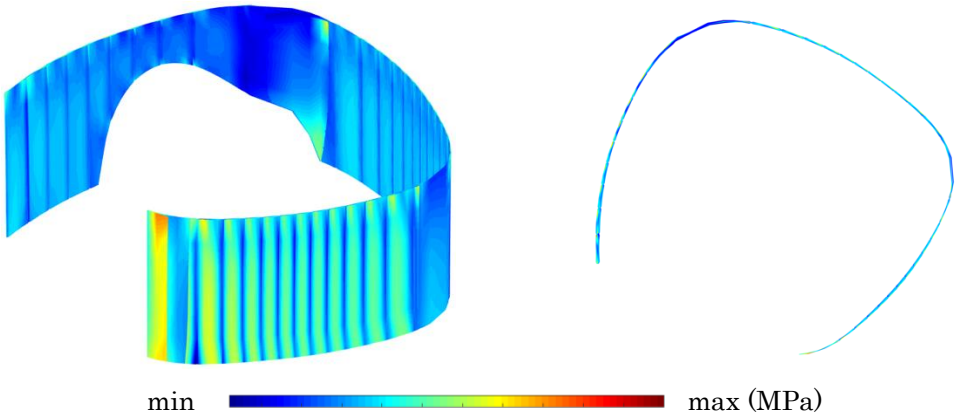


Figure 70 - Effective-Stresses (Von-Mises) colormaps generated with FEMAS, in a 3D view of the entire component with the ellipse tunnel positioning hole (l.h.s) and a top view (r.h.s), starting from a cylindrical shape, under 127ºC of temperature gradient and with material 2's TEC of 420e-6 strain/ºC.

Figure 71 shows the Effective-Stresses (Von-Mises) with the elements represented. A deformation in some elements due to the mesh distortion is related to the Folded Geometry mathematical limitations. This routine, as aforementioned, is responsible for the folded geometry previous to the FEM simulation and, because it is a mathematical approximation, it changes some of the elements' dimensions in the ending points of the folded model diameters. This elements are visibly distorted and elongated after the simulation and this is the reason of the incorrect definition of the ellipse contour, showed in Figure 70 and detailed in Figure 71. Due to this fact, the dimensions of the ellipse tunnel cannot be accurately determined but there is an obvious approximation to a circular shaped tunnel as exposed in Figure 70 and Figure 71.

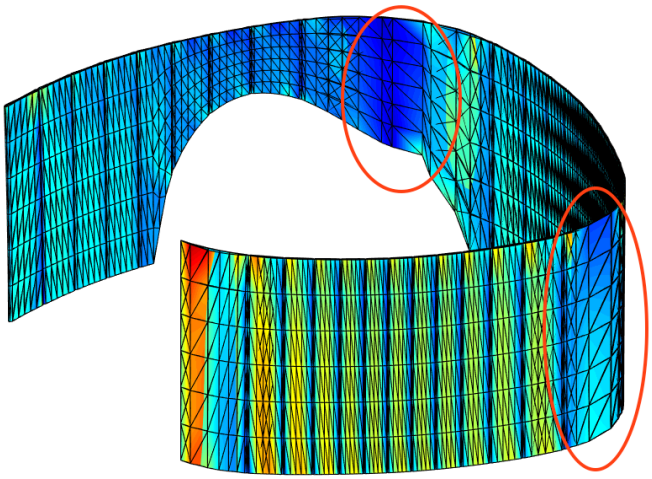


Figure 71 - Effective-Stresses (Von-Mises) colormaps of the ellipse tunnel positioning hole, shown in the l.h.s of Figure 70, with the highlighting of the distorted elements.

After measurements of the diameter of the ellipse the values were close to a circle which can be observed as well in figures Figure 70andFigure 71 and validates the approach for the ellipse tunnel drilling hole.

7.7 Drill guiding tabs

After the dimensioning of the tunnel drilling hole shaped as an ellipse another feature was added to the model. Two guiding tabs were added to the device in order to help the healthcare provider to angle the incision of the tunnel in the femoral bone. These structures had to be tested, because there was the possibility of blocking the unfolding of the device. In addition, these entities could bend with the heat transfer process and their function could be comprised.

In order to test this addition to the device, a SOLIDWORKS© model was developed with the guiding tabs and the respective distances so that the drills could be guided in between these structures and match its position with the drilling hole, as it can be seen in Figure 72. The dimensions of the proper entities were determined in a way so that they could be used as a guide to the drill and the distance between them is 9mm because this is the value that was assumed to be the diameter of this surgical instrument.



Figure 72 - 3D device modelled in SOLIDWORKS© with the ellipse shaped hole and the guiding tabs positioning (above) and their dimensions (below).

Figure 73 allows one to check that the dimensions chosen for the tabs' height is suitable to guide the drill and assist the femoral tunnel positioning.

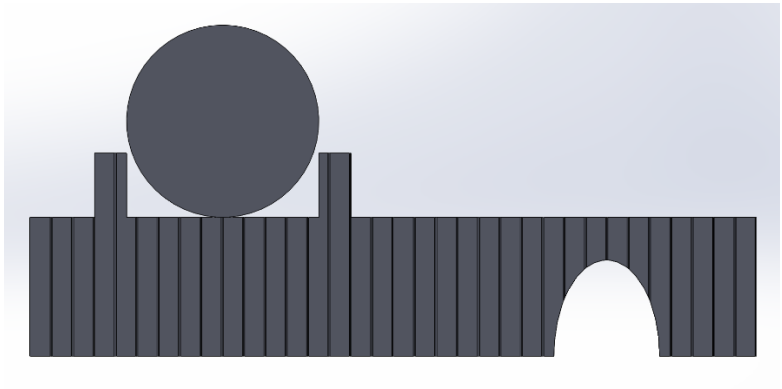


Figure 73 - Drill placement in between both guiding tabs.

It is important to state that this model is half of the whole device, but in its complete version just the upper part will have these tabs, so the symmetry is not totally true (but it will not significantly influence the results). The symmetry condition was used as before (see Figure 57) to reduce the computational cost, because a simulation with the entire model would require the double of the nodes and both hardware and software could not handle that number of nodes.

The FEM simulation was performed in FEMAS and the results assure the correct positioning of the drilling tunnel for the surgical procedure, as it is shown in Figure 74 and Figure 75. The aspects that could arm the results of the device were proven to be inaccurate and, given this insight, it is assured that this feature can be added with no drawbacks to the device, enhancing the accuracy of the tunnel positioning, contributing to the final goal of this project. The results of these tests are displayed in Figure 74.

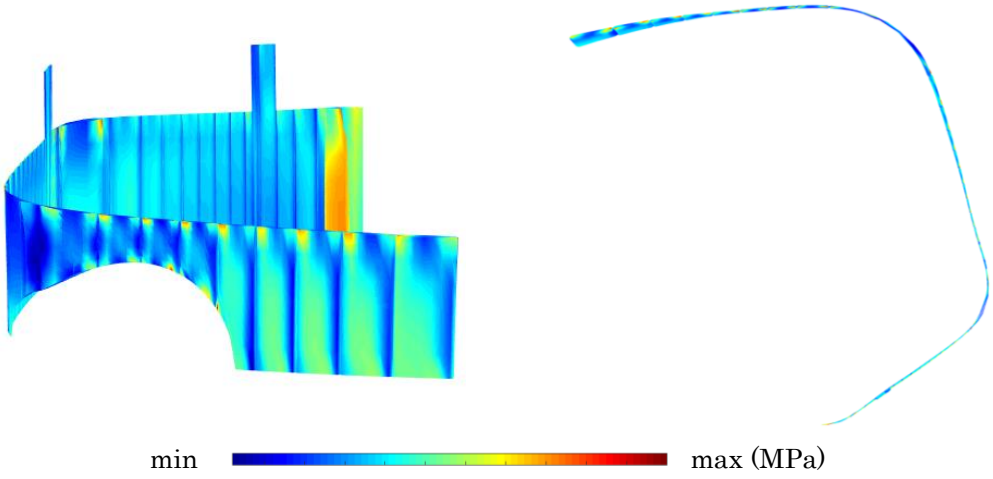


Figure 74 - Effective-Stresses (Von-Mises) colormaps generated with FEMAS, in a 3D view of the entire component with guiding tabs (l.h.s) and a top view (r.h.s), starting from a cylindrical shape, under 127ºC of temperature gradient and with material 2's TEC of 420e-6 strain/ºC.

Figure 75 exemplifies the drill's position and orientation. It is supposed to be placed in between both guiding tabs and slid into the hole throughout it is supposed to drill the femoral tunnel in its exact position, accomplishing for the tunnel positioning the accuracy increment initially intended.

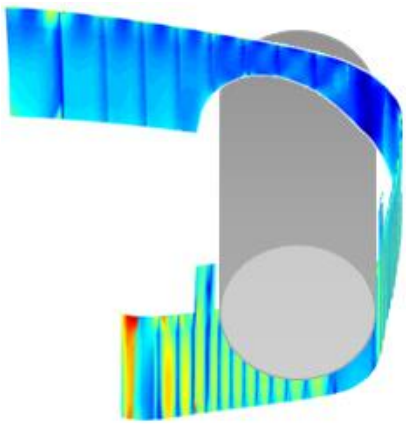


Figure 75 – Illustration of the drill axis orientation.

Once this feature was successfully added, the main objectives of this thesis are accomplished. The research, design and development of a device, fully customizable, Patient-Specific, that allows the healthcare provider an exact positioning of the femoral tunnel drilling hole in the Arthroscopic ACL reconstruction. This instrument overpassed the restrictions inherent to this surgical procedure and maintained the condition of a minimally-invasive technique, once it can be inserted in the knee through a cylindrical-shaped instrument used in these applications.

Additionally, an extra feature was studied in order to, besides the positioning of the tunnel drilling hole, allow the fixation of the device in a specific (and accurate) place along the intercondylar notch.

7.8 Position fixation tabs

Apart from the requirements that were *a priori* committed to be fulfilled, in order to enhance even more the location precision that this device helps to achieve, an extra feature was added to the final model. Two more tabs were included on the top of the model so that, after their folding (orthogonally to the folding of the model), the device could be fixed inside the knee joint.

To perform this, another material distribution was needed across both these entities to fold them in a different orientation when comparing to the rest of the device. To match the nodes of the fixation tabs in the correct manner, some alterations were made to the Material's Attribution routine, in order to change the configuration of the materials' distribution. These

alterations were put into practice in another routine, named "Additional Material's Attribution" routine, detailed in Appendix D.

The FEM analysis in FEMAS were made with a 3D model that was half of the entire device, once again. In opposition to what happened in the drill guiding feature, that was only present in the upper part of the entire model, the position fixation tabs will stay both on the upper and lower part of the model. This assumption allows the study of a total of four different fixation points (two in the half model studied) in the knee joint, which are more than sufficient to accomplish this function. Possibly, there will be no need for so many fixation points, but these tests will prove that it is structurally possible to have these entities added to the device.

The SOLIDWOROKS© model is shown in Figure 76 and it represents the positioning of these entities and their dimensions. Both these variables do not have requirements that have to be fulfilled, because they will depend on the customization of the device, once each femur has its own landmarks that can be exploited to the fixation of the device. This is a general model that just serves as insight about the possibility to use this feature in a more advanced research process.

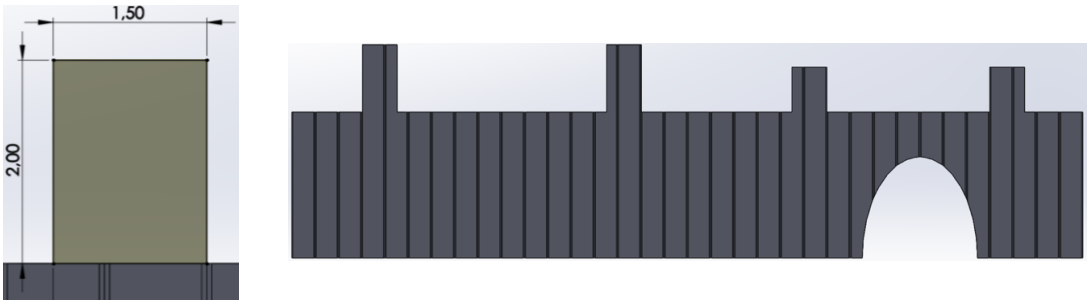


Figure 76 - 3D device modelled in SOLIDWORKS© with the ellipse shaped hole, the drill guiding tabs and the fixation tabs positioning (l.h.s) and their dimensions (r.h.s).

Once this model was designed in SOLIDWORKS© and imported in FEMAS (after being meshed on FEMAP©), the Additional Material's Attribution routine was run after the Material's Attribution was performed. This subsequent routine ensures the materials' distribution in the fixation tabs and the final result of the meshing with both materials is shown in Figure 77. Again, because this is a computational routine, there are some elements that did not have a correct attribution, but the existing errors should not influence significantly the obtained results.

As it can be seen, the fixation tabs have a configuration of an orthogonal division in half with both materials. This configuration will be tested to assess if the folding to an orthogonal position to the rest of the model will occur, using the two different materials that were found to be sufficient

to accomplish the previous requirements. If it is proven insufficient for its function another different material will be needed to construct these entities.

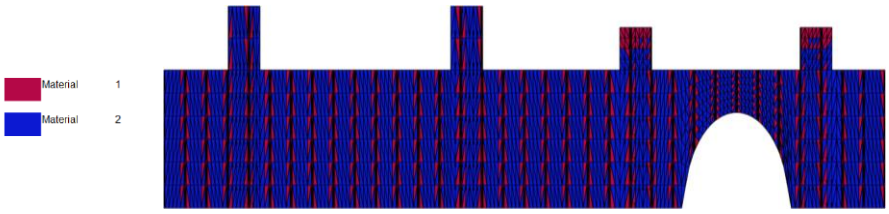


Figure 77 - Linear geometry with the fixation tabs with elements of both materials in FEMAS.

The properties that were used are the same as the ones displayed in Table 9, on page 97, and the results of the FEM analysis are presented in Figure 78. This geometry and material distribution, at least with this couple of materials was not enough to accomplish the perpendicular folding of the device in the desired amount.

Given that this was an additional study, there was not enough time to thoroughly test some variables that could have been important for optimizing this development. This feature needed a more exhaustive research about different constructive solutions to enhance the folding ability. An exploitation of a possible carving of these tabs (orthogonal to the performed carves in the rest of the model) would take an additional time (which was not available), however, it would lead useful indications regarding material properties that could be used in these tabs.

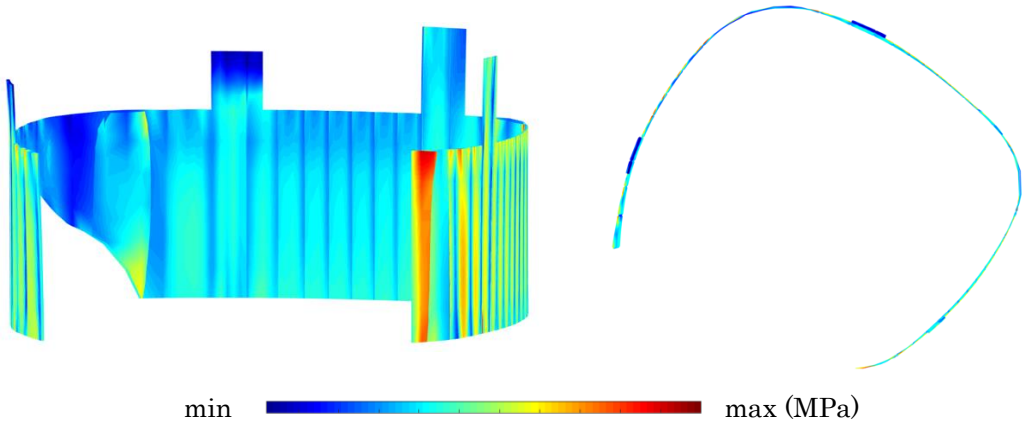


Figure 78 - Effective-Stresses (Von-Mises) colormaps generated with FEMAS, in a 3D view of the entire component with guiding and fixation tabs (l.h.s) and a top view (r.h.s), starting from a cylindrical shape, under 127ºC of temperature gradient and with material 2's TEC of 420e-6 strain/ºC.

Once the geometry changing was not possible, the solution taken was to add a new material, a third material (named material 3) that would have a higher TEC compared to material 2. The FEMAS model had now the

configuration showed in Figure 79. The procedure was the same as before, with the determination of the folded geometry being provided by its routine and, after that the model was tested under a thermal gradient of 127ºC. The TEC's increments were performed sequentially and tested individually.

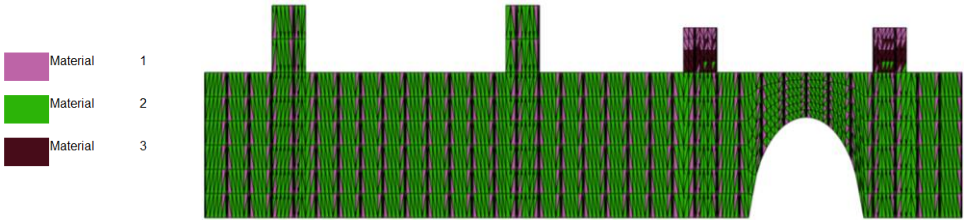


Figure 79 - Material distribution illustration with the three different materials used in the device, in the linear configuration.

The first FEM results with this third material that are worth of mention were obtained with the material properties showed in the following table. The materials 1 and 2 properties were maintained as the ones showed in Table 9. An important aspect that has to be mentioned, is that the first satisfactory results only started to be generated with values of material 3's TEC with an increment over a hundred times compared to material 2's. This was not expected previously, but the impossibility to test and dimension a different geometry was really an obstacle that only was overcame with this approach of thermal properties changing in the new material.

Table 11 - Materials' mechanical and thermal properties for the fixation tabs test, first satisfactory alteration of material 3's TEC.

Property	**Material 1**	**Material 2**	**Material 3**	**Unit**
Young Modulus	3600	3600	3600	MPa
Poisson's ratio	0.38	0.38	0.38	
Thermal Diffusion Coef.	0.09	0.09	0.09	J/msK
Thermal Expansion Coef.	41e-6 [28]	420e-6	50e-3	strain/ºC

The results are displayed in Figure 80. Because of the TEC's increment, the stresses along the entire model could not be differentiated from one and other, given the fact that the values measured in the material 3's area were almost a thousand times higher. With these values, FEMAS could generate an accurate Effective-Stresses (Von Mises) color-map, but the values along the core device were assumed to be close to zero once they were so low compared to the registered in the material 3's areas. With this, it was decided to present the results in a single color.

The folding of the entities in study throughout this section started to seem close to what was expected, but still was not in the desired amount.

Other trials were set up in order to accomplish the function of the fixation tabs.

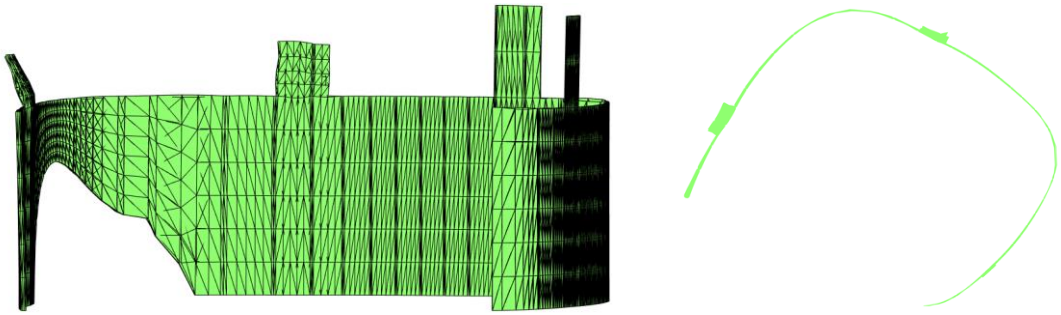


Figure 80 – Geometry generated with FEMAS, in a 3D view of the entire component with guiding and fixation tabs (l.h.s) and a top view (r.h.s), starting from a cylindrical shape, under 127ºC of temperature gradient and with material 3's TEC of 50e-3 strain/ºC.

After some other attempts in order to reach an ideal quantification of the thermal properties of material 3, the final values that were set to fulfill the requirements of this designated function were the ones presented in Table 12, with a final TEC for material 3 of 100e-3 strain/ºC.

Table 12 - Materials' mechanical and thermal properties for the fixation tabs test, final value of material 3's TEC.

Property	**Material 1**	**Material 2**	**Material 3**	**Unit**
Young Modulus	3600	3600	3600	MPa
Poisson's ratio	0.38	0.38	0.38	
Thermal Diffusion Coef.	0.09	0.09	0.09	J/msK
Thermal Expansion Coef.	41e-6 [28]	420e-6	100e-3	strain/ºC

The results are showed in Figure 81 and it is visible that the folding of the entities is now sufficient to embrace the intercondylar notch and fix the position wherever is needed to provide the surgeon with a more accurate guidance and assistance when using this device in the ACL arthroscopic reconstruction.

With this feature assuring the fixation of the device, the additional objective set to develop and study these entities is accomplished and the structural tests of the device are now all performed, being this research and development phase fully finished.

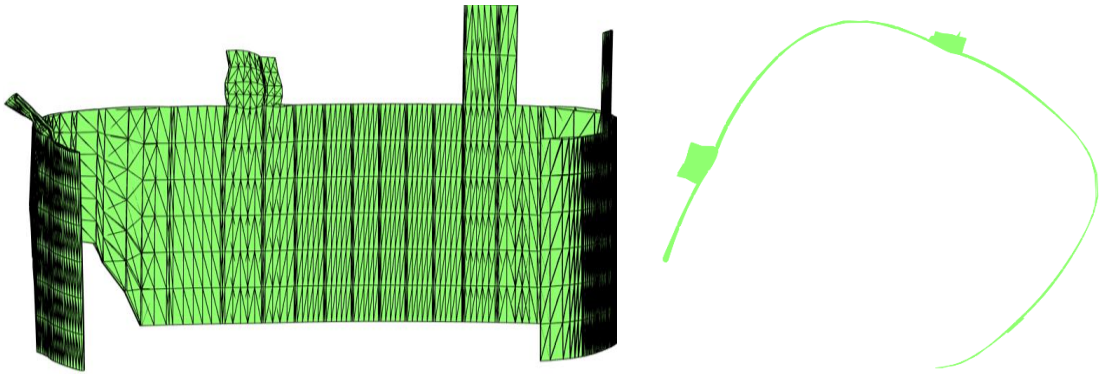


Figure 81 – Geometry generated with FEMAS, in a 3D view of the entire component with guiding and fixation tabs (l.h.s) and a top view (r.h.s), starting from a cylindrical shape, under 127ºC of temperature gradient and with material 3's TEC of 100e-3 strain/ºC.

After all these eight subsections, a comprehensive study of the PSI development was presented, from its concept to the structural tests performed so that a final model was fully designed and scrutinized. From a small to a real-scale, from 2D to 3D, the core of the device was tested thoroughly so that it could fulfill the requirements of the customization and shape changing ability, as well as the positioning of the tunnel drilling hole in a given point. Thereafter, the angle of the incision was tested and assessed with the drill guiding tabs added to the model and, with these, the healthcare provider would be capable to perform the drilling through an exact positioning and angle, which makes it entirely optimized and the main objectives that led this thesis completed.

Additionally, these position fixation tabs were studied so that the positioning of the device could be made in a previously checked point which could enhance even more the incision precision, being an important additional feature added to the already almost completed device.

After all the research and development detailed throughout this chapter a 3D printing of the final model, it was produced with FDM as a proof of concept and will be subsequently elaborated.

7.9 Final device's 3D printing

In addition to what was previously presented in this chapter regarding the whole development process, a physical model was produced using a Fused Deposition Modelling technique with the collaboration of the Computational Mechanics Research Laboratory CMech-Lab.

An entire model was designed in SOLIDWORKS©, this time with no symmetry conditions, detailed in Figure 82. This model was the linear geometry of the fully developed device and this 3D printing test would be used

as a proof of concept for a total comprehension of the different principles on which this thesis is based on.

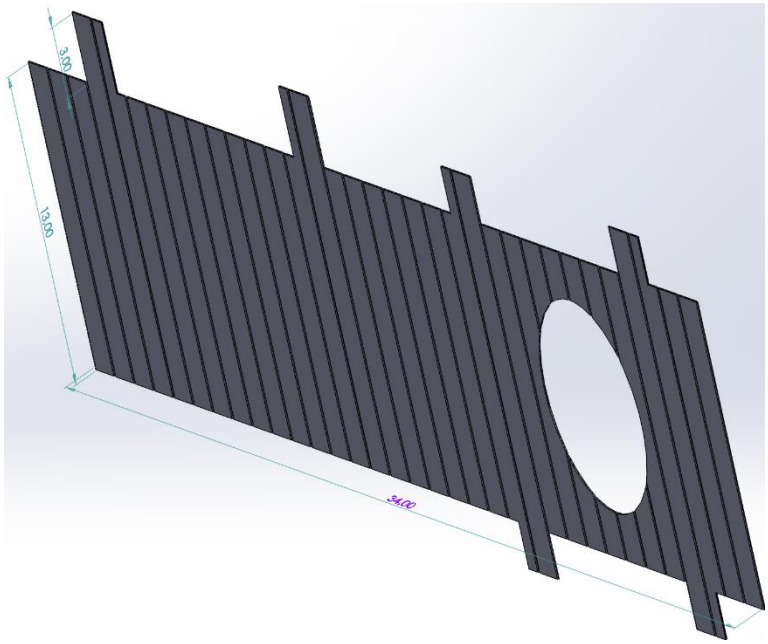


Figure 82 - SOLIWORKS© final model previous to the 3D printing.

This 3D model was then exported to the .STL extension so it could be read by the SLIC3R Software, which is an opensource and free software that uses a slicing engine for 3D printers generating a G-code from 3D CAD files. Once finished, an appropriate G-code file for the production of the 3D modelled part or object is sent to the 3D printer for the part's physical manufacturing [32].

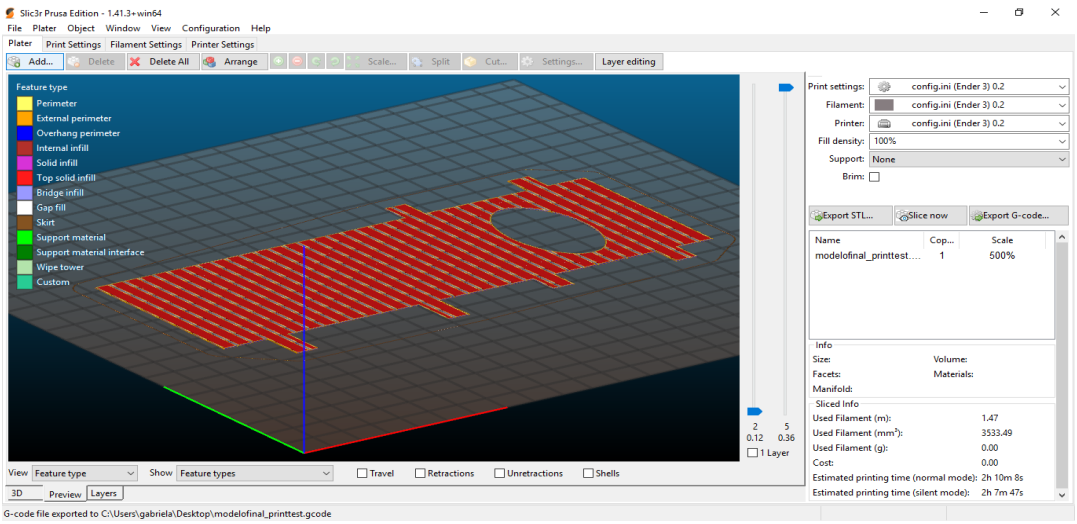


Figure 83 - Slic3r software interface with the final model before printing.

The 3D printing of this kind of geometries, with small dimensions is not possible using the technologies at disposable in CMECH-Lab, so the

dimensions had to be scaled up to five times their values and there were some complications regarding the void present in the geometries developed in section 7.3. This void was detected by the software as an overhang perimeter, represented in blue in Figure 84 (i.e., Slic3r has detected the absence of material in those places) but it is not noticeable in the physical model once the width is very small. This kind of specifications were set with the collaborators of CMech-Lab, as well as the parameters displayed in Table 13. As stated in Chapter 4, the parameters are really important in what concerns about the final quality of the device, so the help collaboration of the CMech-Lab collaborators was key in this phase of the researching process.

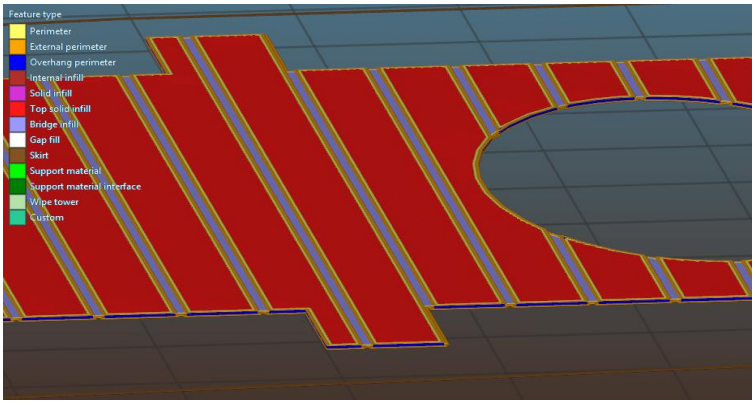


Figure 84 - Slic3r detailed legend of the model's different entities

Table 13 - 3D printing parameters for the printing of the final model.

Layer Settings		
Designation	**Value**	**Units**
Layer height	0.08	mm
1st layer height	0.12	mm
Perimeters	2	
Solid layers (top and bottom)	2	
Infill		
Designation	**Value/Name**	**Units**
Fill density	100	%
Fill angle	45	º
Fill pattern	Rectilinear	
Supports and Cooling		
Designation	**Yes/No**	**Units**
Supports	No	
Cooling	No	
Temperatures		
Designation	**Value**	**Units**
Extruder (all layers)	200	ºC
Bed (all layers)	60	ºC
Filament		
Designation	**Value/Name**	**Units**
Diameter	1.75	mm
Material	PLA [33]	
Nozzle		
Designation	**Value**	**Units**
Diameter	0.2	mm

After approximately three hours, the final device was printed, with dimensions five times higher than the real ones and the final result can be seen in Figure 85.

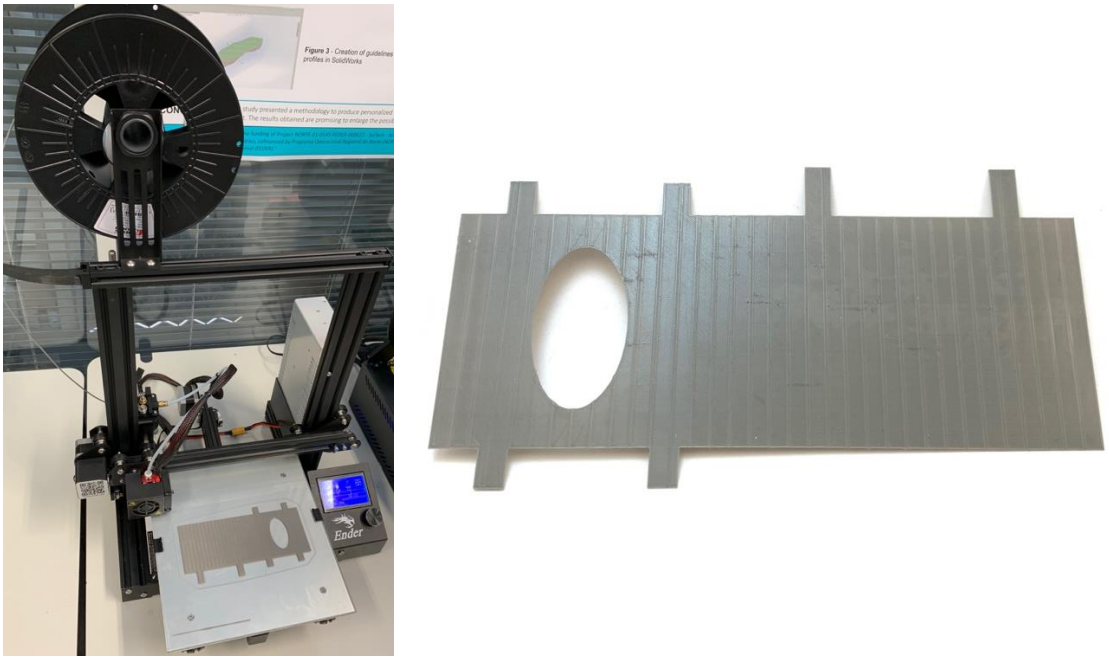


Figure 85 - Printed part on 3D printer immediately after the processing (l.h.s) and detailed image (r.h.s).

It is not, obviously, the finalized model, but, as a prototype, it allows one to check the features and their possible functions and defects that can be detected much straightforwardly when a physical model is at disposal.

Given that all the objectives were accomplished, even the additional ones, a final solution was reached accomplishing all the requirements that were previously gathered and, in the next chapter, the conclusions and the future works that will be needed will be described.

8. Conclusions

8.1 Final Remarks

As conclusion, the main objectives established to this work were accomplished with the structural analysis and study of a PSI that guides and assists the knee arthroscopy. After all the structural tests performed and product specifications defined, additional features were added to the designed model for the sake of a better accuracy in its positioning inside the knee joint. Another extra task performed was its 3D printing to better understand possible defects and changes that could be scrutinized from then on.

Previously to the study that was detailed throughout the PSI development chapter, some assumptions and properties (such as the TECs and the thermal gradient) were continually changed in accordance with the tests' results and the structural analysis.

First of all, some 2D small-scale tests were performed to obtain insights about the materials distribution across the samples and different geometries were considered in order to check which configuration would raise the deformation rates registered.

After that, the width of the model was firstly decreased, because it was concluded to be overly high to perform the desired folding mechanism. This was key to the development of the research process. Notice that if the geometry variation (with temperature) was not considered, the device would not accomplish its functions. This decreasing of width enhanced the device's folding ability after some 2D and 3D real-scale tests.

Thereafter, several features were studied and added to the model after the changing of the variables that determine the process. The tunnel drilling hole was firstly added to the model, so that the tunnel positioning could be determined and accurately placed in femur and, afterwards, the unfolding process was assessed and thoroughly studied with the set of the final material properties (concluded to be different from PLA's) that were used in the production of the device. Another aspect important for the tunnel drilling was the addition of the drill guiding tabs that could help the healthcare provider to set the angle for the incision, which makes its performance fully optimized to decrease ligament malfunction after surgery.

Once all the requirements were completed, a solution for the device's positioning fixation on the knee joint was studied, so that it would not move along the intercondylar notch and harm the tunnel drilling. This study was not exhaustive due to lack of time to test different geometries and variables,

but a final solution was reached, even though it was not the most optimized one.

Another additional study was the model's 3D printing, to obtain a prototype as a proof of concept that could help to understand the design and the functions that this device can comply.

Not all the work was performed with the best technologies and the most accurate computational tools, due to, mostly, the limitation of computational power at disposable. For example, the low number of nodes of all analyzed models and the meshing methods that could have been more accurate (with, for instance, more nodes per element, or different element types), impaired the obtained final results. An important factor that affected this work was, also, the formulation used to perform the FEM with the large deformations' theory. This formulation, programmed in MATLAB© only updated the displacement fields along the incremental procedure and, because of this, the results were not completed to perform a thorough structural analysis. The lack of time to study different (better) geometries, apart from the materials, aiming a more functional final model was also a limitation, as well as the lack of existent materials that still cannot cope with this project's specifications.

To summarize, this was a first approach for the development of this PSI and it possesses relevant documentation regarding the materials and geometries that can lead to a final device that guides and assists the knee arthroscopy. In order take advantage of this thesis' insights, some future works have to be performed.

8.2 Future works

For a further development of this PSI it would be interesting to have a better understanding of the structural and thermal properties of the device, with the inclusion of new FEM formulations on the analysis, such as, for instance, the inclusion of large deformations theory, which would allow more accurate results, or elastoplastic formulations for PLA to obtain the material's non-linear response. Different numerical tools, as Meshless Methods, which allow better results for complex geometries, with a lower number of nodes, decreasing the computational cost and enabling a more thorough analysis of different variables that have their stake on this product development.

Another aspect that would be helpful as future work is a possible geometrical optimization of the device, which will diminish the reliance on the numerical and computational tools, as well as a supplemental investigation about PLA and other biocompatible materials and their properties, that can accomplish the requirements in a more accurate manner.

9. Bibliography

1. H.Jedda, S.B.A., F. Sakli, *The effect of cyclic loading on the mechanical properties of artificial ligaments.* 2010.
2. Orchard, B.M.J.O.J., *Systematic Review: Annual Incidence of ACL injury and Surgery in Various Populations.* Sports Medicine, 2012.
3. Care, S.H. [cited 2019; Available from: https://stanfordhealthcare.org/medical-conditions/bones-joints-and-muscles/knee-ligament-injury/types.html.
4. Cetin Aka, G.B., *Production of Novel Textile-Based Artificial Anterior Cruciate Ligament.* 2016.
5. Leslie S. Beasley, D.E.W., Armando F. Vidal, Anikar Chhabra, Andrea S. Herzka, Matthew T. Feng, and Robin V. West, *Anterior Cruciate Ligament Reconstruction: A Literature Review of the Anatomy, Biomechanics, Surgical Considerations, and Clinical Outcomes.* 2005.
6. Faizal Rayan, et al., *Review of evolution of tunnel position in anterior cruciate ligament reconstruction.* 2015.
7. Turley, K., L.R. Watson, and T.N. Joseph. *Knee Ligament Repair*. Available from: https://www.urmc.rochester.edu/encyclopedia/content.aspx?contenttypeid=92&contentid=p07675.
8. Eleonor Svantesson, E.A.-G., Olufemi R. Ayeni, Volker Musahl, Ramón Cugat, Jón Karlsson, Kristian Samuelsson, *Future Perspectives of Anterior Cruciate Ligament Reconstruction.* 2017.
9. Reddy, S. *Single bundle vs Double bundle ACL surgery*. 2018; Available from: https://www.healthclues.net/blog/en/single-bundle-vs-double-bundle-acl-surgery/.
10. Lionberger, D.R., C.L. Crocker, and V. Chen, *Patient Specific Instrumentation.* The Journal of Arthroplasty, 2014.
11. Tianwu Chen, J.J., Shiyi Chen, *Status and headway of the clinical application of artificial ligaments.* 2014.
12. MarioFerretti, et al., *Osseous Landmarks of the Femoral Attachment of the Anterior Cruciate Ligament: An Anatomic Study.* 2007.
13. Marc Behl, A.L., *Shape-memory polymers.* Materials Today, 2007.
14. S. Strandman, X.X.Z., *Biodegradable shape-memory polymers for biomedical applications.* 2015.
15. Shady Farah, D.G.A., Robert Langer, *Physical and mechanical properties of PLA, and their functions in widespread applications — A comprehensive review.* 2016.
16. Yuval Ramot, M.H.-Z., Abraham J. Domb, Abraham Nyska, *Biocompatibility and safety of PLA and its copolymers.* 2016.
17. J. Xu and J. Song, *Polylactic acid (PLA)-based shape-memory materials for biomedical applications.* 2015.
18. Ngo, T.D., et al., *Additive manufacturing (3D printing): A review of materials, methods, applications and challenges.* 2018.

19. Agarwala, M.K., et al., *Structural quality of parts processed by fused deposition.* Rapid Prototyping Journal, 1996. **2**: p. 4-19.
20. 2018; Available from: https://blog.prusaprinters.org/everything-about-nozzles-with-a-different-diameter/.
21. Mamoru Mitsuishi, J.C., Paulo Bártolo, Dirk Friedrich, Albert J. Shih, Kamlakar Rajurkar, Naohiko Sugita, Kanako Harada, *Biomanufacturing.* CIRP Annals - Manufacturing Technology, 2013.
22. David R. Lionberger, M., Catherine L. Crocker, MPH, Vincent Chen, PhD, *Patient Specific Instrumentation.* The Journal of Arthroplasty, 2014.
23. Gareth G. Jones, K.L., S. Clarke, R. Collins, M. Jaere, S. Harris, J. P. Cobb, *Do patient-specific instruments (PSI) for UKA allow non-expert surgeons to achieve the same saw cut accuracy as expert surgeons?* 2018.
24. Liu, G.R. and S.S. Quek, *The Finite Element Method: A practical course*. 2003: Butterworth-Heinemann.
25. Belinha, J. *Computational Mechanics Research Laboratory*. Available from: https://cmech.webs.com/.
26. Cook, R., *Improved two-dimensional finite element.* Journal of the structural Division, 1974.
27. *Polylactide / Polylactic acid (General purpose)*. 2018: CES Edupack.
28. SD3D. *SD3D Portfolio*. 2019; Available from: https://www.sd3d.com/portfolio/pla/.
29. *Deformation Theory*. 2019; Available from: https://en.wikipedia.org/wiki/Deformation_theory.
30. *MedicalEXPO - O salão online de equipamentos médicos*. 2019; Available from: http://www.medicalexpo.com/pt/fabricante-medico/freezer-hospital-27928.html.
31. Crespo, B., et al., *Measurements of bone tunnel size in anterior cruciate ligament reconstruction: 2D versus 3D computed tomography model.* Journal of Experimental Orthopaedics, 2014.
32. *Slic3r Discription*. 2018; Available from: https://en.wikipedia.org/wiki/Slic3r.
33. FormFutura, *Technical Data Sheet: Premium PLA*. 2019: FormFutura.

Appendix

A. Incremental Procedure MATLAB© routine code

```
% this rotine divides the thermic load in N increments, and then aplies
% them iteratively

% number of increments:
n_incr = 10;

% read the ess_bound_file_h
cd data_val
load('ess_bound_file_h.mat','id_ess','vn_ess')
cd ..

% divide the imposition by n_incr
num_x = length( vn_ess );
temp_0 = 37;
temp_r = 127;

for ii = 1:num_x
    vn_ess(4,ii) = ( temp_r * vn_ess(4,ii)/temp_0 ) / n_incr;
    vn_ess(9,ii) = ( temp_r * vn_ess(9,ii)/temp_0 ) / n_incr;
end

% save the file again
cd data_val
save('ess_bound_file_h.mat','id_ess','vn_ess')
cd ..

for ii = 1:n_incr

    save('ii.mat','ii')

    % run the pre-processing
    fem_analy_pre_pro

    % run the thermo-mechanical model
    fem_analy_st_ht

    load('ii.mat','ii')

    % rename the results file (excel and mat)
    file_num = ii+10000;
    ii

    % file name: 'femas' + 'file_num' + '.mat'
    str_file_name(1,1:5) = 'femas';
    str_file_name(1,6:10) = num2str(10000+file_num);
    str_file_name(1,11:14) = '.mat';
    cd data_val
    movefile('femas10001.mat',str_file_name)
    cd ..

    % Construction of the excel file:
    % file name: 'femas' + 'file_num' + '.xlsx'
    str_file_name(1,1:5) = 'femas';
    str_file_name(1,6:10) = num2str(10000+file_num);
    str_file_name(1,11:15) = '.xlsx';
    cd data_val
    movefile('femas10001.xlsx',str_file_name)
    cd ..

    % Loading the displ_v_file.mat file
    cd data_val
    load('displ_v_file.mat','num_x','def_theory','displ_v')
    cd ..

    % load the final_mesh_file
    cd data_val
    load('final_mesh_file.mat', 'num_x', 'x_nod', 'x_val', 'num_e', 'e_nod', 'e_are', 'e_val')
    cd ..

    % update the nodal mesh
    for jj = 1:num_x
        if ( def_theory == 3 || def_theory == 4 )
            x_nod(1,jj) = x_nod(1,jj) + displ_v(2*jj-1,1);
            x_nod(2,jj) = x_nod(2,jj) + displ_v(2*jj-0,1);
        elseif ( def_theory == 8 )
            x_nod(1,jj) = x_nod(1,jj) + displ_v(3*jj-2,1);
            x_nod(2,jj) = x_nod(2,jj) + displ_v(3*jj-1,1);
            x_nod(3,jj) = x_nod(3,jj) + displ_v(3*jj-0,1);
        end
    end

    % save the final_mesh_file
    cd data_val
    save('final_mesh_file.mat', 'num_x', 'x_nod', 'x_val', 'num_e', 'e_nod', 'e_are', 'e_val')
    cd ..

end
```

B. Materials' Attribution MATLAB© routine code

```
% this routine matches a certain group of nodes to its material and patch

clear all
close all

% load:
load('final_mesh_file.mat')

% load structure file
load('mater_struct_file.mat')
n_pat = 2;
n_mat = 2;
mater_struct_array(1,1) = n_pat; % this indicates how many patches there are..
mater_struct_array(1,4) = n_mat; % this indicates how many materials there are..
mater_struct_array(1,11) = 8; % this indicates that it is a 3D study
mater_material_array = zeros(n_mat,20,3); % this erases all the material properties

n_rep = 34; % number of block repetitions
x0 = 0;
y0 = 0;
z0 = 0;

x1 = 0.05; % begining of material 2
x2 = 0.90; % length of material 2
h = 0.03; % thickness of material 2

% Loop over all nodes
for ii = 1:num_x

    x_ii = x_nod(1,ii);
    y_ii = x_nod(2,ii);
    z_ii = x_nod(3,ii);

    for jj = 1:n_rep

       x0_jj =  x0     + ( x1 + x2 + x1 ) * (jj-1);
       x1_jj =  x1     + ( x1 + x2 + x1 ) * (jj-1);
       x2_jj = (x1+x2) + ( x1 + x2 + x1 ) * (jj-1);
       x3_jj =  x1     + (5/6)* x2 + ( x1 + x2 + x1 ) * (jj-1);

       x0_aa =  x0_jj     + ( x1_jj + x2_jj + x1_jj ) * (jj);
       x1_aa =  x1_jj     + ( x1_jj + x2_jj + x1_jj ) * (jj);
       x2_aa = (x1_jj + x2_jj) + ( x1_jj + x2_jj + x1_jj ) * (jj);

       if ( ( ( x_ii > x1_jj + 1e-6 ) && ( x_ii < x2_jj - 1e-6 )...
          || (x_ii == 0.95)) && ( ( y_ii < 0 + 1e-6 ) && ...
          ( y_ii > 0 - 1e-6 ) || ( y_ii < 0.03 + 1e-6 ) && ...
          ( y_ii > 0.03 - 1e-6 ) ) )
           x_val(1,ii) = 2; % it becomes patch 2
           x_val(4,ii) = 2; % it becomes material 2
       end

    end

end

% Loop over all elements
for ii = 1:num_e

    for jj = 1:3
        id_nod = e_nod(jj,ii);
        e_val(1,ii) = x_val(1,id_nod); % patch of node id_nod
        e_val(4,ii) = x_val(4,id_nod); % material of node id_nod
    end
end

save('mater_struct_file.mat', 'mater_struct_array');
save('mater_material_file.mat', 'mater_material_array');
save('final_mesh_file.mat', 'e_are', 'e_nod', 'e_val', 'num_e', 'num_x', 'x_nod', 'x_val');
```

C. Folded Geometry MATLAB© routine code

```
% this routine changes the initial mesh (only in the Oxy plane) to a clothoid
% in the Oxyz space

% read the final_mesh_file
load('final_mesh_file.mat')

R1 = 4; % radious
s1 = pi*R1; % arc-length

R2 = 3.9;
s2 = pi*R2;

R3 = 3.8;
s3 = pi*R3;
max_length = max(x_nod(1,:));

x_nod_new = 0*x_nod;

for ii = 1:num_x

    x_ii = x_nod(1,ii);
    y_ii = x_nod(2,ii);
    z_ii = x_nod(3,ii);

    if ( x_ii <= s1 )

        x_aux = x_ii-0;

        R1a = R1 - y_ii;
        s1a = pi*R1a;

        x_aux_2 = x_aux * s1a/s1;

        param = 1/10*0.15; %mesh displacements parameters
        exp_n = 0.01;

        if x_aux_2 ~= 0

            term_1 = cos(pi*x_aux_2/s1a); %avoiding the generation of complex numbers

            if term_1 < 0
                term_1 = abs(term_1);
                term_1 = -(term_1)^exp_n;
            else
                term_1 = term_1^exp_n;
            end
            x_aux_2 = -param*term_1 + x_aux_2;

            term_2 = sin(pi*x_aux_2/s1a); %avoiding the generation of complex numbers

            if term_2 < 0
                term_2 = abs(term_2);
                term_2 = -(term_2)^0.5;
            else
                term_2 = term_2^0.5;
            end

            x_nod_new(1,ii) = R1a*term_2;
            x_nod_new(2,ii) = y_ii + (R1a*2) * x_aux_2/s1a;
            x_nod_new(3,ii) = z_ii;

        else

            x_nod_new(1,ii) = R1a*sin(pi*x_aux_2/s1a)^0.5;
            x_nod_new(2,ii) = y_ii + (R1a*2) * x_aux_2/s1a;
            x_nod_new(3,ii) = z_ii;
        end


    elseif ( x_ii > s1 && x_ii <= (s1+s2) )

        x_aux = x_ii-s1;

        R2a = R2 - y_ii;
        s2a = pi*R2a;

        x_aux_2 = x_aux * s2a/s2;

        param = 1/15*0.15; %mesh displacements parameters
        exp_n = 0.01;

        if x_aux_2 ~= 0

            term_1 = cos(pi*x_aux_2/s2a); %avoiding the generation of complex numbers

            if term_1 < 0
```

```
                term_1 = abs(term_1);
                term_1 = -(term_1)^exp_n;
            else
                term_1 = term_1^exp_n;
            end
            x_aux_2 = -param*term_1 + x_aux_2;

            term_2 = sin(pi*x_aux_2/s2a); %avoiding the generation of complex numbers

            if term_2 < 0
                term_2 = abs(term_2);
                term_2 = -(term_2)^0.5;
            else
                term_2 = term_2^0.5;
            end

        x_nod_new(1,ii) = -R2a*term_2;
        x_nod_new(2,ii) = -y_ii + R1*2 - (R2a*2) * x_aux_2/s2a;
        x_nod_new(3,ii) = z_ii;

        else

        x_nod_new(1,ii) = -R2a*sin(pi*x_aux_2/s2a)^0.5;
        x_nod_new(2,ii) = -y_ii + R1*2 - (R2a*2) * x_aux_2/s2a;
        x_nod_new(3,ii) = z_ii;

        end

    elseif ( x_ii > (s1+s2)  )

        x_aux = x_ii-(s1+s2);

        R3a = R3 - y_ii;
        s3a = pi*R3a;

        x_aux_2 = x_aux * s3a/s3;

        param = 7/9*0.15; %mesh displacements parameters
        exp_n = 1;

        if x_aux_2 ~= 0

            term_1 = cos(pi*x_aux_2/s3a); %avoiding the generation of complex numbers

            if term_1 < 0
                term_1 = abs(term_1);
                term_1 = -(term_1)^exp_n;
            else
                term_1 = term_1^exp_n;
            end
            x_aux_2 = -param*term_1 + x_aux_2;

            term_2 = sin( pi* x_aux_2/s3a); %avoiding the generation of complex numbers

            if term_2 < 0
                term_2 = abs(term_2);
                term_2 = -(term_2)^0.5;
            else
                term_2 = term_2^0.5;
            end

            x_nod_new(1,ii) = R3a*term_2;
            x_nod_new(2,ii) = y_ii + ( R1*2 - R2*2 ) + (R3a*2) * x_aux_2/s3a;
            x_nod_new(3,ii) = z_ii;

        else

            x_nod_new(1,ii) = R3a*sin( pi* x_aux_2/s3a)^0.5;
            x_nod_new(2,ii) = y_ii + ( R1*2 - R2*2 ) + (R3a*2) * x_aux_2/s3a;
            x_nod_new(3,ii) = z_ii;

        end

    end

end

x_nod = x_nod_new;

% save the final_mesh_file
save('final_mesh_file.mat', 'num_x', 'x_nod', 'x_val', 'num_e', 'e_nod', 'e_are', 'e_val')
```

D. Additional Material's Attribution routine

```
% this routine matches a certain group of nodes to its material and patch

clear all
close all

% load:
load('final_mesh_file.mat')

% load structure file
load('mater_struct_file.mat')
n_pat = 2;
n_mat = 2;
mater_struct_array(1,1) = n_pat; % this indicates how many patches there are..
mater_struct_array(1,4) = n_mat; % this indicates how many materials there are..
mater_struct_array(1,11) = 8; % this indicates that it is a 3D study
mater_material_array = zeros(n_mat,20,3); % this erases all the material properties

%initial point of material changing
x0 = 17;
y0 = 0.03;
z0 = 6.5;
zf = 7.5;

% final point of material changing
x1 = 0.05; % beginning of material 2/3
x2 = 0.90; % length of material 2/3
h = 0.03; % thickness of material 2/3

% Loop over all nodes
for ii = 1:num_x

    x_ii = x_nod(1,ii);
    y_ii = x_nod(2,ii);
    z_ii = x_nod(3,ii);

    if ( ( x_ii > x0 - 1e-6 ) && ( y_ii < y0 + 1e-6 ) && ( z_ii > z0 - 1e-6 ) && ( z_ii < zf ) )
           x_val(1,ii) = 3; % it becomes patch 2/3
           x_val(4,ii) = 3; % it material patch 2/3
    end

end

% Loop over all elements
for ii = 1:num_e
    for jj = 1:4
        id_nod = e_nod(jj,ii);
        e_val(1,ii) = x_val(1,id_nod); % patch of node id_nod
        e_val(4,ii) = x_val(4,id_nod); % material of node id_nod
    end
end

save('mater_struct_file.mat', 'mater_struct_array');
save('mater_material_file.mat', 'mater_material_array');
save('final_mesh_file.mat', 'e_are', 'e_nod', 'e_val', 'num_e', 'num_x', 'x_nod', 'x_val');
```